POLITECNICO DI TORINO

Master's Degree in Aerospace Engineering

Politecnico di Torino

von KARMAN INSTITUTE FOR FLUID DYNAMICS

Master's Degree Thesis

Experimental investigation of sloshing on the Advanced Lead Fast Reactor European Demonstrator

von Karman Institute tutors:
Prof. Delphine LABOUREUR
Dr. Jannette FRANDSEN
Politecnico di Torino tutors:
Prof. Salvatore BRISCHETTO
Prof. Marco GHERLONE
External tutor:
Dr. Jean MULLER

Candidate
Vito GRASSO, 304792

Academic Year 2023/2024

Abstract

Earthquake's induced sloshing may lead to dangerous effects in a nuclear reactor pool during seismic events. The objective of this thesis is to investigate sloshing processes in the Advanced Lead Fast Reactor European Demonstrator (ALFRED).
Model scale experiments (1:18.4) have been carried out. The model of ALFRED is a reproduction in plexiglass of the very hot plenum of the actual demonstrator, based on Froude number scaling. Distilled water is used in similarity with the lead in the demonstrator. The model consists of an annular tank, as nuclear pool and internal primary core are simply reproduced. In the peripheral, nine cylinders are distributed and represent the internal structures of the demonstrator. The dominating sloshing processes take place above the diaphragm.
Harmonic base excitation in one Degree of Freedom (DoF) forms the basis of the present investigations. Nonlinear free-surface physics have been identified for different water depths, forcing amplitudes and frequencies outside and at/near to the fundamental resonance of the system. The wave-structure interactions add complexity to the sloshing processes, altering the skewness of the free-surface orbits.
Further, idealized norm-based earthquakes test series have been undertaken. These tests contain base excitation signals outside and close to the fundamental system frequency. The analysis of the seismic base excitation test series performed in 1-3 DoFs exhibits highly nonlinear and random behaviour. The short duration input signals add further to the randomness of the sloshing processes. Violent sloshing motions were detected for several events, especially related to the increasing amplitudes/intensity of earthquakes' excitation signals close to the fundamental frequency.
Additionally, a hazard condition in the primary nuclear reactor has been simulated by removing three of the internal cylinders (steam generators). In these parametric studies and via comparisons, a highly damped system was identified.
A preliminary full-scale assessment has been done both for the harmonic base excitation test series and for the norm-based earthquakes test series. The maximum ground accelerations and associated maximum amplitudes have been computed to perform a scale effect assessment based on the Froude scaling.

Keywords: **sloshing**, **experimental investigation**, **nuclear reactor**, **earthquakes**, **nonlinear physics**

Contents

List of Figures

List of Tables

Nomenclature

Roman Symbols

x	Cartesian coordinate	[m]
y	Cartesian coordinate	[m]
z	Vertical Cartesian coordinate	[m]
u	Horizontal velocity along x	[m s^{-1}]
v	Horizontal velocity along y	[m s^{-1}]
w	Vertical velocity along z	[m s^{-1}]
R	Radius	[m]
D	Diameter	[m]
h	Liquid level	[m]
t	Time	[s]
f	Frequency	[s^{-1}]
f_n	Natural Frequency	[s^{-1}]
a	External Forcing Amplitude	[m]
g	Gravity	[m s^{-2}]
m	Mass	[kg]
q	Fluid velocity vector (u,v,w)	[m s^{-1}]
V	Potential energy	[J]
T	Kinetical energy	[J]
L	Lagrangian function	[J]

Greek Symbols

Φ	Potential function of velocity	[m^2 s^{-1}]

η	Free surface vertical coordinate	[m]
ω	Angular frequency	[rad s^{-1}]
ω_n	Natural Angular frequency	[rad s^{-1}]
λ	Wavelength	[m]
θ	Azimuthal coordinate	[m]
ξ	Root of J'(ξ)=0	[-]
ρ	Density of the fluid	[kg m^{-3}]
ν	Kinematic viscosity	[m^2 s^{-1}]
μ	Dynamic viscosity	[Pa s^{-1}]
ζ	Wave amplitude	[-]
κ	Dimensionless external forcing acceleration	[-]
τ	Time	[s]

Subscript

m	number of diametral nodes
n	number of diametral nodes - 1
n	natural as subscript of ω
x	in x direction
y	in y direction
z	in z direction

Dimensionless numbers

Re	Reynolds	$\frac{\rho \mathrm{VD}}{\mu}$
Fr	Froude	$\frac{\mathrm{U}^2}{\mathrm{gD}}$

Acronyms

VKI	von Karman Institure for Fluid Dynamics
PASCAL	Proof of Augmented Safety Conditions in Advanced Liquid-Metal-Cooled Systems

ALFRED Advanced Lead Fast Reactor European Demonstrator

MYRRHA Multi-purpose hYbrid research Reactor for High-tech Applications

ASME American Society of Mechanical Engineers

SHAKESPEARE SHaking Apparatus for Kinetic experiments of Sloshing Projects with EArthquake REproduction

SG Steam Generator

DHR Decay Heat Removal

MCM Monte Carlo method

DoF Degree of Freedom

Chapter 1

Background on sloshing

1.1 Definition of sloshing

> "**Sloshing** means any motion of the free surface inside a container."[1]

In a more simple way, sloshing can be pictured in everyday life because it occurs each time one walks with a glass partially or completely filled with water: the liquid can spill out of the container if its free surface is excited enough. Depending on a series on parameters, such as the type of disturbance, the container shape, the frequency of external excitation or the presence of dumping element in the container itself, the free surface can move differently by kind of motion: simple planar or non-planar waves, rotational waves, symmetric or asymmetric modes, periodic or chaotic motion. Things starts to get more complicated when the free liquid surface interacts with elastic container's walls or internal frames, showing up a wave-structure interaction in the form of interacting modal modes.
The sloshing processes introduce larger loads on the walls due to the free-liquid surface motion. Containers' integrity due to sloshing phenomena needs to be properly investigated and the typical sloshing parameters need to be known. In this scenario, hydrodynamic pressure distribution, natural frequencies of the free liquid surface and mechanical estimation of stress distribution on structures need to be estimated. The hydrodynamic pressure has two components: the first proportional to the acceleration of the tank; the second one due to the free-surface-liquid motion. Such as any other dynamic problem, mass-spring-damper systems or pendulum are used to extract this information. As written in Ibrahim's work [1], despite an infinite number of natural frequencies of the system, only the first ones are really interested in the majority of the engineer applications.
Sloshing is a problem particularly sensitive to the initial conditions and boundary conditions, the surface tension, the height of free-liquid surface in the containers (partially or completely filled). The high sensibility leads to hard predictable non-linear effects, and the very problem is that each type of moving containers has its own non-linearity associated.

1.2 History of sloshing

In order to write a quick but essential overview on the impact of sloshing studies in research history, [1] was used as starting point, because it's one of the most compre-

hensive work that collects biggest achievements in the literature so far (from 1960 to 2005). From the author Ibrahim it's well known also the review article in [2], whose purpose is to review the research work developed in different engineering applications.
The issue of liquid sloshing in both moving and stationary containers continues to be a significant focus for aerospace, civil, and nuclear engineers, as well as physicists, road tanker and ship tanker designers, and mathematicians. Civil engineers and seismologists have investigated the effects of liquid sloshing on large dams, oil tanks, and elevated water towers during ground motion. They have also utilized liquid tanks on the rooftops of buildings to mitigate building oscillations caused by earthquakes.
Sloshing is a matter of fundamental interest when earthquakes and tsunamis effect on containers is studied. The Great Alaskan earthquake in 1964 can be considered a turning point in recent engineer history: [3] highlights how that tragedy can be considered as one of the strongest stimuli that led to major breakthroughs in earth science research. Sloshing become a matter of interest when associated to seismic events since then, as cited in [4] about the water storage tank response to earthquake loads. Events that involved the Fukushima I Nuclear Power Plant during the magnitude 9.0 Tohoku earthquake and tsunami in March 2011 represent a pivotal point in the current matter.
Since the early 1960s, considerable concern about the dynamics of free-liquid surface motion was expressed also in terms of the impact of liquid propellant sloshing on the flight performance of jet vehicles, leading to the emergence of new areas of research. Abramson (2003) is one of the most influential author in that particular research sector, and reviewed its own work in [5]. It's usual to refers to [6], whose conclusion lead to the necessity of providing baffles and dumping devices to allow the maintenance of adequate flow rates. In [7] Abramson (1960) compares experimental results of test on smaller models of missile tanks with full-scale ones by the means of a similitude theory, while in [8] Abramson (1961) provides a mechanical model for representation of linear fuel sloshing with damping in cylindrical tanks. It's important to notice that even Apollo 11 experienced sloshing during the lunar landing phases. In particular, in the mission transcripts the sloshing was considered the phenomenon responsible for the spacecraft uncontrolled descend, the Landing Point Designator uselessness and the premature latch of the propellant low-sensor [9]. As reported in the beginning of [10], the Space Exploration Technologies (SpaceX) launched X Demo Flight 2 by means of Falcon 1 (March 20, 2007) occurs in failure. Propellant slosh is considered the primary contributor to an instability in pitch, yaw and in particular in roll which led to a fatal roll torque. The final consequence was overeating of the engine and flame-out of it because that roll torque was too difficult to stabilized even for the roll control thrusters.
Faltinsen can be considered one of the most author in sloshing as well as Ibrahim. [11] (2009) presents a complete overview on the sloshing problem, but with a special eye on marine and land-based applications. This is the name one must know when

are treated topics such as ocean waves and sloshing related with ship motion. Faltinsen interest in coupling of sloshing and ship motion is presented also in [12] and [13]. It's fundamental to make mention of [14], one of the main reference for nonlinear sloshing theory in rectangular tanks.
The last field of interest of sloshing that is reported in the current literature review is about public transportation of liquid tank, such as oil tank, by means of vehicle or railways (in example are referenced [2] and [11]). Here is also cited [15] and [16], which define the most critical conditions for tanks safety by the means of simulation about typical accidents, such as derailment or vehicles accidents.

1.3 Sloshing theory

1.3.1 Hints of linear sloshing theory

An overview on the theory of sloshing is presented, proposing as main reference [1] as it can be applicable both to free or forcing liquid free-surface motion. The fluid field equation is obtained for the general case of a tank moving in space along any trajectory. The container's walls are considered rigid and impermeable, while the flow is assumed inviscid, incompressible and initially irrotational. If the field is gravitational, then the hypothesis on the flow could also be considering negligible the capillary or the surface tension.
The reference systems implied are exposed in Figure 1.1: $Oxyz$ is the moving Cartesian coordinate frame that's attached to the container, while $OX'Y'Z'$ is the stationary Cartesian coordinate frame.

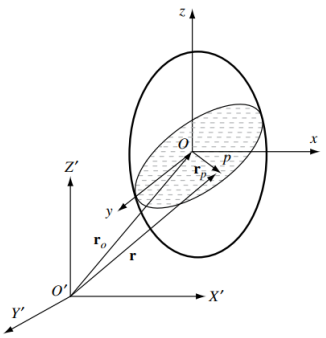

Figure 1.1: Moving liquid container showing inertia and moving coordinates [1]

Euler equation of motion is written as follows:

$$\frac{\partial}{\partial t}\mathbf{q} + (q \cdot \nabla)\mathbf{q} = -\frac{1}{\rho}\nabla P - \nabla(gZ') \tag{1.1}$$

where $\mathbf{q}$ is the fluid velocity, $\partial\mathbf{q}/\partial t$ is the local acceleration of the flow measured by a fixed observer, $(\mathbf{q} \cdot \nabla)\mathbf{q}$ is the convective term of acceleration, P is the fluid

pressure, ρ is the fluid density, gZ' is the gravitational potential. For irrotational flow $\nabla \times \mathbf{q} = 0$ and exists the velocity potential function:

$$\mathbf{q} = -\nabla\Phi \tag{1.2}$$

The potential flow function leads to the Laplace's equation:

$$\nabla^2\Phi = 0 \tag{1.3}$$

Besides, the hypothesis of potential flow leads to the following form of the pressure equation:

$$\nabla\left(\frac{P}{\rho} + \frac{1}{2}q^2 + gZ' - \frac{\partial\Phi}{\partial t}\right) = 0 \tag{1.4}$$

in the $OX'Y'Z'$ stationary Cartesian reference frame. Let consider $\mathbf{V}_0$ the velocity of O of $Oxyz$ frame relative to O' of the $OX'Y'Z'$ frame. The moving frame is such that the undisturbed free surface coincides with the Oxy plane. Eq. 1.4 is equal to

$$\nabla\left(\frac{P}{\rho} + \frac{1}{2}q^2 + gZ' - \frac{\partial\Phi}{\partial t} + \mathbf{V}_0 \cdot \nabla\Phi\right) = 0 \tag{1.5}$$

written in terms of the total fluid velocity related to the fixed coordinates.
The kinematic free-surface condition is imposed, so the vertical velocity of a fluid particle on the free surface is equal to the vertical velocity of the same free surface:

$$-\frac{\partial\Phi}{\partial z} = \frac{\partial\eta}{\partial t} + \mathbf{q}_{rel} \cdot \eta \tag{1.6}$$

where $z = \eta(r, \theta, t) = \eta(x, y, t)$ is the vertical velocity of the fluid particle. The boundary conditions at the wall and the bottom are applied in the Cartesian and cylindrical coordinates:

$$-\left.\frac{\partial\Phi}{\partial z}\right|_{z=-h} = \ddot{Z}_0, -\left.\frac{\partial\Phi}{\partial x}\right|_{x=a} = \ddot{X}_0 \tag{1.7}$$

$$-\left.\frac{\partial\Phi}{\partial z}\right|_{z=-h} = \ddot{Z}_0, -\left.\frac{\partial\Phi}{\partial r}\right|_{r=R} = \ddot{X}_0 cos\theta \tag{1.8}$$

When the hypothesis of the potential flow is respected, then the previous set of equations is the starting point for describing the sloshing problem. The nonlinearity in the boundary value problem only exists in the free-surface boundary conditions for $z = \eta$.
Since the sloshing problem requires the extraction of the natural frequencies, a modal analysis is required: this kind of proposed approach works if the potential function is obtained analytically in a closed form. The variational formulation associated with the Rayleigh-Ritz method (as a method for approximating eigenvalues) is another valid approach to the modal problem. It starts with the Hamilton's principle statement:

$$\delta I = \delta \int_{t_1}^{t_2} (T - V)dt = 0 \tag{1.9}$$

where T and V are the kinetic and potential energy of the system. The parenthesis $(T - V)$ stands for the Lagrangian function $L = T - V$ that must be minimized by means of the Hamilton's principle. This formulation is very powerful if compared to the proposed previous one because it brings in one statement the fluid equations and the associated boundary conditions. This advantage is typical of the variational formulation's approaches.
The variational formulation leads to the following frequency equation:

$$|A_{mn} - \lambda B_{mn}| = 0 \tag{1.10}$$

where $\lambda = \omega^2/g$ and contains the frequency information, while A_{mn} and B_{mn} are symmetrical matrices and are obtained starting from the Hamilton's statement in Eq. 1.9 and the application of a Rayleigh-Ritz method [1].

1.3.2 Normal modes in an Annular tank

Hints on the annular tank natural frequencies are presented because the this geometry fits with the simpler structure of primary pool of a nuclear reactor. Indeed, the inner circular cylinder of the container should represents a simplification of the primary core of the pool. An explanatory sketch is in Figure 1.2.

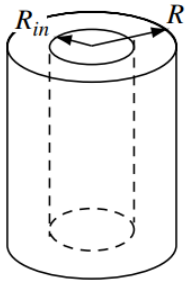

Figure 1.2: Annular tank geometry [1]: R is the external radius, while R_{in} represents the radius of the internal cylinder

The dominant mode is the first $m = 1$, and it performs several fluid forces if compared to the others. If the surface tension is negligible, the natural frequencies are:

$$\omega_{mn}^2 = \frac{g}{R}\xi_{mn}\tanh(\frac{\xi_{mn}h}{R}) \tag{1.11}$$

and it's obtained by solving the determinant $\Delta_m(\xi_{mn}) = 0$ [17]. If $k = R_{in}/R$ is the ratio of inner radius to outer radius, the values of the parameter ξ_{mn} for an annular tank and when $m = 0, 1, 2$, $n = 0, 1, 2$ are reported in Table 1.1 and represented in Figure 1.3.

	k, ratio of inner radius R_{in} to outer radius R									
(m,n)	0.0	0.1	0.2	0.3	0.4	0.5	0.6	0.7	0.8	0.9
(0,1)	3.832	3.941	4.236	4.706	5.391	6.393	7.930	10.522	15.738	31.429
(0,2)	7.016	7.331	8.055	9.104	10.558	12.625	15.747	20.969	31.431	62.839
(1,0)	1.841	1.804	1.705	1.582	1.462	1.355	1.262	1.182	1.113	1.053
(1,1)	5.331	5.137	4.961	5.137	5.659	6.565	8.041	10.592	15.778	31.447
(1,2)	8.536	8.199	8.433	9.308	10.683	12.706	15.801	21.004	31.451	62.847
(2,0)	3.054	3.053	3.035	2.968	2.842	2.681	2.516	2.363	2.227	2.106
(2,1)	6.706	6.687	6.495	6.274	6.416	7.063	8.367	10.799	15.898	31.500
(2,2)	9.970	9.888	9.550	9.918	11.056	12.949	15.962	21.106	31.511	62.918

Table 1.1: Values of parameter ξ_{mn} for an annular cylindrical tank when $m = 0, 1, 2$ and $n = 0, 1, 2$ [18]

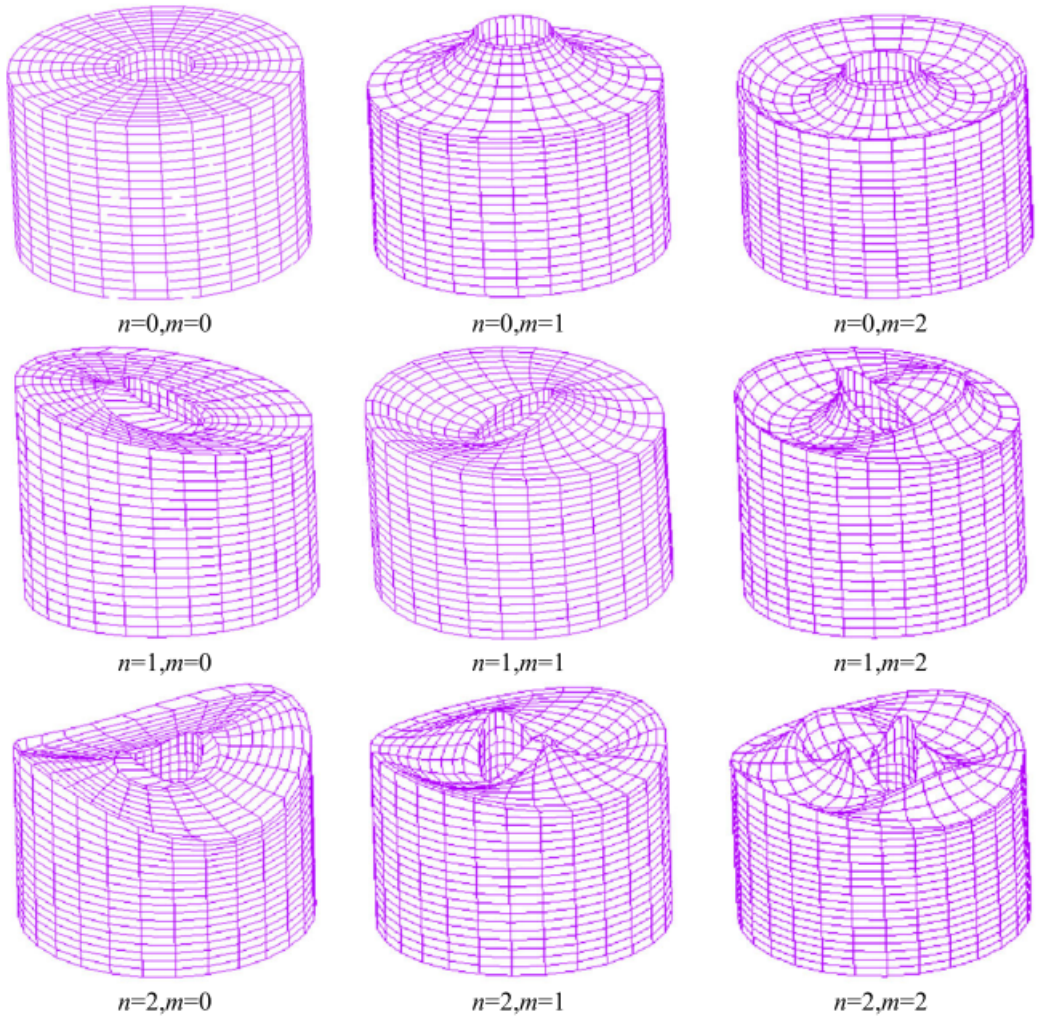

Figure 1.3: Modes of free-surface sloshing in annular cylindrical tank [19]

1.3.3 Hints of weakly non-linear wave regimes

The linear theory does not take in account the important vertical motion of the free-liquid surface. The weakly non-linear regimes are experienced when the forcing frequency is at/near the resonance one of the dynamic system. The linear theory fails to predict the complexity of the sloshing since the nodal diameters could change; something that usually happens is the combination of modal forms, whom frequency is different from the linear ones. Experimental results of forced sloshing are quickly treated in [9], [20] and [21].
Three main sloshing wave regimes are identified:

- steady state planar wave regime, which adjusts the linear motion prediction for a frequency away from the resonance condition;
- swirling regime, which is characterized by rotational motion waves;
- chaos regime, which is characterized by randomness, potentially wave breaking and possible formation of bubbles in the liquid itself.

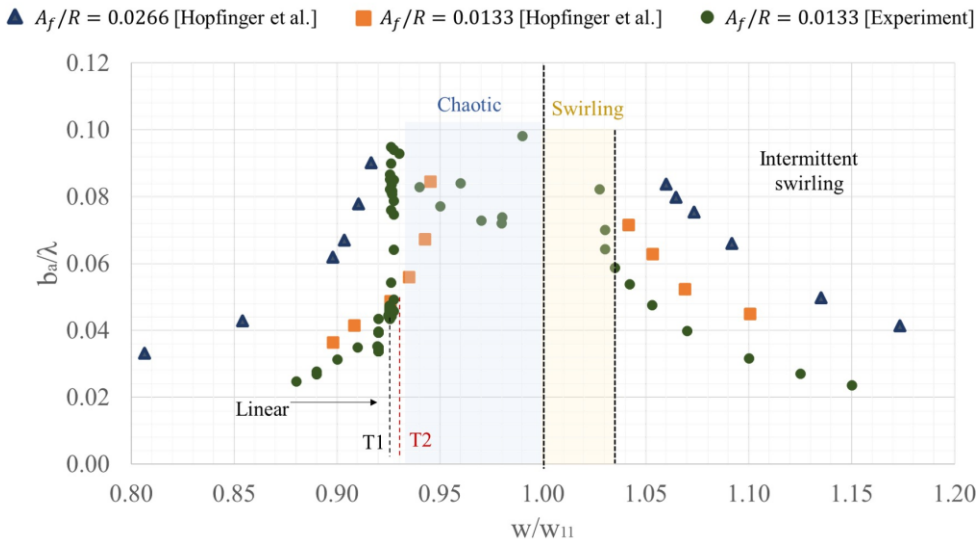

Figure 1.4: Demonstrative representation of the sloshing regimes taken from [20] and [21]: Dimensionless stabilised wave amplitude (b_a/λ) for harmonic base excitation in one direction at different forcing amplitude (A_f/R) and forcing frequency (ω/ω_{11}); performed test in [20] are the circles, the triangle and square points are extracted from [21].

1.4 Sloshing in nuclear industry

Earthquake induced sloshing may lead to dangerous effects in the nuclear power industry. Housner (1957), which is one of the most influential author on the dynamic behaviour of accelerated fluid containers [22], treats about problems of nuclear power

plants in [23] (1966). For the records, the accident of SL-1 reactor in the USA (1961) can be also mentioned in this quick literature review: [24] collocates the extreme impact of coolant liquid on the ceiling of the primary pool within the one of the problem that occurs in that tragedy. Another technical report about nuclear reactors and earthquakes is [25], cited by many as a reference to recent history of accidents.
Nowadays, the sloshing problem in the nuclear reactors is still a very current topic. Seismic safety has been brought to a primary role after the event that involved the Fukushima I Nuclear Power Plant during the magnitude 9.0 Tohoku earthquake and tsunami in March 2011. With the advent in the close future of the new class of *Generation IV Lead-cooled Fast Neutron Reactor demonstrator*, new studies have been conducted to guarantee safety. The most cited authors in this category of sloshing application are Ibrahim (2005), Faltinsen (2003) and Housner (1966). [26] can be considered a good starting point in the study of sloshing in the this new type of Lead-Cooled fast reactors. From the same author, Jeltsov (2015), also [27] can be cited as well, because it presents a parametric study of sloshing effects in the primary system of this reactors. According to the sloshing theory, in his works Jeltsov affirms that generally the mitigation strategies for earthquake is to take advantage from seismic isolation system. One of the most dangerous collateral effects is the decrease of the fundamental frequencies in the response spectra of some interesting point of the structure. That shifting brings the system closer to liquid sloshing frequencies.
Among other relevant studies, [28], published for the American Nuclear Society in 2017, is cited and treats about a CFD and experimental investigation of sloshing parameters in MYRRHA (*Multi-purpose hYbrid Research Reactor for High-tech Applications*) a lead-bismuth cooled fast reactor, managed by SCK CEN the Belgian Centre for Nuclear Research. It's part with the *Advanced Lead Fast Reactor European Demonstrator* in the *Proof of Augmented Safety Conditions in Advanced Liquid-Metal-Cooled Systems* (PASCAL) framework. More details about the project are in the next Paragraph 1.5.

1.5 PASCAL project

Advanced Lead Fast Reactor European Demonstrator (ALFRED)[29], is a project by the European Sustainable Nuclear Industrial Initiative, aimed at developing *Generation IV Lead-cooled Fast Neutron Reactor demonstrator* [30] as part of the EU's Strategic Energy Technology plan. Lead by FALCON association (Fostering ALfred CONstriction), formed by *Ansaldo Nucleare*, *Ente per le Nuove tecnologie, l'Energia e l'Ambiente (ENEA)* and the Institute for Nuclear Research *(ICN)*, this project is committed to the future of fission nuclear power as the carbon-free source that, together with renewable, will drive the transition towards sustainable, reliable and affordable electricity. This type of reactor is specific because represents a solution for fast reactors cooled with heavy liquid.

Von Karman Institute (VKI) has been conducting both experimental and numerical studies in collaboration with *Ansaldo Nucleare* to ensure nuclear safety for operations related to ALFRED.
European project *Proof of Augmented Safety Conditions in Advanced Liquid-Metal-Cooled Systems* (PASCAL) [31] is well suited for the previous objective. PASCAL project aims to the advancement of the safety research on innovative nuclear reactors ALFRED and MYRRHA, and to generate ready-for-use evidence for the discussions between the designers of those reactors and the respective safety authorities in the pre-licensing phase. It's part of the EU Framework Program for Research and Innovation *Horizon 2020*.
Earthquakes induced sloshing may lead to dangerous effects in a nuclear reactor pool during seismic events. PASCAL's framework dedicate to the sloshing part aims to identify if seismic activity is critical for the nuclear reactor safety and to give quantitatively a prediction of the damages on the involved structures. One can think about it as a progression of the previous works that started in the 1960s (Paragraph 1.4).

1.6 Thesis project's objective

The objective of this thesis is to investigate sloshing processes in the ALFRED's model. Model scale experiments (1:18.4) have been performed by means of the von Karman Institute's scaled reproduction in plexiglass of the very hot plenum of the actual demonstrator. The present chapter has been used to introduce an historical background on the sloshing induced accidents and features, some brief hints of linear and weakly linear theory. PASCAL project has been also mentioned because some of the seismic simulation test series have been post-processed in the current thesis.
Chapter 2 collects the fundamental characteristic of the experimental setup and the methodology of investigation. Similarities studies, based on equivalence related to Froude number, had already been done in the past years and are quickly reported in this chapter to explain the similitude within distilled water in the reduced model and the molten lead in the demonstrator. The geometry model is then presented to give a glimpse of its own complexity, which affects consistently the dominating sloshing processes taking place. Tests have been set up through usage of the VKI's three degree of freedom shake table with hydraulic piston type actuators. Capacitance probes have been used as an intrusive method of investigation to measure the amplitude of distilled water waves of the free surface when an excitation is applied. Their calibration is performed using the Monte Carlo method, according to the ASME PTC 19.1 (2018). A complete test matrix of the performed tests is presented.
Chapter 3 presents the result of some of the most significant test series which has been performed. Harmonic base excitation in one Degree of Freedom (DoF) has been identified as the starting point of the sloshing processes' investigation. Different water depths, forcing amplitudes and frequencies outside and at/near to the fundamental resonance of the system have been selected to highlight the behaviour of

the liquid free-surface when they change. Nonlinear free-surface physics are expected to be identified, combined with a non-negligible wave-structure interaction that adds complexity to the sloshing processes.
Chapter 4 presents the results of some test series performed in the sloshing framework of PASCAL, where some idealized norm-base earthquakes input signals have been undertaken. These tests contain base excitation signals outside and close to the fundamental system frequency. The short duration input signals add further to the randomness of the sloshing processes. A hazard condition in the primary nuclear reactor has been simulated by removing three of the internal cylinders (steam generators).
As stated in the abstract and the introduction, the framework of the current Master thesis is the experimental investigation of the highly nonlinear sloshing processes that occur in the scaled reproduction of the ALFRED's model. At the end of each of the performed test series, some observations can be done on the nuclear safety due to sloshing induced accidents. Harmonic based excitations have been extremely useful to decouple the complexity of current study case. As a consequence, seismic simulations can be critically analysed.

Chapter 2

Experimental setup and methods

This chapter presents an overview on the experimental setup and the methodology for performing the test series and acquiring the data.
The shaking table in VKI laboratories was used for performing the test cases of interest, It has 3 degree of freedom with hydraulic piston type actuators and a well lubricated mechanism that performs independent motion in sway, surge and heave. ALFRED model had been designed by VKI team in the past years and was properly mounted on the shaking table for the PASCAL project purposes (Chapter 1.5). The model consists of a 1:18.4 scaled reproduction in plexiglass of the very hot plenum of ALFRED reactor demonstrator, based on equivalence related to Froude's number because waves amplitude depend on the acceleration of external excitation and gravitational acceleration. The model represents properly the internal structure of the nuclear reactor demonstrator in according to the similarities studies, which are based on the assumptions described in Chapter 2.2.1.
A combination of two different types of accelerometer has been mounted on the table. The primary acceleration measurements system is a proper configuration of six digital accelerometers developed in VKI, and based on the MMA8451Q digital sensor. The secondary acceleration measurements system is a ceramic shear high sensitivity sensor, a PCB Piezotronics 356B18.
The 1D elevation of the free surface of water has been captured by two capacitance probes provided by Artelia. These sensors measure the capacitance of a copper wire in function of its immersed height in the water. Three capacitance probes were supposed to work, but one of them revealed faulting for reasons still unknown by the time of the first experimental campaign. Calibration of them has been performed twice, one at the beginning and one at the ending of the test, as good practice suggests. According to ASME Performance Test Code 19.1 (2018) [32], a Monte Carlo method has been used to extract uncertainty from probes measurements. In particular, for the capacitance probes this method has been repeated on 50,000 random points from the probability density function calculated on the calibration test. At the end of the first campaign, the calibration results were each other consistent for the two working probes, while it shows some issues on the uncertainty values for the faulting sensor.
An Arduino at 200 Hz interface is used to drive the six accelerometers and acquire the measurements, while the PCB accelerometers and the capacitance probes are connected to a NI DAQ 9215 at 2048 Hz with their own cards to acquire the data. The whole system is connected to a PC by USB ports, so the collective data are summed up in one `.tdms` file compiled properly by the LabView program. In post-processing

phase, the acceleration from PCB and the amplitude of free surface was resampled at 200 Hz, according to the acceleration taken from the Arduino.
In addition to the essential experimental setup, for the first test campaign a high-speed camera *Dantec - SpeedSense M310* camera was positioned at a proper distance from the shaking table for catching the free surface motion of this special case study. The acquisition resolution was set to 768 pixels*576 pixels and the frame rate was of 50 frame per second. The camera was not fitted for capturing quantitative amplitude of the free surface motion, but only for identifying the sloshing resonance modes and capturing non-linear phenomenon. Behind the ALFRED model is collocated a large sheet of translucent paper, which filtrates the light of a square white LED device for providing a uniform illumination.
In the following paragraphs, a deeper look on the setup is furnished. ALFRED model is described for giving the reader a glimpse of the complexity and distinctiveness of it. Besides, it aims to give the reader an explanation on why this structural configuration should be congenial to the sloshing problem. Shaking table is described in order to learn how to treat the acquired data from the test in terms of instrumentation limits, so the uncertainty budgets on the results. Capacitance probes are analysed in details and a deeper look in Monte Carlo code is provided for a correct interpretation of the calibration laws output. Finally, a final and complete overview of the shaking table facility is provided, highlighting issues and practical procedures that have been followed to perform the test campaign.

2.1 Shaking table - SHAKESPEARE facility

Here, a small overview about the shaking table facility is provided. SHAKESPEARE stands for SHaking Apparatus for Kinetic Experiments of Sloshing Projects with EArthquake REproduction. This facility has been designed for testing the MYRRHA reactor's mockup, which is the ALFRED "brother" and it's managed by the *Belgian Centre for Nuclear Research*, *SCK CEN*.
SHAKESPEARE is a three axis shaking table used for simulating the seismic events on a prototype of the ALFRED reactor. It allows a maximum acceleration of 1.1 g for a maximum mass of 500 kg load, according to [33]. SHAKESPEARE shaking table is dimensioned considering that the larger model scale cannot be bigger 1/10 of the prototype. This is a crucial point because the geometric similarity must be respected. The dimensions of the table are the product of a tradeoff: closer the model dimension are to the prototype and more all the non-dimensional number are easily respected; by the other hand, large model are expensive.
In order to provide the forces for reaching the required accelerations in the three directions of the geometrical space, this shaking table is installed with one hydraulic cylinder piston type actuator, as it's shown in Figure 2.1. This system assures high frequency response, for reaching a more realistic seismic simulation from up to 10-15 Hz. The energy that the actuator needs is provided by a hydraulic system collocated

outside the laboratory, while it's controlled by a control unit shown in Figure 2.2.

(a) Shaking table placement

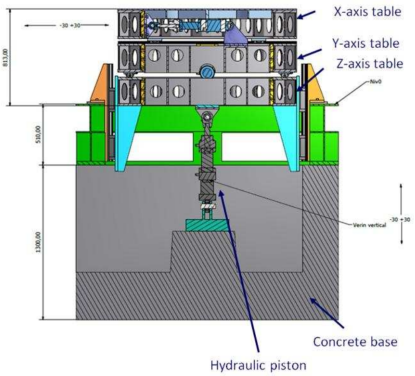

(b)

Figure 2.1: SHAKESPEARE shaking table ([33]): (a) shaking table placement; (b) shaking table concept

(a)

(b)

Figure 2.2: SHAKESPEARE shaking table ([33]): (a) shaking table control unit; (b) external hydraulic pumps that provide the hydraulic power for the shaking table facility

A concrete base attaches the whole shaking table to the floor, added by a floating base that supports the shaking table during the excitations. Each one of them are divided by an anti-vibration zone, specifically design for protecting the building by vibrations of the table. The supporting frame is installed upon the floating base, and it's composed by three share-shaped frames: the first one, on the top of it, provides movement along X-axis; the second one provides movement along Y-axis; the third one provides movement along Z-axis, supports the total weight of the table and its guides are fixed on the supporting frame. The movement of each frame is independent because of the guides amid them. The modular design can ensure that

the motion on each degree of freedom is independent and enough well controlled. The lack of a feedback loop on the module's position doesn't give so much confidence as on the frequency actuation. For more information about table uncertainties on displacements and frequencies, Simonini provides an example of demonstration of that in [9].

2.2 ALFRED model

ALFRED demonstrator reactor sketch is shown in Figure 2.3, taken from the technical report in [29]. The model consists of a 1:18.4 scaled reproduction in plexiglass of the very hot plenum of the demonstrator, based on equivalence related to Froude's number because waves amplitude depend on the acceleration of external excitation and the gravitational one. The model is in plexiglass, and it's contained in a plexiglass cubic container for protecting the model from the outside agents, minimizing optical distortion when an external camera is used, besides an easy way to install it on the shaking table.
Entering the real demonstrator, the central core is in the very centre of the internal structure, and it's surrounded by an annulus filled with molten lead (chemical element *Pb*). According to the similarities studied previously and conducted by VKI, the model is filled with distilled water.

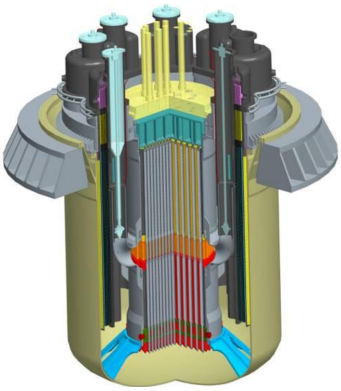

Figure 2.3: *Advanced Lead Fast Reactor European Demonstrator* [30]

2.2.1 Similarity

The study case's container can be seen as an excited annular tank partially filled with liquid at a certain height, h. The fluid is considered incompressible, $\nabla\rho = 0$ and no heat transfer is considered during the sloshing processes. Bond number is considered negligible, so in the current case study the surface tension doesn't affect the sloshing processes.
The similarity within the actual demonstrator and the model is to ALFRED scaled is presented in the technical report [34]. Starting from the momentum conservation equation, the Navier-Stokes equation for momentum is made dimensionless and the manipulated in order to make appear the following characteristic numbers:

- *Froude number* $Fr = \frac{U^2}{gL}$, which represents the relation within inertial load and gravitational forces.
- *Strouhal number* $St = \frac{L}{U\tau}$, which represents the relation within characteristic time of the phenomenon and the one of the liquid on exam;
- *Reynolds number* $Re = \frac{UL}{\nu} = \frac{UL\rho}{\mu}$, which represents the relation within inertial load and viscous force.

Appendix A presents some critical considerations made during this fundamental dimensionless analysis.
The sloshing processes in the ALFRED's model involve gravitational dependent waves, so the fundamental similarity with the actual demonstrator is in relation to the Froude number. Other condition that has been imposed in [34] are about the Strouhal number and the ratio between water depth and external radius h/R. From the technical report, it's known the result:

$$\begin{cases} (Fr)_{ALFRED} = (Fr)_{Model} \\ (St)_{ALFRED} = (St)_{Model} \\ (h/R)_{ALFRED} = (h/R)_{Model} \end{cases} \rightarrow \begin{cases} A_{Model} = 0.054 \times A_{ALFRED} \\ f_{Model} = 4.29 \times f_{ALFRED} \\ h_{Model} = 8.84\,\text{cm} \end{cases} \tag{2.1}$$

where A and f are the amplitude and frequency of the external excitation to the pool, and h_{model} is the computed water depth for a well fitted geometrical analogy.
Figure 2.4 presents the model geometry in the CAD file with design dimensions for the plexyglass model's elements. Table 2.1 sums up the effective dimension before and after the application of the similarity studies within the demonstrator and the model.

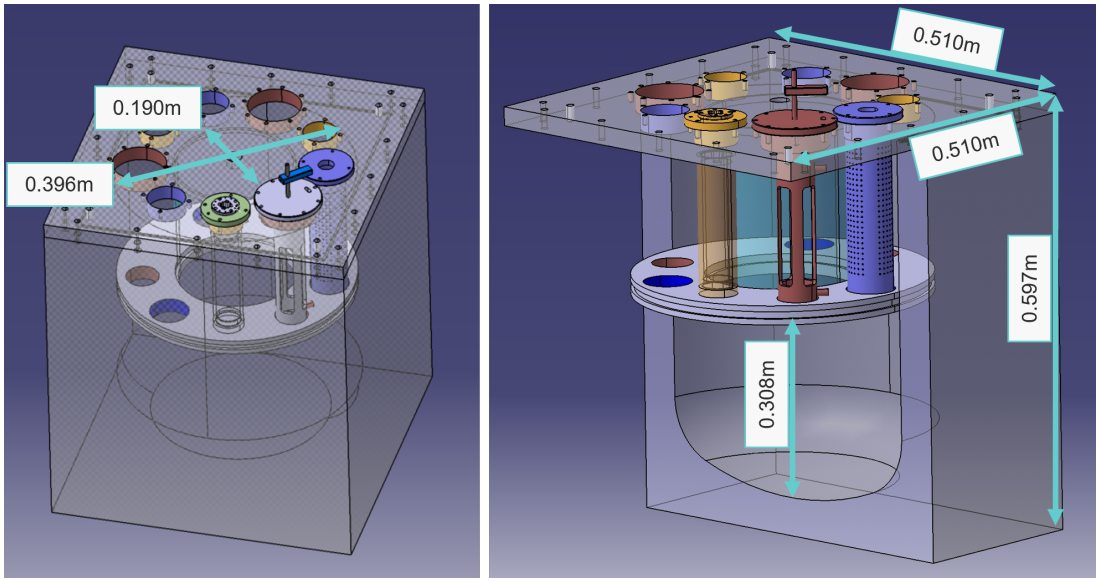

Figure 2.4: CAD drawing of ALFRED's model [34]: it's clear in the drawing that the membrane has six holes in the annulus surface, for suiting the SGs and the Pumps of the three triplets

	ALFRED	ALFRED's model	Model scaling
Internal Diameter d [m]	3.500	0.1900	1:18.4
External Diameter D [m]	7.3000	0.3960	1:18.4
Water depth h [m]	1.6300	0.0884	1:18.4
h/R ratio	0.4465	0.4465	1:1

Table 2.1: Geometric parameters that affect the similarity studies; h/R ratio is correctly equal to 1, where h refers to the water depth up to the diaphragm

2.2.2 Internal structure

The model has been designed taking in account the following design expedients:

- the pool below the hot plenum is full of the same liquid used for the top one, and it's not considered for the specific sloshing problem; so, the free surface is located in the hot plenum, while the bottom part of the reactor is full of liquid;
- upper pool and bottom pool are separated by a non-elastic diaphragm orthogonal to the longitudinal axe of the tank, creating a key-element discontinuity;
- the Steam Generator (SG) and the pumps are connected to the bottom part with a certain porosity, which could be changed depending on the initial condition of performed test; instead, the Decay Heat Removal (DHR), which in the actual demonstrator is dedicated to the cooling of the remaining heat due to decay after the showdown of the reactor, is represented as a plain tube not connected to the diaphragm.

The discontinuity membrane is the key-element because from it the water depth of reference starts. Since the geometry similarity is specifically built to preserve the hot plenum to radius ratio (h/R) equal to 1, it's easy to understand its importance.
The external annulus it's provided with 9 cylindrical seats, which are suitable for the entering of 9 cylindrical piston structures. The 9 plain tubes are organized in 3 triplets of elements distributed evenly at 40 degrees intervals.
The DHR are represented as close transparent plexiglass tubes fixed on the top of the model (Figure 2.4). With a diameter of 49.5 mm and height of 223 mm, they cannot go through the diaphragm.
The three Steam Generators are 3D-printed cylinders because their main function is damping the motion of the liquid. The external diameter is equal to $d_{SG} = 60$ mm while its height is equal to 239 mm. In reality, they are a complex composition of very small tubes, one near the others, that create damping in the motion from a dynamic point of view of the system. In theory, the porosity is a level of the motion damping imposed by design and can be changed as preferred only by means of a new 3D-manufactured piece. This kind of variability is an add-on useful if one wants to simulate an internal accident in the reactor. In the following test, something like that will be reproduced but removing entirely the three steam generators, because

the lack of time have not allowed to wait for new 3D-printed pieces.
In this model, the pumps are seated to suit the capacitance probes to measure the water height in the hot plenum part. They are in aluminium and on their top are drilled in order to successfully complete the probe installation. The outer diameter is equal to 50.1 mm and the height of the cylindrical corp is equal to 235 mm. As it's shown in Figure 2.5, the pumps present a drilled bottom floor, and the number of holes gives the *pressure drop* ξ aimed. In the real demonstrator, 17.4 tonne/s are flowing through the pumps so each of them bleed 5.8 tonne/s, and a pressure drop of $\Delta P = 1kPa$ can be considered. The singular pressure losses are equal to $\xi = \frac{\Delta P}{1/2\rho w_0^2} = 23.8$, where $\rho = 10570$ kg/m^2 is the density of Pb. In Table 2.2 there's an overview on the plain tube dimensions in the model.
It's not a matter in this work explaining the reasons of this choice as all the other parameters, such as the porosity for example. It's important, instead, highlighting that the pressure drop represents a consistent element in the liquid's dynamic in the model, if it has to be representative of reality. Parameters such as the pressure drop are not going to be changed during the test performed.

Dimensions of cylindrical tubes				
	Diameter [mm]	Height [mm]	Number on the mockup	Goes across diaphragm?
SG	60.0	239	3	Yes
DHR	49.5	223	3	No
Pump	50.1	235	3	Yes

Table 2.2: Main dimensions of the elements of the three triplets: SG, DHR and Pumps; it's highlighted which tube goes across the diaphragm [34]

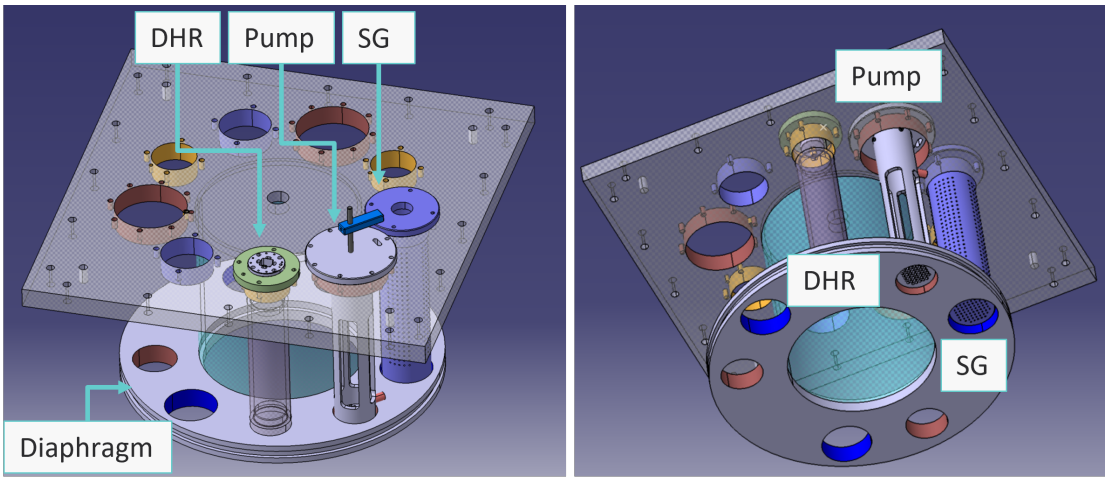

Figure 2.5: CAD drawing of hot plenum of ALFRED's model [34]: it's clear in the drawing that the membrane has six holes in the annulus surface, for suiting the SGs and the Pumps of the three triplets

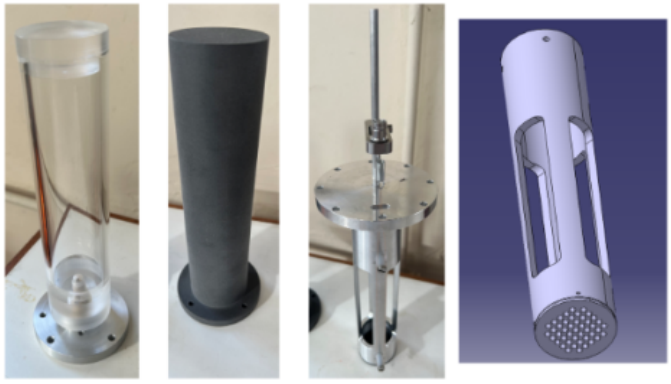

Figure 2.6: Some photos of the DHR, SG and pump used for completing the ALFRED's model [34]); the Figure includes also a CAD model of the Pump to highlight the holes-configuration at the bottom of the tube

2.3 Accelerometers applied on the shaking table

A combination of two different types of accelerometers has been mounted on the shaking table. The primary acceleration measurements system is a proper configuration of six digital accelerometers developed in VKI, and base on the MMA8451Q digital sensor. The accelerometers are applied in a configuration shown in Figure 2.7 to average the acceleration all around the table, and avoiding great interference noise because the table resonance at 12-14 Hz. Before fastening the six small boxes, the surfaces have been cleaned and approximately polished for assuring planar contact. Besides, they must be positioned accordingly to the three axis of the shaking table, which are underlined in Figure 2.9.
The "Octopus" of six accelerometers is connected to the `LabView` interface through an Arduino card by means of a USB port and provides measurement of acceleration. The frequency of data acquisition of the "Octopus" Arduino card is equal to 200 Hz. The secondary acceleration measurements system is a ceramic shear high sensitivity sensor, a *PCB Piezotronics 356B18*. The PCB Piezotronics 356B18 analogic accelerometer is installed on the top surface of the shaking table. The sensor is connected to a NI DAQ 9215, which is the same used for the capacitance probes data acquisition (2.4). The reference system of the acceleration recorded by the PCB sensor is rotated of an $\alpha = 37°35'$ angle with respect to $\{x, y, z\}$ reference system of the table. In Table 2.3 are reported the effective sensitivity along the $\{x, y, z\}$ directions of the PCB accelerometer. The PCB acquires data at a very high frequency of above 2000 Hz, so a post-processing consideration has been done to resolve the contradiction by the means of a resampling of the signals at the lowest acquisition frequency of 200 Hz.

Axis	Sensitivity e_i[mV/g]
x	1037
y	1088
z	1033

Table 2.3: Accelerometer sensitivity [35]: common sensitivity used in the `LabView` program is equal to $e = 1000$ mV/g, so it's necessary to multiply the acquired acceleration in each direction by a factor equal to $e_i/1000$

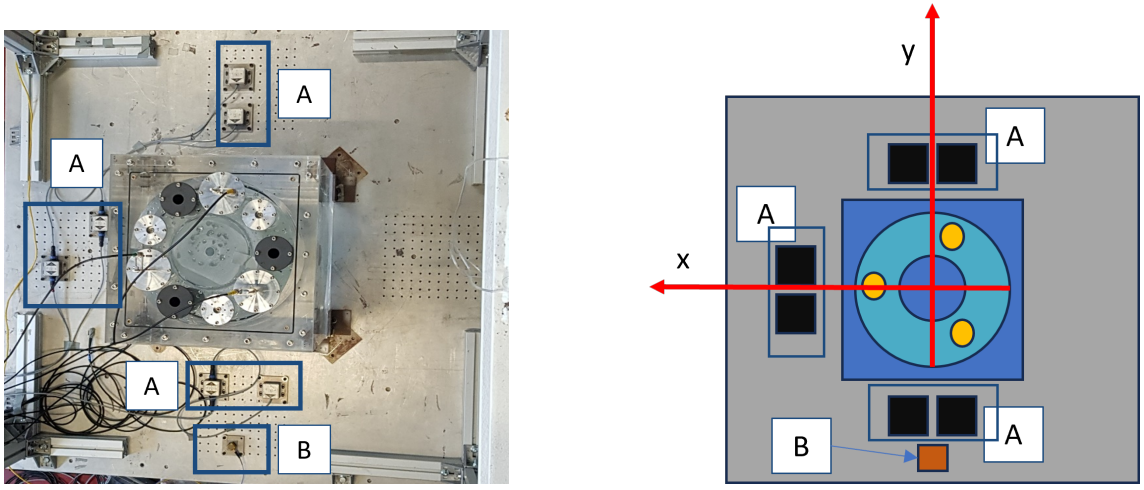

(a) (b)

Figure 2.7: Accelerometers on the table: *A* stands for the MMA8451Q digital sensor [36] in the *octopus configuration*; *B* stands for the PCB

2.4 Capacitance probes

The amplitude of the liquid free surface motion were supposed to be measured with three capacitance probes, which are provided by Artelia group. Each of them is constituted of a single wire of copper attached to a spring at the top of the particular structure of the pump tubes, providing so the preload mechanically, as it can be seen in Figure 2.8. The conductive surface of the wire will start working as a capacitor by the proximity of the water in the hot plenum pool. A simplified scheme is reported in Figure 2.8, while the respective dimensions are reported in Table 2.2 and Table 2.4.

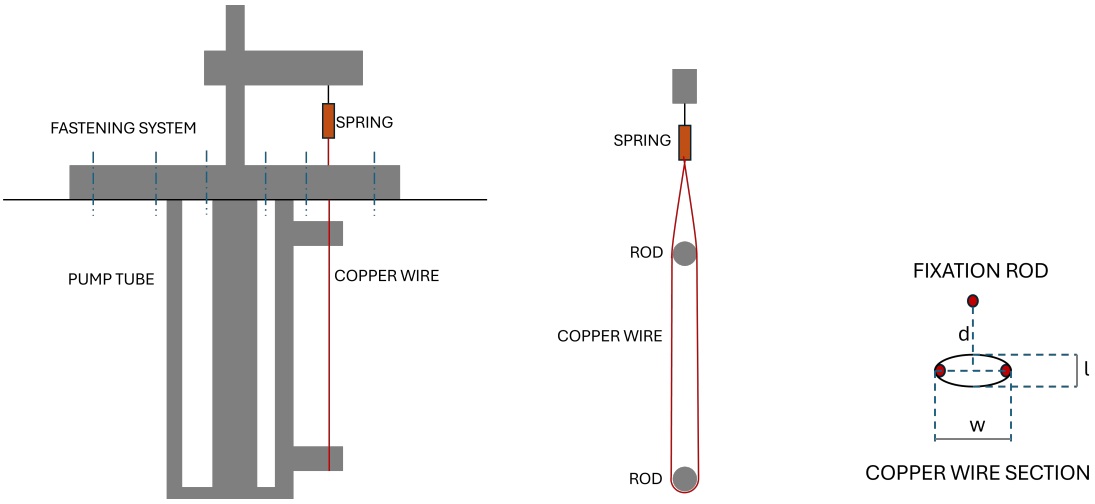

(a) (b) (c)

Figure 2.8: Simplified scheme of the capacitance probes: (a) overview on the pump tube structure, in which the copper wire is mechanically keeps in position by means of a spring; (b) scheme of the copper wire around the pump rigid supports; (c) section of the copper wire

	Probe 0	Probe 1	Probe 2
w [mm]	9	9	9
l [mm]	3	2.25	1
d [mm]	13.4	11.9	13.6

Table 2.4: Probe placement and position uncertainty on the measurement referring to Figure 2.8c

The measurement principle is that the output capacitance is proportional to the part immersed in water of the probe. As it's written in [37], each part of the capacitance probe immersed in water create infinite capacitors in parallel connection. So, the final capacitance is:

$$C(h) \simeq \frac{2\pi\epsilon_r\epsilon_0}{ln(d2/d1)} \sum h_i \tag{2.2}$$

where h_i is the length of probes dived in water; ϵ_r is the relative permittivity of the water in this case; $\epsilon_0 = 8.8542 \times 10^{-12}$ F/m is the permittivity of vacuum; d_1 and d_2 are the diameters of the metal probe and the insulating coating of the cable, respectively. A certain approximation must be kept into account to consider the uncertainty on the measurements of the probes.
A composition of oscillator/integrator connected by BNC permits to measure the evolution of height of the free surface. As the height of the water level increase, the capacitance increase with an increasing of the voltage of the capacitor probes.

For technical reasons, it's preferred that the voltage variation don't exceed the range from -10 V to 10 V. Besides, the DAQ acquires data from the probes at a frequency above 2000 Hz. These sensors are connected to the NI DAQ 9215 to acquire data, also used for the PCB accelerometer.
For each of the three probes, the voltage measurements of the level of water in time is a mean within the two filaments. Table 2.5 provides the location in the $X - Y$ plane of each of the three probes, and it refers to Figure 2.9.

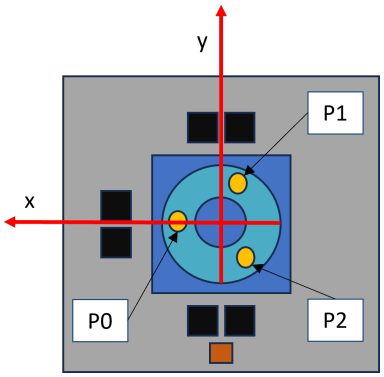

Figure 2.9: Simplified sketch for the probes placement.

	P0	P1	P2
x [mm]	-154	+69.0	+104
y [mm]	-19.0	+154	-84.0

Table 2.5: Probe placement on the $X - Y$ plane, referring to the Cartesian reference frame in Figure 2.9

Other measurements techniques could be applied and used for monitoring the free surface of the liquid in the tank, as was done in the previous years ([9] and [20]). The detection of the free surface motion can be recorded by means of no-intrusive ways, such as by Level Detection and Recording (LeDaR) in 2D or by Reference Image Topography (RIT) in 3D.

2.5 Uncertainty on the probes' measurement

2.5.1 Calibration of the capacitance probes

The three probes were calibrated by filling up the empty tank with the distilled water. In particular, the lower part of the ALFRED model until the porosity section has been filled faster than the last part of it. On the contrary, the upper part that includes the nine cylinder seats and the inner cylinder has been filled very carefully, because the probes has been measured an increasing level of water starting from zero values.

Each 5mm as been taken a series of measurement from the three probes until the top of the model; then, the water has been drawn in the same way as before, so taking also the measurements each 5 mm. This process has been stopped until the desired level height has been reached. The level depends on which initial condition of water depth is requested, taking in account also that the plain tubes occupy volumes in the hot plenum representation, as they are basically dumping elements. The measures for each level has been taken with a `LabView` code that read the voltage for some seconds from the probes. In Figure 2.10 can be seen that there's a measurement in voltage for each of the time step in a time range from 0 seconds to 4 seconds. Starting from this picture, it's clear that something it's not working properly with the P0 sensor.
It's fundamental to notice that all the height used for compiling the calibration filenames are taken from a regular ruler attached to the model. The reference system in this case is from the top to the bottom of the hot plenum pool, so the raw data in voltage of each of the file are referred to a height measure that has to be properly post processed.
Those files and their contents are then post processed by means of a code written, created by Jean Muller, in `Python` environment. The code applies a Monte Carlo method to estimate the uncertainty on the height measurements of water depth, using 50000 points on the *Probability Density Function* extracted from the raw data.

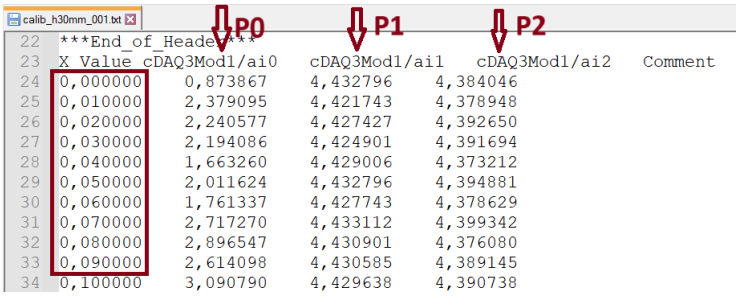

Figure 2.10: Calibration file *.csv* architecture: is outlined the time step of acquisition data, the column relative to the raw data measured from the three probes P0, P1 and P2; the final time step is equal to 4 seconds

2.5.2 Initial uncertainty budget

Calibration is normally taken as a systematic error source, and knowing that the uncertainty propagates from direct measurement (in voltage V from the probes measurements) to the derived quantities (in mm), a Monte Carlo method has been chosen to compute this propagation. The calibration is completed to find the best fit for a linear fit of the output, given in Voltage V by the probes, in function of the height. The standard that has been taken as a reference is the *ASME PTC 19.1, 2018* [32]. The MCM allows taking to account correlated uncertainty sources automatically,

without providing a simplified formulation for the propagation of the errors. For example, if compared to a Taylor series expansion the MCM makes no assumption on input and output *Power Density Function* and, above all, doesn't require linearization, while the first above-mentioned method assumes Gaussian output PDF and requires linearization of the measurement system. Using 50000 repetition in the Monte Carlo should allow having a good fit for the calibration law.
The code used for the application of the MCM has been written by Jean Muller and properly modified to ask in output the calibration law linear fit. An overview of the code is provided in the Appendix B. The code performs 50000 repetition of the Monte Carlo method on the Probability Density Function extracted form the *csv* file previously indicated.
For each probe a mean value for the slope m_i of the curve, its intercept q_i and their standard deviation δm_i and δq_i has been found. The law for each $i - probe$ is the following,

$$h_i = m_i \times V_i + q_i \tag{2.3}$$

with h_i the free surface height (mm), V_i the output voltage (V) and m_i and q_i the fitting couple.
The uncertainty is computed as follows,

$$u_{h_i} = max(\sqrt{A^2 + B^2 + C^2}) \tag{2.4}$$

with

$$\begin{cases} A = V \times \delta m \\ B = \delta q \\ C = m \times \delta V \end{cases} \tag{2.5}$$

δm and δq go out from the Monte Carlo, V is considered within $[-10, 10]$ V and δV is the smallest measurable value of voltage, equal to $20/2^{16}$ for the NI DAQ 9215.
In Table 2.6 and 2.7 there are the results for the first and the last calibration concerning the first experimental campaign. It was necessary to confirm the consistency of the data from the probes after the P0 sensor revealed to faulting and some of the BNC cables have been changed on October 30, so the first fitting law is used for the test series until that date.

Probe	m[mm/V]	q[mm]	δm	δq	u_{h_i}[mm]
0	-18.3406	78.7737	0.0321	0.1609	0.3592
1	-18.2275	104.4165	0.0282	0.0893	0.2957
2	-18.6136	1048.1397	0.0293	0.0894	0.3066

Table 2.6: Calibration table for linear fitting of the 1D height measurement of the capacitance probes-results from the October 10, 2023

Probe	m[mm/V]	q[mm]	δm	δq	u_{h_i}[mm]
0	-17.2128	86.3444	0.4398	1.7984	4.7518
1	-18.9240	109.5946	0.0284	0.0828	0.2962
2	-19.2108	109.4787	0.0297	0.0873	0.3092

Table 2.7: Calibration table for linear fitting of the 1D height measurement of the capacitance probes-results from the November 6, 2023

In spite of the computed intercepts for the linear fit, what really matter are the slope coefficient because the sloshing problem of the free surface motion will be studied by means of non-dimensional amplitude $\zeta = \frac{h_i - (still\ water\ depth)}{non\ dimensional\ parameter}$. Besides, the reference system for height measurement used in the Monte Carlo method it's not the same used for studying the dynamic system; in particular, that intercept and that slope refers to a coordinate system from the top to the bottom of the tank, so indicates minor h_i when the water level increases. In Figure 2.11 a post-processed representation of the calibration fitting law is proposed.

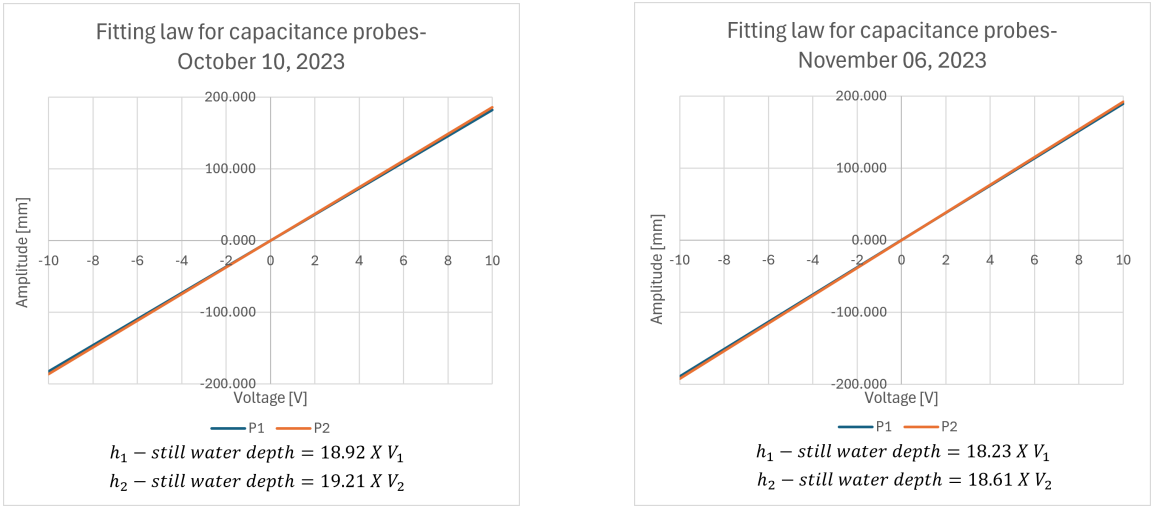

(a) (b)

Figure 2.11: (a) Fitting curve for the calibration results of October 10, 2023, used in test until; (b) Fitting curve for the calibration results of November 06, 2023

2.5.3 Total uncertainty budget

The total uncertainty budget is computed summing up the initial uncertainty budget from the Monte Carlo method and an experimentally uncertainty related to the shake table. Repeatability test has been consisted of six test series, equal to each other for the sinusoidal input signal at 0.71 Hz, and a level of confidence of 95% from a two-sides Student's t-distribution is considered. Table 2.8 the total uncertainty budget is presented for the probes P1 and P2.

Calibration of October 10, 2023			
Probe	u_{i-MC}[mm] initial budget	$u_{i-TABLE}$[mm]	u_i[mm]
P1	0.296	1.056	1.352
P2	0.307	0.993	1.300
Calibration of November 6, 2023			
Probe	u_{i-MC}[mm] initial budget	$u_{i-TABLE}$[mm]	u_i[mm]
P1	0.296	1.056	1.352
P2	0.309	0.993	1.302

Table 2.8: Total uncertainty on the probes measurements:
$u_{i-TOTAL} = u_{i-MC} + u_{i-TABLE}$

2.6 Complete setup

In Figure 2.13a is shown the top view. The darker cylinders are the steam generators in 3D-printed material, removable or replaceable if a changed of porosity is wanted to be performed. Also in Figure 2.13a can be seen the capacitance probes, while the remaining three seats can be suited for the addition of strain gauge sensors. In confirmation of what has already been written, the order in the position of three triplets, counting the 3D-printed ones, the capacitance probes and the possible seats for strain gauge it's respected in accordance to the CAD model (Figure 2.4 and Figure 2.5).
In figure 2.13b an oversight of the complete operating facility is shown. A high-speed camera *Dantec - SpeedSense M310* camera was positioned at a proper distance from the shaking table for catching the free surface motion of this special case study. The acquisition resolution was set to 768 pixels*576 pixels and the frame rate was of 50 frame per second. The camera was not fitted for capturing quantitative amplitude of the free surface motion, but only for identifying the sloshing resonance modes and capturing non-linear phenomenon. Behind the ALFRED mockup is collocated a large sheet of translucent paper, which filtrates the light of a square white LED device for providing a uniform illumination.
The central PC is connected with a special interface to the shaking table, providing a specific Control Bench Unit of the facility. From the interface, the proper status of the facility can be checked and managed if needed. Besides, all the input file are loaded there, with all the limitation that the software imposes for a correct test performance. It's noticed that all the signal used to catch significant results respect those limitations, otherwise the confidence of the results became really unacceptable. For example, one of the major issue has been creating proper input signals that don't abruptly stop the movements of the shaking table's plates or give a shock to the dynamic system with unexpected high accelerations. It has been really challenging the setting up of the sampling frequency of the input file and the correct correlation with the table's reading frequency of the input signal.

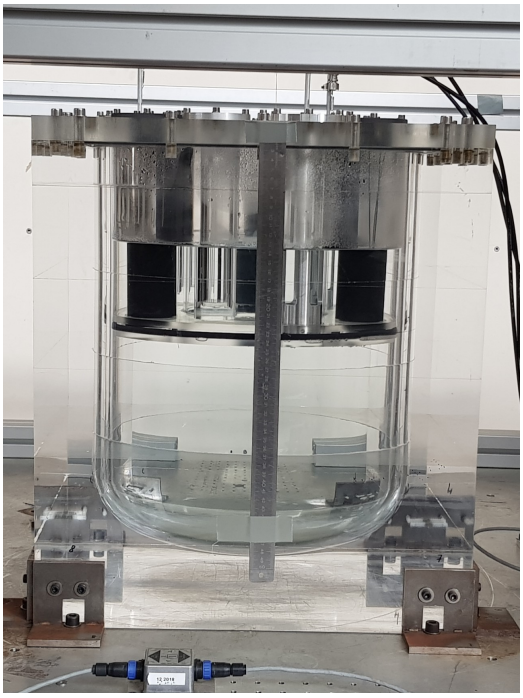

(a)

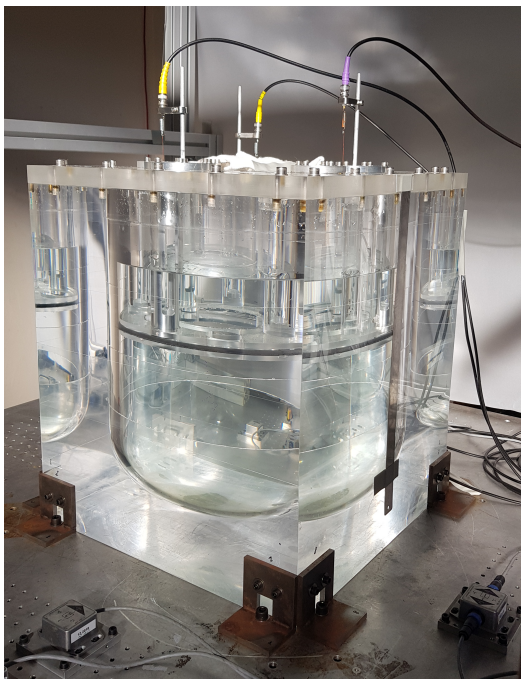

(b)

Figure 2.12: ALFRED model mounted on the shaking table: (a) mockup with the 3 SG installed; The model is provided with a ruler on the side to measure the water depth each time that it needs to be changed. (b) mockup without the 3 SG for simulating a changing porosity of the internal structure due to an accident simulation

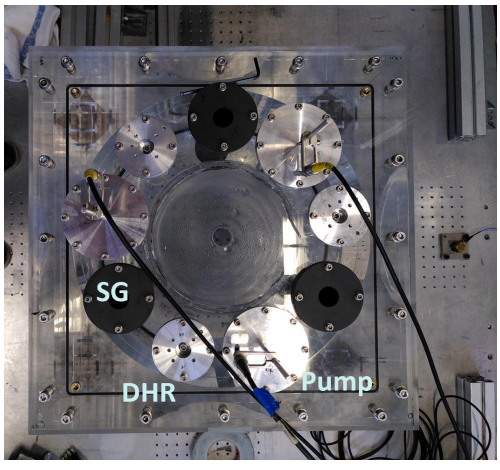

(a)

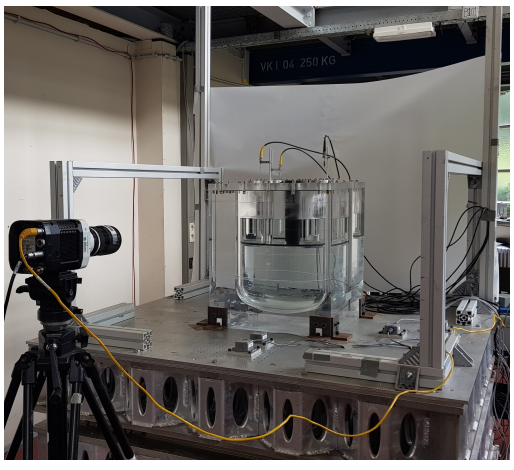

(b)

Figure 2.13: ALFRED model mounted on the shaking table: (a) top view. (b) a front view of the lab facility

2.7 Creation of the input signal

2.7.1 Horizontal base excitation input signal

Horizontal input harmonic signal has been created in such a way that the maximum amplitude of the free-liquid surface is captured from the P1 sensor alongside Y-direction of the Cartesian reference frame in Figure 2.9.
Harmonic base excitation in one DoF input signal has been created with the code in D. The harmonic excitation selected has the following form:

$$a(t) = a_y \sin(\omega_y t) \tag{2.6}$$

where a_y is the amplitude of the external excitation and $\omega_y = 2\pi f_y$ where f_y is the forcing pulsation.
Three types of 1 DoF signal for the harmonic base excitation have been created for the following forcing amplitude:

- $a_y = 5$ mm;
- $a_y = 15$ mm;
- $a_y = 30$ mm.

Forcing frequencies f_y are selected near/at and away from the first natural frequency of the free-liquid surface of ALFRED a CFD model [34] predicted:

$$f_1 = 0.89\,\text{Hz} \tag{2.7}$$

The internal structure adds damping to the motion and makes impossible to compare ALFRED's model to one of the nearest theoretical configuration of the problem, exposed in the Eq. 1.11. The harmonic base excitation in the form of Eq. 2.6 leads to the following definition of the horizontal acceleration:

$$a(t) = a_y \sin(\omega_y t) \implies \ddot{a}_y(t) = a_y(t) \cdot \omega_y^2 \tag{2.8}$$

Maximum acceleration occurs when $\sin(\omega_y t) = 1$. The shaking table mechanics limitations, which are mostly due to the type of hydraulic actuators, have required some precaution about the acceleration imposed to each of the three moving plates in X-Y-Z direction (Figure 2.1b). The input signal is created with initial and ending ramps whom duration is equal both of 10 seconds. The most interesting central part of the signal lasts 60 s and it represents the full-regime oscillation of the input signal. Figure 2.14 represents the input signals provided to the table in terms of position $a(t)$ in function of the time array varying the forcing amplitude. The time array was constructed using a constant step size of $dt = \frac{1}{f_{SAMPLING}} = \frac{1}{200Hz} = 0.005$ s.

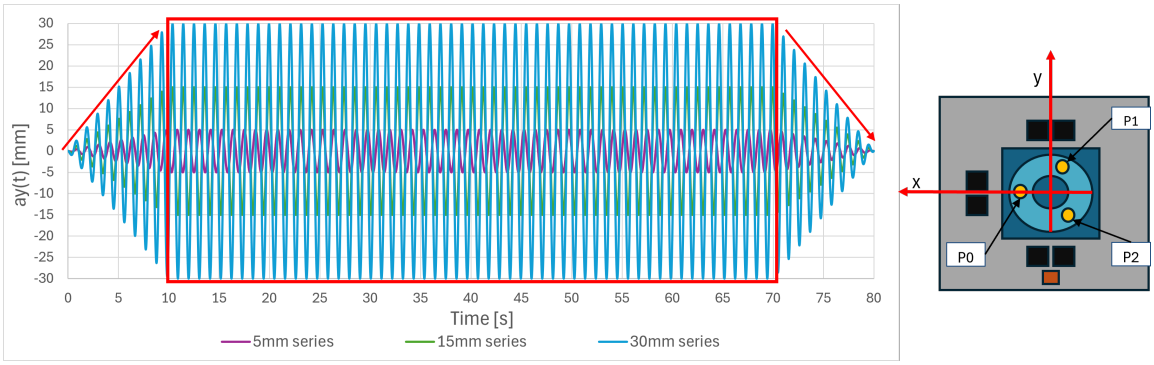

Figure 2.14: Input signal in 1 DoF alongside Y direction for forcing amplitude equal to $a_y = 5, 15, 30$ mm and $f_y = 0.94$ Hz; the sampling frequency is equal to the reading frequency from the shaking table, $f_{SAMPLING} = 200$ Hz; the physical signal is within the time range [10,70] s.

2.7.2 Norm base earthquake signals

Earthquake simulations' input signal have been taken from the norm IEC 60068-3-3, which have been modified by the research engineer Jean Muller at the time of the test. The required response spectrum is in Figure 2.15 and the input signal is scaled to respect the soil and seismic characterization of Mioveni (Romania), where the reactor is gonna be built. The zero period acceleration is equal to

$$a_t = a_g \times K \times D \times D \times \alpha \times G \tag{2.9}$$

where the following choices weren't made by the author but are the results of agreements within VKI in the PASCAL framework:

- wave factor $\alpha = 1$;
- geometric factor $G = 1$;
- superelevation factor $K = 1$ because the reactor is mounted on rigid fixation;
- direction factor $D = 1$;
- ground acceleration $a_g = 1\,\mathrm{m/s^2}$.

The ground acceleration a_g was selected knowing that the region of interest is a zone 1 for seismic activities. The damping ratio in the response spectra is chosen equal to 5% to have a maximum value of the acceleration equal to three times a_t and a frequency range within $f_1 = 1$ Hz and $f_2 = 35$ Hz. In Figure 2.15 the required response spectra is plotted: the entire acceleration is developed within f_1 and f_2, while the plateau at the maximum value is within $2f_1 = 2$Hz and $\frac{1}{3}f_2 = 11.7$ Hz.
From the similarity studies (§2.2.1) a frequency scaling should be necessary to fulfil the dynamic similarities, but this would mean input signal in terms of position that impose too higher acceleration on the shake table and, at the same time, frequency of no interest for the sloshing investigation. Existing `MATLAB` codes generates the accelerogram from the non-scaled power spectral density of the norm, then a Newmark

baseline correction (`MATLAB` code manual) is applied because an unrealistic mean shift occurs at the end of the input signal between 15 seconds and 20 seconds.
The input signal is in figure 2.16. The nominal one presents a displacement within 0.4 mm and -0.7 mm, but to see interesting sloshing dynamics a more energetic case is considered multiplying the amplitude by five times and ten times.

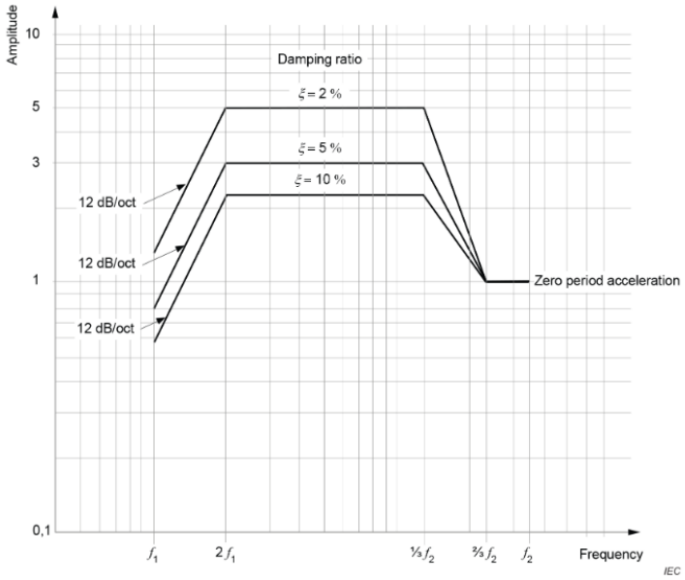

Figure 2.15: Required response spectrum in generalized form taken from IEC 60068-2-57 for vibration test, time-history and sine-beat method. Curve at damping ratio $\xi = 5\%$ is selected for having three times the zero period acceleration a_t.

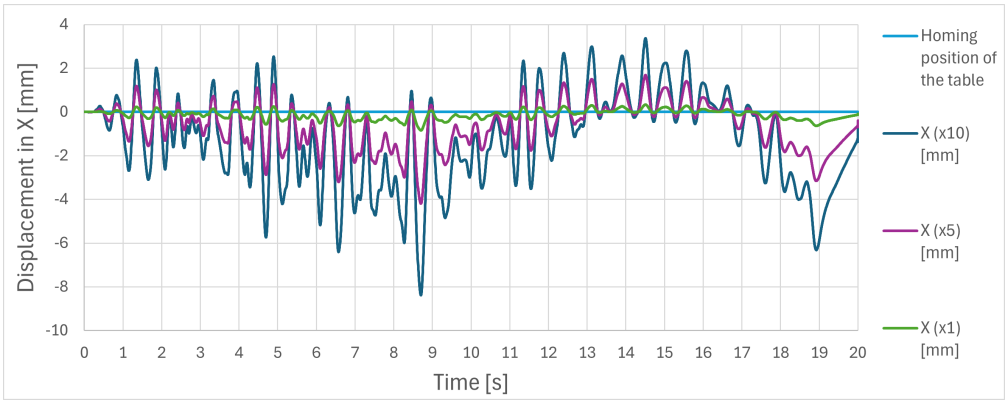

Figure 2.16: Norm base signal after the baseline correction. The Figure presents the varying amplitude multiplied by one, five and ten, which is the most energetic case.

An additional shifting in frequency is applied because the previous signal excites the free-liquid surface motion at higher frequencies than the estimated numerical equal to 0.89 Hz [34]: the entire acceleration is developed within f_1 and f_2, while the

plateau at the maximum value is within $2f_1 = 0.89$ Hz and $\frac{1}{3}f_2 = 11.4$ Hz. Figure 2.17 presents the shifting to 0.89Hz of the norm signal and Figure 2.18 presents the actual input signal following the same procedure indicated for the non-shifted case.

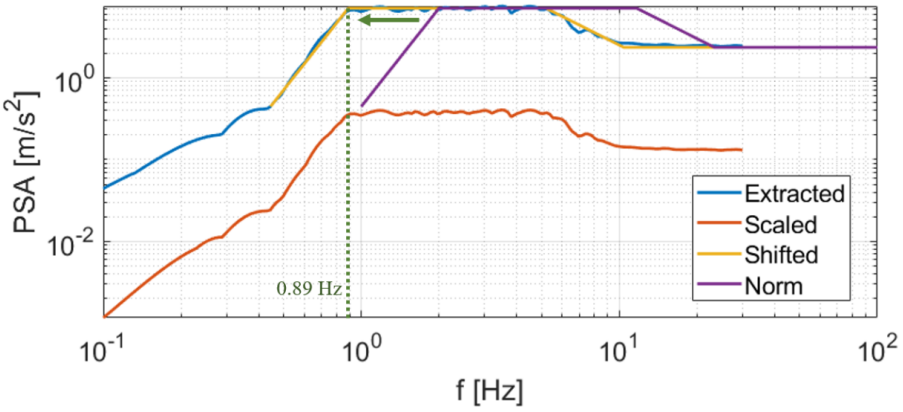

Figure 2.17: Pseudo spectral acceleration from the norm following a scaling due to model similarities and a frequency shifting due to experimental necessity to study sloshing dynamics in ALFRED's model.

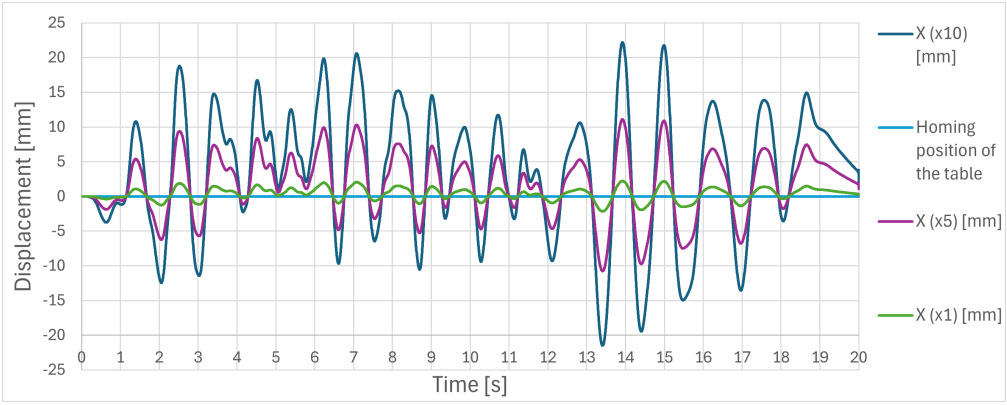

Figure 2.18: Norm base signal after the baseline correction and PSA acceleration shifting close to $f = 0.89$ Hz. The Figure presents the varying amplitude multiplied by one, five and ten, which is the most energetic case and intense sloshing.

2.8 Matrix of performed test series

In the current section the test matrix is presented.

Horizontal harmonic base excitation				
DoF	Forcing frequency	Forcing amplitude	Internal structure	Water depth
1 DoF in y	$f_y = 0.68$Hz	$a_y = 5, 15, 30$mm	3SG config. no 3SG config.	h=5.00,6.50,7.84, 8.84,9.90cm
1 DoF in y	$f_y = 0.78$Hz	$a_y = 5, 15, 30$mm	3SG config. no 3SG config.	h=5.00,6.50,7.84, 8.84,9.90cm
1 DoF in y	$f_y = 0.82$Hz	$a_y = 5, 15, 30$mm	3SG config. no 3SG config.	h=5.00,6.50,7.84, 8.84,9.90cm
1 DoF in y	$f_y = 0.84$Hz	$a_y = 5, 15, 30$mm	3SG config. no 3SG config.	h=5.00,6.50,7.84, 8.84,9.90cm
1 DoF in y	$f_y = 0.845$Hz	$a_y = 5, 15, 30$mm	3SG config. no 3SG config.	h=5.00,6.50,7.84, 8.84,9.90cm
1 DoF in y	$f_y = 0.85$Hz	$a_y = 5, 15, 30$mm	3SG config. no 3SG config.	h=5.00,6.50,7.84, 8.84,9.90cm
1 DoF in y	$f_y = 0.86$Hz	$a_y = 5, 15, 30$mm	3SG config. no 3SG config.	h=5.00,6.50,7.84, 8.84,9.90cm
1 DoF in y	$f_y = 0.68$Hz	$a_y = 5, 15, 30$mm	3SG config. no 3SG config.	h=5.00,6.50,7.84, 8.84,9.90cm
1 DoF in y	$f_y = 0.90$Hz	$a_y = 5, 15, 30$mm	3SG config. no 3SG config.	h=5.00,6.50,7.84, 8.84,9.90cm
1 DoF in y	$f_y = 0.94$Hz	$a_y = 5, 15, 30$mm	3SG config. no 3SG config.	h=5.00,6.50,7.84, 8.84,9.90cm
1 DoF in y	$f_y = 0.98$Hz	$a_y = 5, 15, 30$mm	3SG config. no 3SG config.	h=5.00,6.50,7.84, 8.84,9.90cm
1 DoF in y	$f_y = 1.04$Hz	$a_y = 5, 15, 30$mm	3SG config. no 3SG config.	h=5.00,6.50,7.84, 8.84,9.90cm
1 DoF in y	$f_y = 1.08$Hz	$a_y = 5, 15, 30$mm	3SG config. no 3SG config.	h=5.00,6.50,7.84, 8.84,9.90cm
1 DoF in y	$f_y = 1.12$Hz	$a_y = 5, 15, 30$mm	3SG config. no 3SG config.	h=5.00,6.50,7.84, 8.84,9.90cm
1 DoF in y	$f_y = 1.20$Hz	$a_y = 5, 15, 30$mm	3SG config. no 3SG config.	h=5.00,6.50,7.84, 8.84,9.90cm
1 DoF in y	$f_y = 1.38$Hz	$a_y = 5, 15, 30$mm	3SG config. no 3SG config.	h=5.00,6.50,7.84, 8.84,9.90cm
1 DoF in y	$f_y = 1.54$Hz	$a_y = 5, 15, 30$mm	3SG config. no 3SG config.	h=5.00,6.50,7.84, 8.84,9.90cm

Table 2.9: Horizontal harmonic base excitation in 1 DoF test matrix; nineteen forcing frequencies around near/at and away $f = 0.89$ Hz are selected; forcing amplitude tested $a_y = 5, 15, 30$ mm; internal structure with and without the 3SG; water depths tested $h = 5.00, 6.50, 7.84, 8.84, 9.90$ cm.

Harmonic base excitation in sway and pitch				
DoF	Forcing frequency	Forcing amplitude	Internal structure	Water depth
2 DoF in y and z	$f_y = 0.68$Hz $f_z = 2.23$Hz	$a_y = 15, 30$mm	3SG config. no 3SG config.	h=8.84cm
2 DoF in y and z	$f_y = 0.78$Hz $f_z = 2.23$Hz	$a_y = 15, 30$mm	3SG config. no 3SG config.	h=8.84cm
2 DoF in y and z	$f_y = 0.82$Hz $f_z = 2.23$Hz	$a_y = 15, 30$mm	3SG config. no 3SG config.	h=8.84cm
2 DoF in y and z	$f_y = 0.84$Hz $f_z = 2.23$Hz	$a_y = 15, 30$mm	3SG config. no 3SG config.	h=8.84cm
2 DoF in y and z	$f_y = 0.845$Hz $f_z = 2.23$Hz	$a_y = 15, 30$mm	3SG config. no 3SG config.	h=8.84cm
2 DoF in y and z	$f_y = 0.85$Hz $f_z = 2.23$Hz	$a_y = 15, 30$mm	3SG config. no 3SG config.	h=8.84cm
2 DoF in y and z	$f_y = 0.86$Hz $f_z = 2.23$Hz	$a_y = 15, 30$mm	3SG config. no 3SG config.	h=8.84cm
2 DoF in y and z	$f_y = 0.68$Hz $f_z = 2.23$Hz	$a_y = 15, 30$mm	3SG config. no 3SG config.	h=8.84cm
2 DoF in y and z	$f_y = 0.90$Hz $f_z = 2.23$Hz	$a_y = 15, 30$mm	3SG config. no 3SG config.	h=8.84cm
2 DoF in y and z	$f_y = 0.94$Hz $f_z = 2.23$Hz	$a_y = 15, 30$mm	3SG config. no 3SG config.	h=8.84cm
2 DoF in y and z	$f_y = 0.98$Hz $f_z = 2.23$Hz	$a_y = 15, 30$mm	3SG config. no 3SG config.	h=8.84cm
2 DoF in y and z	$f_y = 1.04$Hz $f_z = 2.23$Hz	$a_y = 15, 30$mm	3SG config. no 3SG config.	h=8.84cm
2 DoF in y and z	$f_y = 1.08$Hz $f_z = 2.23$Hz	$a_y = 15, 30$mm	3SG config. no 3SG config.	h=8.84cm
2 DoF in y and z	$f_y = 1.12$Hz $f_z = 2.23$Hz	$a_y = 15, 30$mm	3SG config. no 3SG config.	h=8.84cm
2 DoF in y and z	$f_y = 1.20$Hz $f_z = 2.23$Hz	$a_y = 15, 30$mm	3SG config. no 3SG config.	h=8.84cm
2 DoF in y and z	$f_y = 1.38$Hz $f_z = 2.23$Hz	$a_y = 15, 30$mm	3SG config. no 3SG config.	h=8.84cm
2 DoF in y and z	$f_y = 1.54$Hz $f_z = 2.23$Hz	$a_y = 15, 30$mm	3SG config. no 3SG config.	h=8.84cm

Table 2.10: Combined harmonic base excitation in 2 DoF test matrix; nineteen forcing frequencies around near/at and away $f = 0.89$ Hz are selected; forcing amplitude tested $a_y = 15, 30$ mm; internal structure with and without the 3SG; water depths tested $h = 8.84$ cm.

Earthquake test series				
DoF	Forcing frequency	Forcing amplitude	Internal structure	Water depth
1 DoF in x	Around f natural	×5	3SG config.	h=5.00,6.50,7.84, 8.84,9.90cm
1 DoF in x	Around f natural	×10	3SG config.	h=5.00,6.50,7.84, 8.84,9.90cm
1 DoF in x	Norm scaled	×1	3SG config.	h=5.00,6.50,7.84, 8.84,9.90cm
1 DoF in x	Norm scaled	×5	3SG config.	h=5.00,6.50,7.84, 8.84,9.90cm
1 DoF in x	Norm scaled	×10	3SG config.	h=5.00,6.50,7.84, 8.84,9.90cm
All 3 DoF	Norm scaled shifted	×1	3SG config.	h=5.00,6.50,7.84, 8.84,9.90cm
All 3 DoF	Norm scaled shifted	×5	3SG config.	h=5.00,6.50,7.84, 8.84,9.90cm
All 3 DoF	Norm scaled shifted	×10	3SG config.	h=5.00,6.50,7.84, 8.84,9.90cm
1 DoF in x	Norm scaled	×1	no 3SG config.	h=8.84cm
1 DoF in x	Norm scaled	×5	no 3SG config.	h=8.84cm
1 DoF in x	Norm scaled	×10	no 3SG config.	h=8.84cm
All 3 DoF	Norm scaled shifted	×1	no 3SG config.	h=8.84cm
All 3 DoF	Norm scaled shifted	×5	no 3SG config.	h=8.84cm
All 3 DoF	Norm scaled shifted	×10	no 3SG config.	h=8.84cm
2 DoF in y and z	$f_y = 1.20$Hz $f_z = 2.23$Hz	$a_y = 15, 30$mm	3SG config. no 3SG config.	h=8.84cm
2 DoF in y and z	$f_y = 1.38$Hz $f_z = 2.23$Hz	$a_y = 15, 30$mm	3SG config. no 3SG config.	h=8.84cm
2 DoF in y and z	$f_y = 1.54$Hz $f_z = 2.23$Hz	$a_y = 15, 30$mm	3SG config. no 3SG config.	h=8.84cm

Table 2.11: PASCAL sloshing framework input signals, taken from the norm; 1 DoF and 3 DoF signals with the amplitude multiplied by 1, 5 and 10 times the scaled signal; changing water has been tested only in the 3SG configuration; no 3SG configuration has been tested only for water depth $h = 8.84$ cm.

Chapter 3

Harmonic base excitation

This chapter presents results and observation on the reference test series obtained from the performed test for the smallest forcing amplitude applied $a_y = 5$ mm in direction y for forcing frequencies near/at $f = 0.89$ Hz. The results for test series using the same 1 DoF harmonic base excitation signal but at different forcing amplitude, water depth in the model and in hazard condition removing the three steam generators from the experimental setup are presented and are compared each other. Time histories, phase plane plots and Fast Fourier Transform (FFT) are the tools for studying the investigation of sloshing processes in the ALFRED's model. Captures of the video taken with the *Dantec* camera are used to confirm the post-processed information. `Python` codes for post processing are used as well as spreadsheets for the data collection.
The fundamental parameter for the investigation of sloshing is the dimensionless forcing acceleration κ_y, equal to:

$$\kappa_y = \frac{a_y \omega_y^2}{g} \tag{3.1}$$

where $g = 9.81\,\mathrm{m/s^2}$ is the gravitational acceleration, a_y the external forcing amplitude and ω_y is the forcing pulsation.

3.1 Basic reference test series

The horizontal harmonic base excitation with a forcing amplitude equal to $a_y = 5$ mm is selected as the test series of reference. The selected free-liquid surface height in the nuclear pool reproduction is equal to the nominal one $h = 8.84$ cm, according to the similarity with the actual demonstrator (§2.2.1). It is the starting point of the experimental investigation of the ALFRED's model, because it's the reference to which compares all the other horizontal harmonic series in 1 DoF. It's also a reference for all the other harmonic series and the earthquakes' simulation events studied in this thesis.
The investigation starts with the plots for the maximum amplitude ζ_{max} reached from the free liquid surface during the test at different forcing frequencies, which are listed in Table 2.9 in §2.8. The plots are built taking in account the total uncertainty on the measurement, due to the single probe and to the shaking table displacement (§2.4), and the capacitance laws obtained after the Monte Carlo method. Taking in account the frequency that gives back the maximum amplitude response equal to

$f_1 = 0.98$ Hz, then ζ_{max} is plotted as a function of the frequency ratio f_y/f_1 in Figure 3.1.
Data from the P1 gives back relevant results about the real maximum amplitude reached during the sloshing phenomena because it takes the actual peak of the waves. Data from the P2 gives back a hint of when the swirling regime modes starts to initiates, so when another natural frequency is going to be experimentally reached. Maximum wave amplitude is reached for $f_y/f_1 = 1$. where $f_y = 0.98$ Hz, and doesn't occur for $f = 0.89$ Hz, as it would be expected by the numerical studies of reference. The right-shifting of the maximum elevation in function of the frequency ratio is an indication of starting nonlinear phenomena.
The test series is then analyzed selecting the following investigation points: point **AR1** at $f_y/f_1 = 0.796$ and $f_y = 0.78$ Hz; points **NR** from 1 to 3 at f_y/f_1 =0.898, 0.918, 0.959 and f_y=0.88 Hz, 0.90Hz, 0.94Hz approaching the greater maximum amplitude; point **R** at $f_y/f_1 = 1.000$ and $f_y = 0.98$ Hz at the higher amplitude; point **AR2** at $f_y/f_1 = 1.061$ and $f_y = 1.040$ Hz.

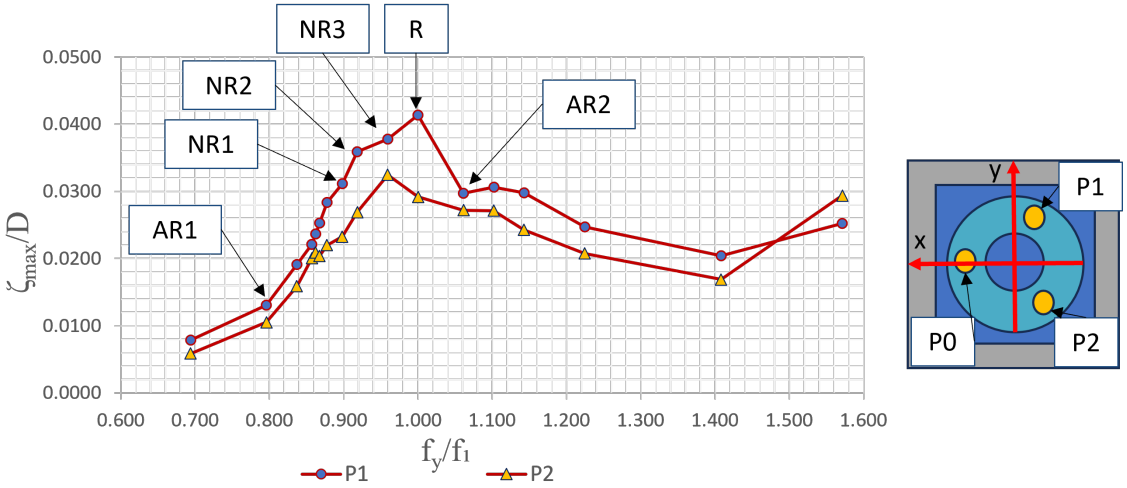

Figure 3.1: Maximum amplitude plot for horizontal harmonic base excitation in Y direction in function of the frequency ratio f_y/f_1 when $a_y = 5$ mm ($a_y/D = 0.013$); point AR1 for $f_y/f_1 = 0.796$, NR1 for $f_y/f_1 = 0.898$, NR2 for $f_y/f_1 = 0.918$, NR3 for $f_y/f_1 = 0.959$, R for $f_y/f_1 = 1.000$ and AR2 for $f_y/f_1 = 1.061$.

3.1.1 Forcing frequency 0.78 Hz

In the point AR1 the forcing frequency is equal to $f_y = 0.78$ Hz, so from Eq. 3.1 the dimensionless forcing acceleration is equal to $\kappa_y = 0.0122$. The time evolution of the free-liquid surface motion is shown for ten seconds in Figure 3.2, not taking into account the starting ramp effect. Time histories plots are made dimensionless multiplying the time variable per the pulsation $\omega_1 = 2\pi f_1$, where $f_1 = 0.98$ Hz is the frequency at higher wave amplitude. For the current forcing frequency, time

evolution confirms a semi-periodic motion, where the P1 presents peaks when the P2 presents troughs because of the position of the probes.

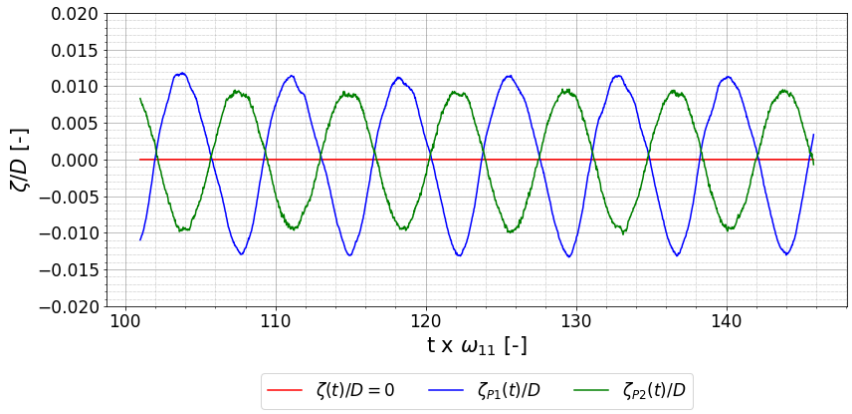

Figure 3.2: Dimensionless time histories for the horizontal harmonic base excitation $a_y = 5$ mm, $f_y/f_1 = 0.796$ and $f_y = 0.78$ Hz; blue is assigned to the P1 signal, while green the P2 signal

In Figure 3.3 the video captures for an analogue test series performed in the x-direction are shown. The video had been taken before noticing the faulting of the P0 sensor, but are useful to highlight the modal forms. At the current forcing frequency $f = 0.78$ Hz and for $a_y = 5$ mm a semilinear behaviour is experienced and the modal form is similar to the first sloshing mode, despite the small amplitudes.

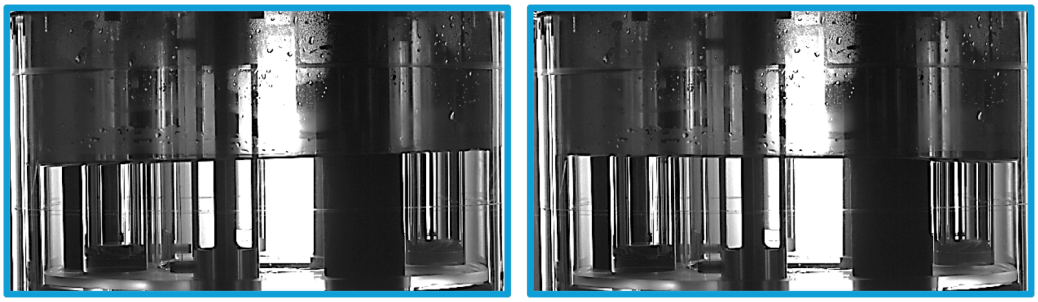

Figure 3.3: Video captures of the model's pool from the $f = 0.78$ Hz and $a_y = 5$ mm test series but performed in the x-direction to see modal forms: semi-linear first sloshing mode is outlined, but the amplitudes are very small

The studies are conducted by means also of *Fast Fourier Transform* (*FFT*), so by *Power Spectral Density* (*PSD*). In Figure 3.4 the PSD associated to the regime signal is shown. The primary peak is at the forcing amplitude frequency ratio of 0.796, while the secondary ones are multiples of the forcing frequency. The low resolution (frequency step ≈ 0.02) is not enough to formally identify the nonlinear frequency components, despite secondary peaks at low energy are attended since the phenomenon is nonlinear.

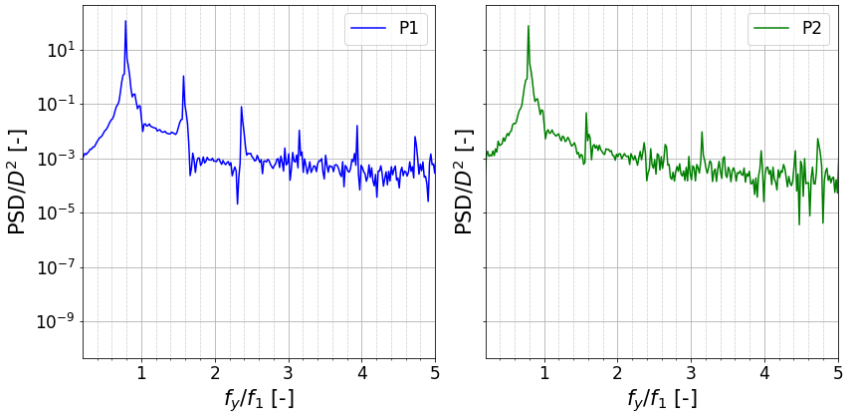

Figure 3.4: Power Spectral Density for the horizontal harmonic base excitation $a_y = 5$ mm, $f_y/f_1 = 0.796$ and $f_y = 0.78$ Hz; while the x-axis are shown until $f_y/f_1 = 5$; peaks are at the forcing amplitude multiples.

Phase plane plots are also used in the formulation proposed in [20]: for each time instant t_i, $\zeta(t_i) = \zeta(t_i + \tau)$ by calculating the mutual information of the attractor, where the $\tau = 0.05$ value has been chosen to have a good resolution of the curves. The phase plots typically show circular, clear and regular orbit in case of linear motion, and asymmetric ones in case of nonlinear free-liquid surface motions.

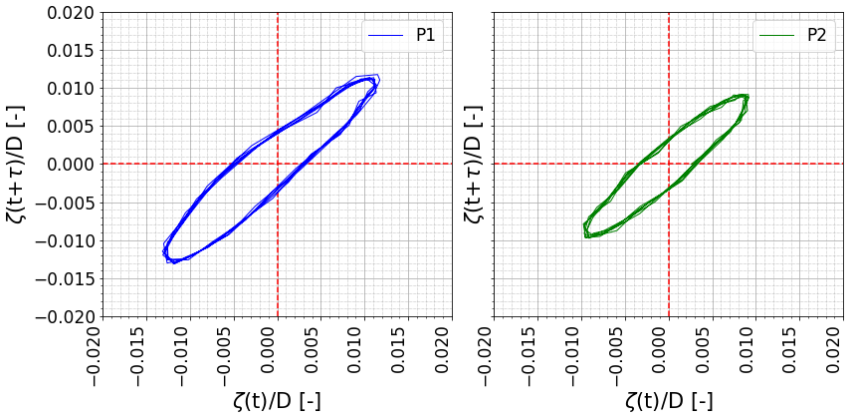

Figure 3.5: Dimensionless phase plane plots for the horizontal harmonic base excitation $a_y = 5$ mm, $f_y/f_1 = 0.796$ and $f_y = 0.78$ Hz; skewness already in the lower forcing amplitude test series for low forcing frequency

3.1.2 Forcing frequencies 0.88 Hz, 0.90 Hz, 0.94 Hz

Near the frequency that gives the maximum amplitude at $f_y = 0.98$ Hz (points NR1, NR2, NR3), the amplitude of the wave increases and some significant irregularities start to show in the time histories. Figure 3.7 exhibits the time history when $f_y = 0.94$Hz and $\kappa_y = 0.0177$, associated to video captures in Figure 3.6. The maximum

amplitude ζ_{max} for each of the those proposed forcing frequency ratio is increasing. It can be seen that the slope in the evolution of the free-surface amplitude is more steep than the $f_y = 0.78$Hz test series, and a nonlinear first sloshing mode is experienced on the free surface, as can be seen in Figure 3.6.

Figure 3.6: Video captures of the model's pool from the $f = 0.94$ Hz and $a_y = 5$ mm test series but performed in the x-direction to see modal forms: semi-linear first sloshing mode is outlined.

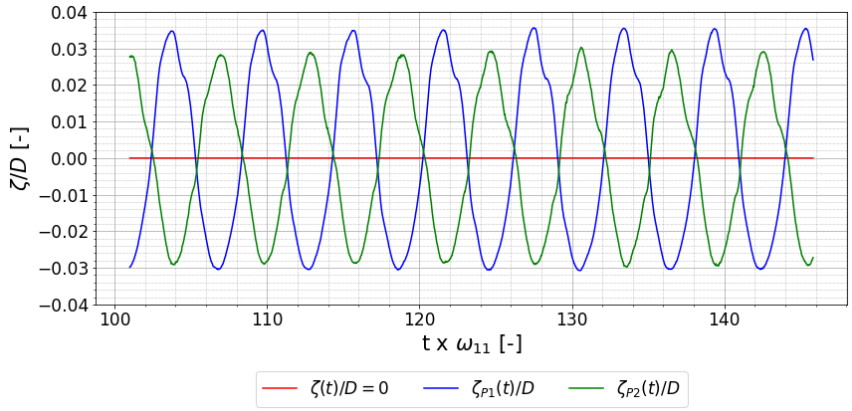

Figure 3.7: Dimensionless time histories for the horizontal harmonic base excitation $a_y = 5$ mm, $f_y/f_1 = 0.959$ and $f_y = 0.94$ Hz; P1 time evolution shows up peaks and secondary peaks due to nonlinear sloshing phenomenon.

The PSD plots in Figure 3.8 show that also in this case the primary peaks are at the forcing frequency ratio, but there's a hint of nonlinear component attached to the primary peak, which is instead representative of the external harmonic load. The resolution is too low (frequency step ≈ 0.02) to catch exactly the value of the nonlinear component, which in f_y[0.94,0.98] Hz.
The trend observed in the time history signal is shown in the phase plane plots, in Figure 3.9, showing skewed elliptical orbits. The wave-structure interaction is experienced even for a small forcing amplitude, because of the not circular and not even elliptical orbits' shape. The phase plane plot for P1 indicates that as the forcing

frequencies increase, then $\zeta(t)$ increases within the positive quarter delineated by $\zeta(t)/D = [0.00, 0.04]$ on the x-axis and $\zeta(t+\tau)/D = [0.00, 0.04]$ on the y-axis.

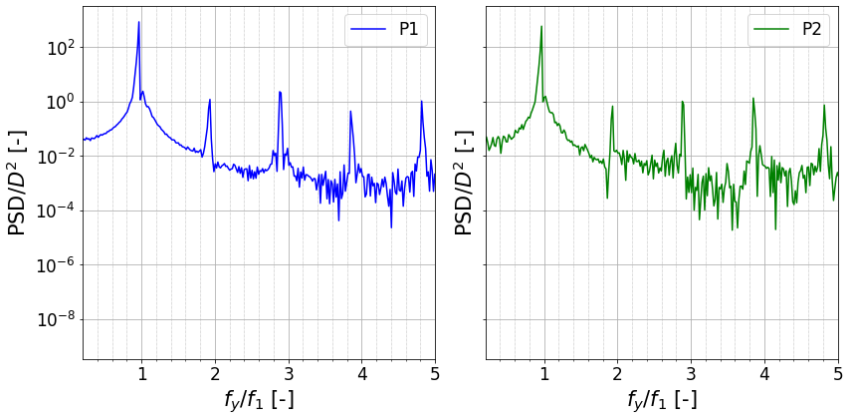

Figure 3.8: Power Spectral Density for the horizontal harmonic base excitation $a_y = 5$ mm, $f_y/f_1 = 0.959$ and $f_y = 0.94$ Hz; while the x-axis are until $f_y/f_1 = 5$; peaks at the forcing amplitude multiples and at $f = 1$ Hz, but low resolution affects the plots

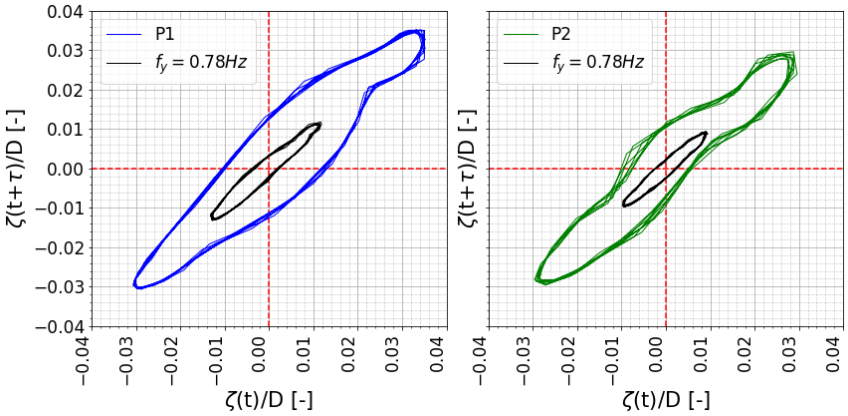

Figure 3.9: Dimensionless phase plane plots for the horizontal harmonic base excitation $a_y = 5$ mm, $f_y/f_1 = 0.959$ and $f_y = 0.94$ Hz; P1 phase plane plot is greater than the one for P2 and shows up higher nonlinearity in the positive quarter; a confrontation is made with the phase plane plots for $f = 0.78$ Hz and $a_y = 5$ mm

3.1.3 Forcing frequency 0.98Hz

The forcing frequency $f_y = 0.98$ Hz (in point R) is when there is the maximum free-liquid surface wave amplitude. Dimensionless acceleration is equal to $\kappa_y = 0.0194$. For the same adopted methodology in the previous cases, video captures for the same test series but performed in the x-direction, in Figure 3.10, are useful to exhibits

nonlinear free-surface motion.
Time evolution of the free-liquid surface in Figure 3.11 shows up higher peaks than the troughs for P1 probe, while secondary peaks are experienced in the P2 time evolution. It's a sign of nonlinearity alongside a non-negligible wave-structure interaction. The maximum amplitude is higher 2.67 times the maximum one for the $f_y = 0.78$ Hz test series.

Figure 3.10: Video captures of the model's pool from the $f = 0.98$ Hz and $a_y = 5$ mm test series but performed in the x-direction to see modal forms: nonlinear sloshing mode is outlined, which is similar to the first mode.

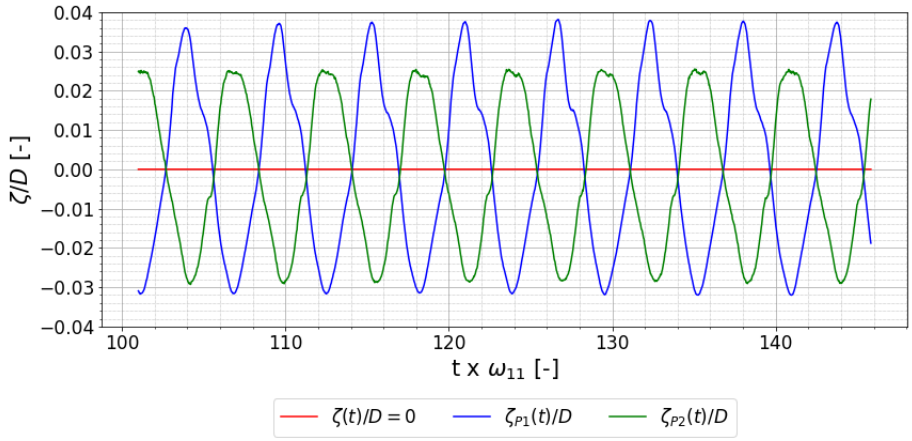

Figure 3.11: Dimensionless time histories for the horizontal harmonic base excitation $a_y = 5$ mm, $f_y/f_1 = 1.000$ and $f_y = 0.98$ Hz; slopes of the curves are greater than the lower frequency cases and they increase approaching the peaks of the time evolution for P1.

The wave-structure interaction is the reason way the orbits in phase plane in Figure 3.13 has a so strong skewness in correspondence of the peaks, and are not even elliptical. The PSD plots for the regime signal in Figure 3.12 still indicates the forcing frequency as the major contribution to the motion. The low resolution doesn't allow being sure about the real value of a nonlinear frequency component, which is in range

f =[0.91,0.98] Hz. This could be the first natural sloshing frequency, that from the numerical studies is about to be $f_1 = 0.90$ Hz.

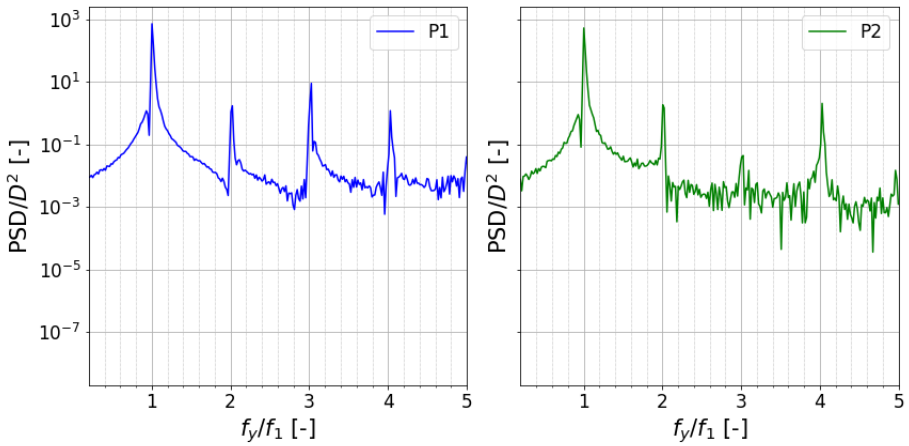

Figure 3.12: Power Spectral Density for the horizontal harmonic base excitation $a_y = 5$ mm, $f_y/f_1 = 1.000$ and $f_y = 0.98$ Hz; low resolution affects the PSD, but a nonlinear component can be spotted before the forcing frequency peak.

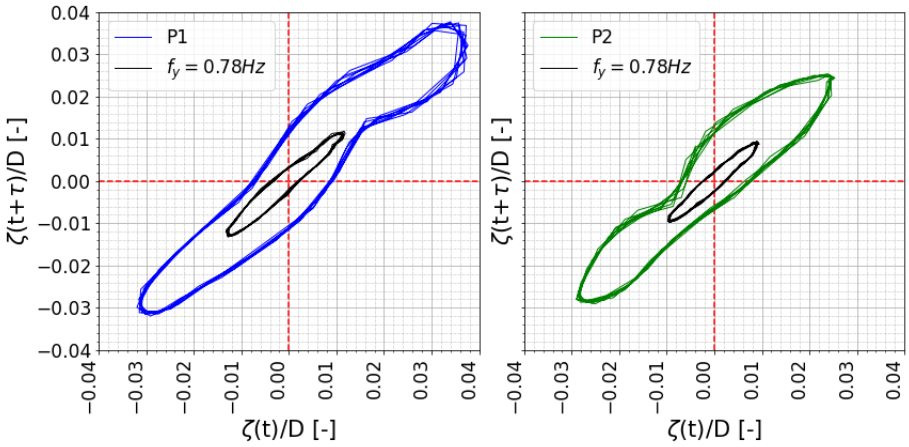

Figure 3.13: Dimensionless phase plane plots for the horizontal harmonic base excitation $a_y = 5$ mm, $f_y/f_1 = 1.000$ and $f_y = 0.98$ Hz P1 phase plane plot is greater than the one for P2 and shows up higher nonlinearity in the positive quarter; a confrontation is made with the phase plane plots for $f = 0.78$ Hz and $a_y = 5$ mm and the difference is up to 2.67 time the maximum amplitude within the two series.

3.1.4 Forcing frequency 1.04 Hz

The test series at frequency ratio $f_y/f_1 = 1.061$ at $f_y = 1.04$ Hz ($\kappa_y = 0.0219$), (point AR2) away from the greater amplitude is lastly studied. Time history in Figure 3.15 indicates that the wave amplitude $\zeta(t)$ for P1 is lower than the previous case for $f_y = 0.98$ Hz, while $\zeta(t)$ for P2 is comparable with P1 for the first time in basic reference test series. Phase plane plots in Figure 3.16 don't show chaotic motion but still strong skewness, in particular from P2. It seems that wave structure interaction is stronger for the P2 signal close to the inner cylinder.

Figure 3.14: Video captures of the model's pool from the $f = 0.98$ Hz and $a_y = 5$ mm test series, but performed in the x-direction to see modal forms: nonlinear sloshing mode is outlined.

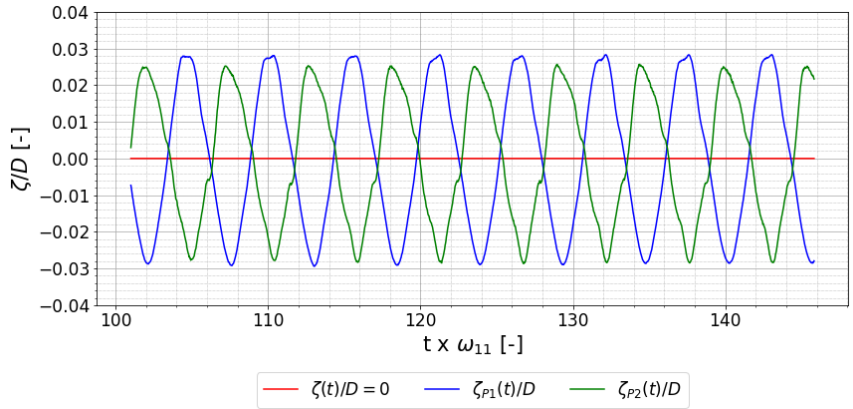

Figure 3.15: Dimensionless time histories for the horizontal harmonic base excitation $a_y = 5$ mm, $f_y/f_1 = 1.061$ and $f_y = 1.04$ Hz; P1 peaks are not greater than the ones for P2 as in the previous forcing frequencies.

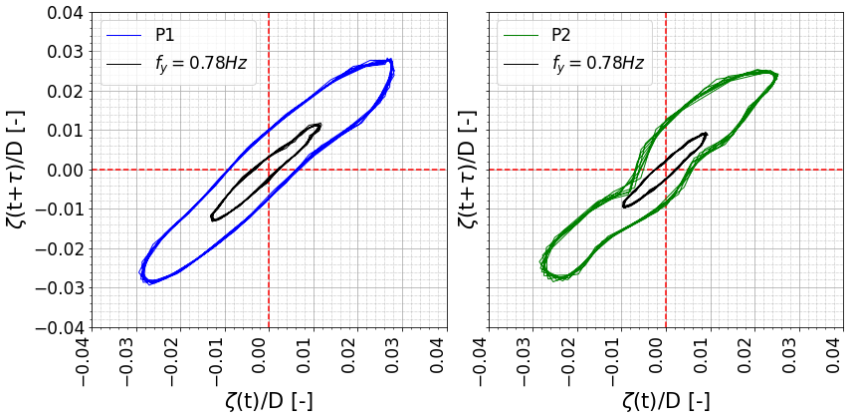

Figure 3.16: Dimensionless phase plane plots for the horizontal harmonic base excitation $a_y = 5$ mm, $f_y/f_1 = 1.061$ and $f_y = 1.04$ Hz; phase plane plots for the first forcing frequency $f_y = 0.78$ Hz is smaller than the one for $f_y = 1.04$ Hz.

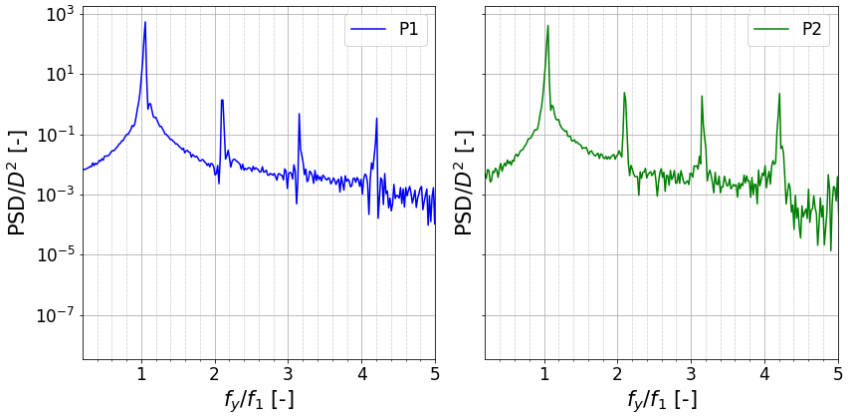

Figure 3.17: Power Spectral Density for the horizontal harmonic base excitation $a_y = 5$ mm, $f_y/f_1 = 1.061$ and $f_y = 1.04$ Hz; low resolution affects the PSD, but a nonlinear component can be spotted after the forcing frequency at $f = 1.11$ Hz

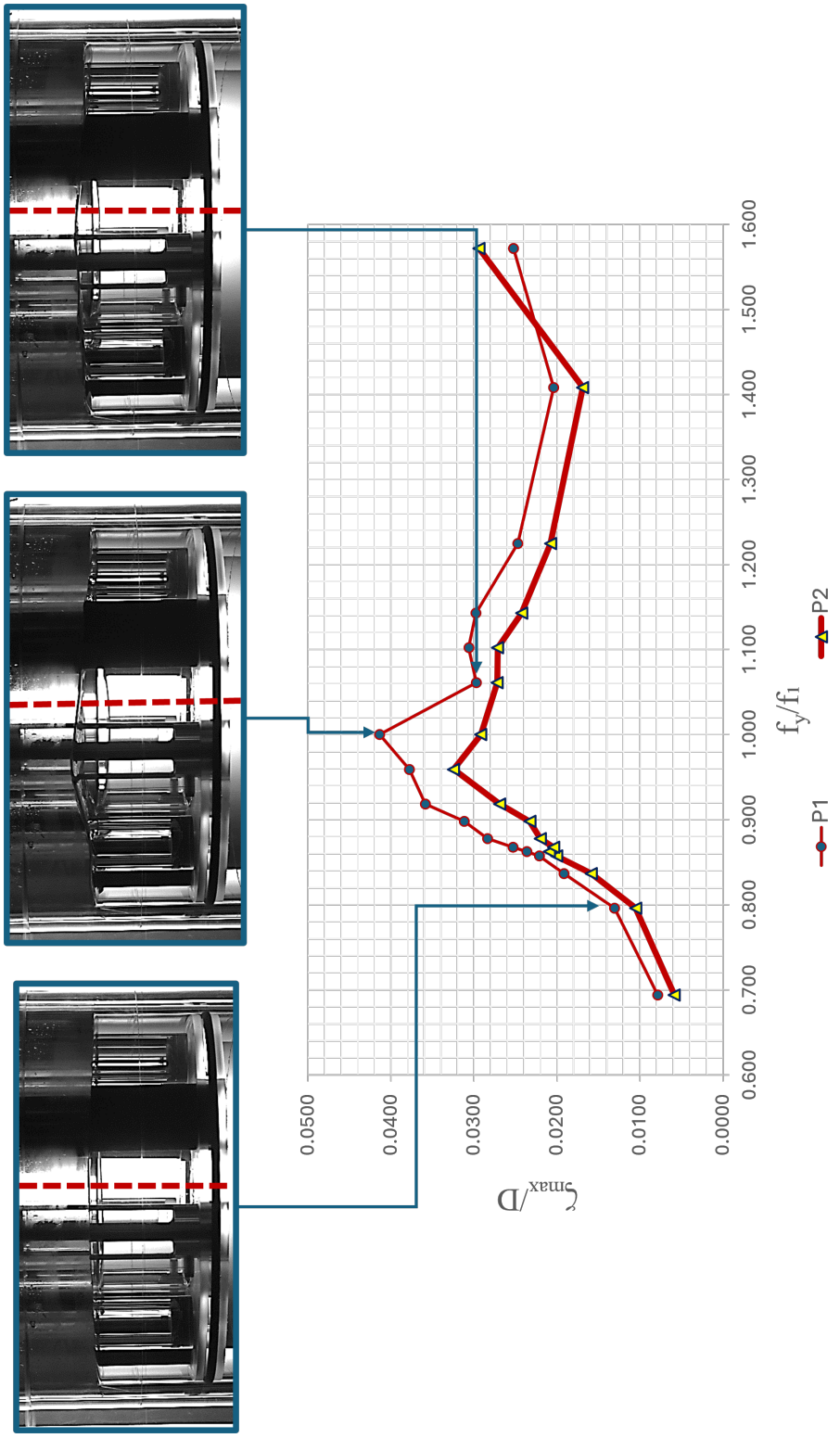

Figure 3.18: Evolution of maximum wave amplitude in the pool's model from the video captures; the comparison is associated to the maximum amplitude plot for horizontal harmonic base excitation in Y direction in function of the frequency ratio f_y/f_1 when $a_y = 5$ mm ($a_y/D = 0.013$).

3.2 Effect of forcing amplitude

The first comparison is about the forcing amplitude for the horizontal harmonic base excitation in one DoF. In addition to reference test series for a maximum forcing amplitude equal to $a_y = 5$ mm, $a_y = 15$ mm and $a_y = 30$ mm are considered (§2.7.1). The water height is still the nominal one equal to $h = 8.84$ cm. The analysis method used to pursue this investigation is the same used for the reference test series (§3.1). For a proper comparison with the test series at forcing amplitude $a_y = 5$ mm, $f_1 = 0.98$ Hz has been selected as reference for the dimensionless frequency ratio. The selected forcing frequency is when the reference test series experiences the greater wave amplitude.
Five investigation points have been selected to investigate the effect of the forcing amplitude on the free-liquid surface motion during the sloshing process: point **A** at $f_y/f_1 = 0.796$ ($f_y = 0.78$ Hz); point **B** at $f_y/f_1 = 0.898$ ($f_y = 0.88$ Hz); point **C** at $f_y/f_1 = 1.000$ ($f_y = 0.98$ Hz); point **D** at $f_y/f_1 = 1.408$ ($f_y = 1.38$ Hz).
Table 3.1 presents the dimensionless forcing acceleration κ_y that varies with different forcing amplitude. Dimensionless acceleration is a good indicator for finding patterns in the effect of the forcing amplitudes comparison.

f_y[Hz]	0.78	0.88	0.98	1.38
κ_y for $a_y = 5$ mm	0.0122	0.0156	0.0193	0.0383
κ_y for $a_y = 15$ mm	0.0367	0.0467	0.0580	0.0115
κ_y for $a_y = 30$ mm	0.0735	0.0935	0.1159	0.2299

Table 3.1: κ_y dimensionless acceleration for the horizontal harmonic base excitation in one DoF for different forcing amplitude a_y

The harmonic test series at $a_y = 5$ mm presents the maximum wave amplitude for P1 capacitance probe when $f_y = 0.98$ Hz. Since the horizontal harmonic base excitation in y direction have the forcing frequencies around the first natural mode, P1 capture the most valuable information about the wave amplitude. Figure 3.19 presents the complete plot for maximum wave amplitude as a function of the frequency ratio, both for P1 than P2. Taking into account the information about P1, a plateau of the maximum amplitude can be seen for $a_y = 15$ mm in correspondence to a forcing frequency range equal to f_y =[0.98,1.08] Hz, while for $a_y = 30$ mm for f_y =[0.98,1.12] Hz. This behavior is not observed for the reference test series $a_y = 5$ mm, which reaches the maximum wave amplitude only at $f_y = 0.98$ Hz.
In the same plot, wave amplitude for P2 is shown. It is always minor than the one detected from P1, but this trend is inverted at higher frequency ratio. A possible explanation could be the starting of a swirling motion of the free-liquid surface. A deeper look at this behavior is provided in the investigation of the investigation point E at $f_y = 1.38$ Hz.

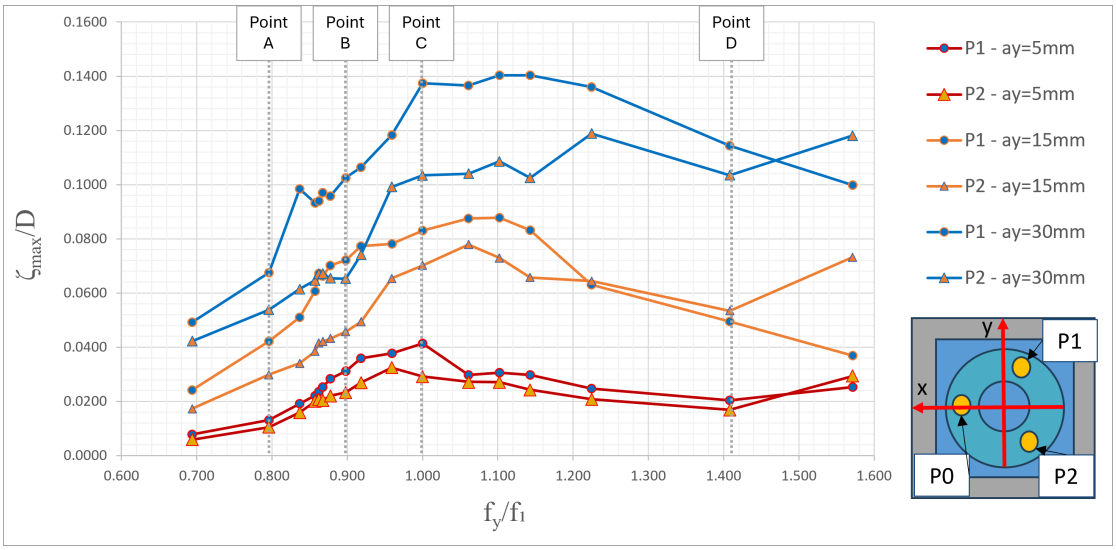

Figure 3.19: Maximum amplitude plot for horizontal harmonic base excitation in Y direction in function of the frequency ratio f_y/f_1 when $a_y = 5, 15, 30$ mm $(a_y/D = 0.013, 0.038, 0.076)$; investigation point are outlined.

3.2.1 Forcing frequency 0.78 Hz

The first investigation point A is at $f_y/f_1 = 0.796$ for $f_y = 0.78$ Hz. Video captures of the free-liquid surface approaching and reaching the maximum amplitude are presented in Figure 3.20 for the $a_y = 30$ mm test series. Motion is strongly nonlinear and some bubbles start to show up already for a low forcing frequency. Maximum amplitude is reached when a wave coming from the right edge merges with another one from the left edge. The merge takes place not in the center line of the model because the internal structure damping.

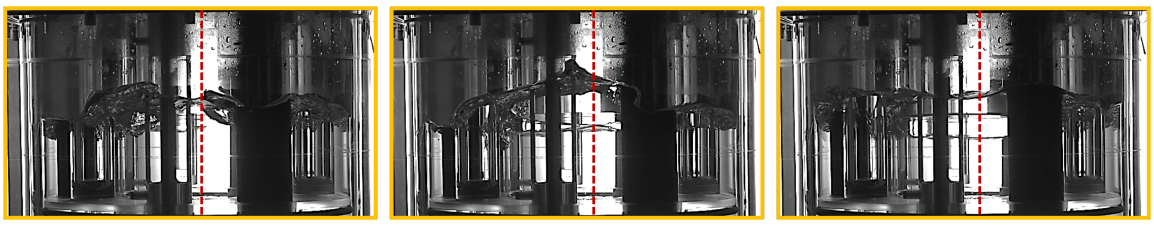

Figure 3.20: Cine file capture near, at and beyond the maximum amplitude when $f = 0.78$ Hz: the maximum amplitude is reached in proximity of the P1 sensor after a merge within two waves from the right edge and the left edge; centreline of the tank is outlined in red.

Phase plane plots in Figure 3.21 for showing immediately that the amplitude $\zeta(t)$ is increasing when the forcing amplitude increase. The orbits for each of the studied cases are different, highlighting different wave-structure interaction. Nonlinearity

is stronger as the dimensionless acceleration κ_y is increasing for increasing forcing amplitude.

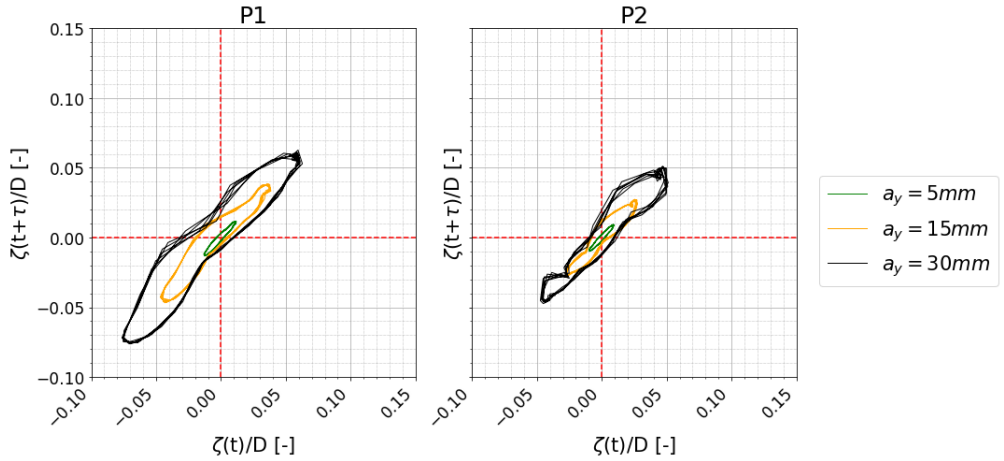

Figure 3.21: Phase plane plots for $a_y = 5, 15, 30$ mm, $f_y/f_1 = 0.796$ at $f_y = 0.78$ Hz: skewness makes assuming different orbits due to different wave structure interaction.

The corresponding PSD plots in Figure 3.22 gives back a hint on the nonlinear frequency associated to the motion. Frequency x-axis have been cut up to 5 Hz because the predominant motion is still periodic each 15 or 20 seconds, so the most energetic peaks are about the forcing frequency. Despite the low resolution in the PSD plots doesn't allow being sure about the value of the secondary peak indicated, an estimation can be done and is about $f = 0.74$ Hz, at the left of $f_y = 0.78$ Hz peak of the external excitation.

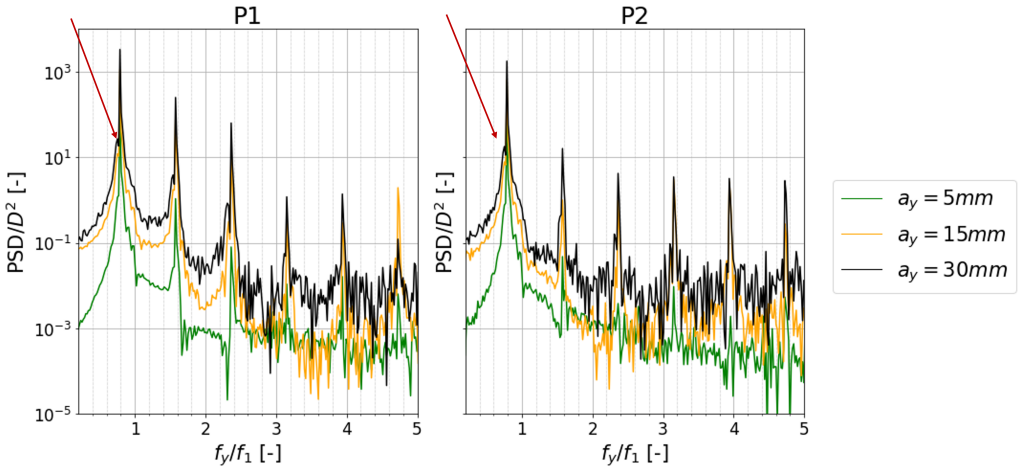

Figure 3.22: Power Spectral Density for the horizontal harmonic base excitation for $a_y = 5, 15, 30$ mm, $f_y/f_1 = 0.796$ at $f_y = 0.78$ Hz: a possible nonlinear component is outlined at $f = 0.74$ Hz for the $a_y = 30$ mm test series.

3.2.2 Forcing frequency 0.88 Hz

The second investigation point B is taken fo $f_y/f_1 = 0.898$ at $f_y = 0.88$ Hz as an example of approaching to the maximum wave amplitude. Figure 3.23 presents the video capture near/at the maximum wave amplitude. The complex geometry, the inner cylinder and the damping internal element are responsible for this behavior highly nonlinear behavior of the free-liquid surface.

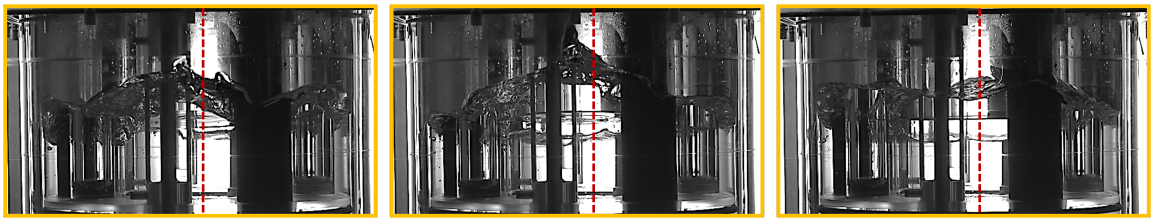

Figure 3.23: Cine file capture near, at and beyond the maximum amplitude when $f = 0.88$ Hz: highly nonlinear modes are occurring in the model's pool.

Figure 3.24 shows increasing amplitude $\zeta(t)$. If the maximum amplitude reached is compared in taking as reference the $a_y = 5$ mm test series, ζ_{max} of P1 for 15 mm series is 2.31 times and 3.29 time for 30 mm series. Wave structure interaction is particular strong at the troughs for the medium and the larger forcing amplitude test series: phase plane presents a small lobe in the negative quarter for negative $\zeta(t)/D$ and negative $\zeta(t+\tau)/D$.
The PSD in Figure 3.25 presents a secondary peak at $f = 0.85$ Hz despite the more energetic ones are about the forcing frequency $f_y = 0.88$ Hz. Despite the resolution, this peak can be outlined in particular in the $a_y = 5$ mm test series, while in the other two the low resolution affects too much the plots.

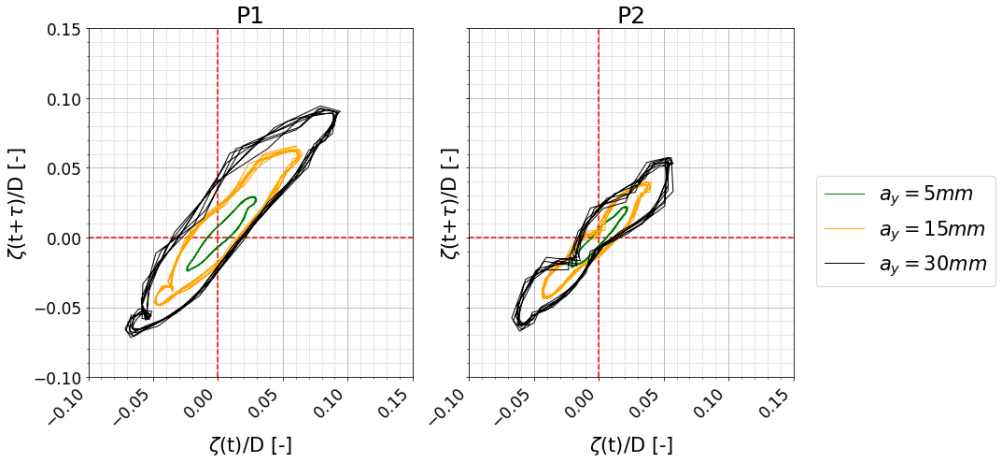

Figure 3.24: Phase plane plots for $a_y = 5, 15, 30$ mm, $f_y/f_1 = 0.898$ at $f_y = 0.88$ Hz: skewness makes assuming similar orbit for the troughs of the medium and the larger forcing amplitude series.

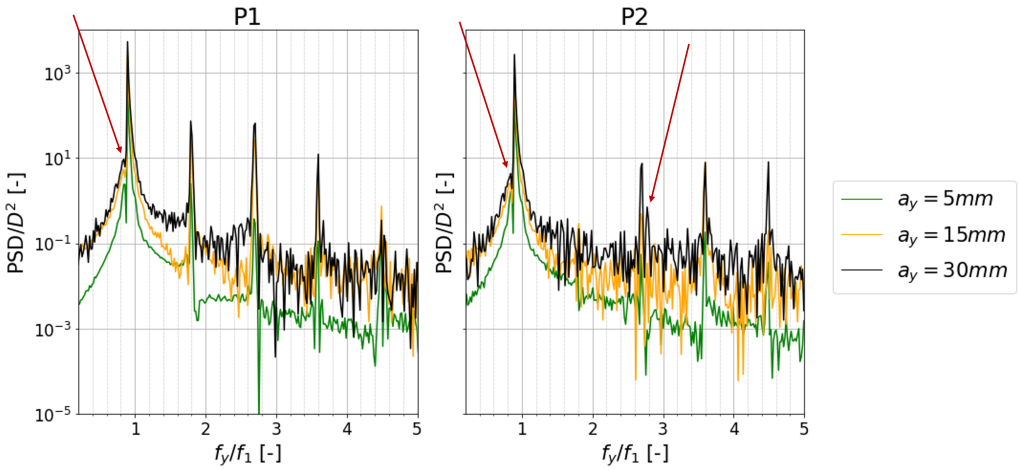

Figure 3.25: Power Spectral Density for the horizontal harmonic base excitation for $a_y = 5, 15, 30$ mm, $f_y/f_1 = 0.898$ at $f_y = 0.88$ Hz: a possible nonlinear component is outlined at $f = 0.85$ Hz for the $a_y = 30$ mm test series.

3.2.3 Forcing frequency 0.98 Hz

The third investigation point C for $_y/f_1 = 1.000$ at $f_y = 0.98$ Hz. From §3.1 this forcing frequency is the one that excites more the free-liquid surface motion for the $a_y = 5$ mm test series in terms of maximum amplitude detected from the P1 capacitance probe. This forcing frequency is the first of a range that goes until $f_y = 1.08$ Hz for the medium forcing amplitude series and $f_y = 1.12$ Hz for the greater forcing amplitude series. comparing with the $a_y = 5$ mm test series, maximum wave amplitude for the $a_y = 15$ mm series is 2.01 times higher and 3.32 times for the $a_y = 30$ mm series.
The video captures in Figure 3.26 near/at the maximum wave amplitude leads to a similar conclusion from the smaller forcing frequency: the greater amplitude measured from P1 is after the merge of two waves from the right and the left edge of the ALFRED's model. The violence increases for higher forcing frequencies, so at higher κ_y value in terms of dimensionless external acceleration.

Figure 3.26: Cine file capture near, at and beyond the maximum amplitude when $f = 0.98$ Hz: the maximum amplitude is reached in proximity of the P1 sensor after a merge within two waves from the right edge and the left edge; the violence of the motion is increasing.

Phase plane plots in Figure 3.27 present orbits more asymmetric than the previous investigation points at lower forcing frequency. Nonlinearity is higher for the test series at higher dimensionless acceleration parameter κ_y (Table 3.1). As an example, a selected time history is presented for the higher forcing amplitude at $f_y = 0.98$ Hz in Figure 3.28: periodicity cannot be emphasized as in the reference test series (§3.1, and peaks for P1 reach different amplitudes in the time evolution as well the ones for P2.

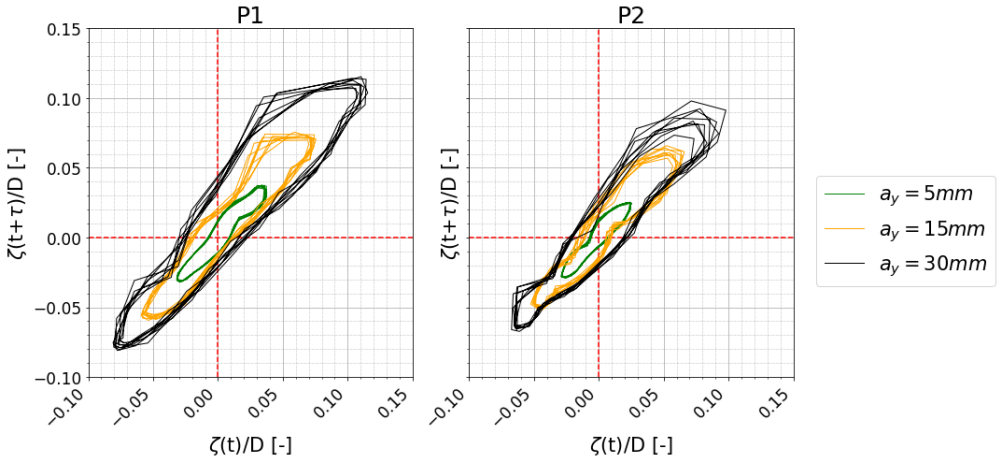

Figure 3.27: Phase plane plots for the horizontal harmonic base excitation for $a_y = 5, 15, 30$ mm, $f_y/f_1 = 1.000$ at $f_y = 0.98$ Hz: phase plane plots make asymmetric but out of focus orbits.

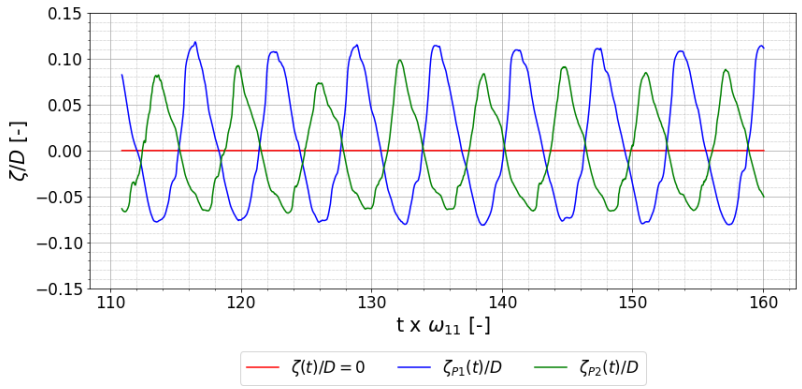

Figure 3.28: Dimensionless time histories for the horizontal harmonic base excitation $a_y = 30$ mm, $f_y/f_1 = 1.000$ and $f_y = 0.98$ Hz; P1 peaks and troughs reach different amplitudes in the time evolution, as well as P2 peaks and troughs.

The PSD plots are affected by low resolution, so the nonlinear component cannot be clearly identified, but studying the $a_y = 5$ mm curve a secondary peak is at $f = 0.91$ Hz, while the primary one is at the forcing frequency $f_y = 0.98$ Hz.

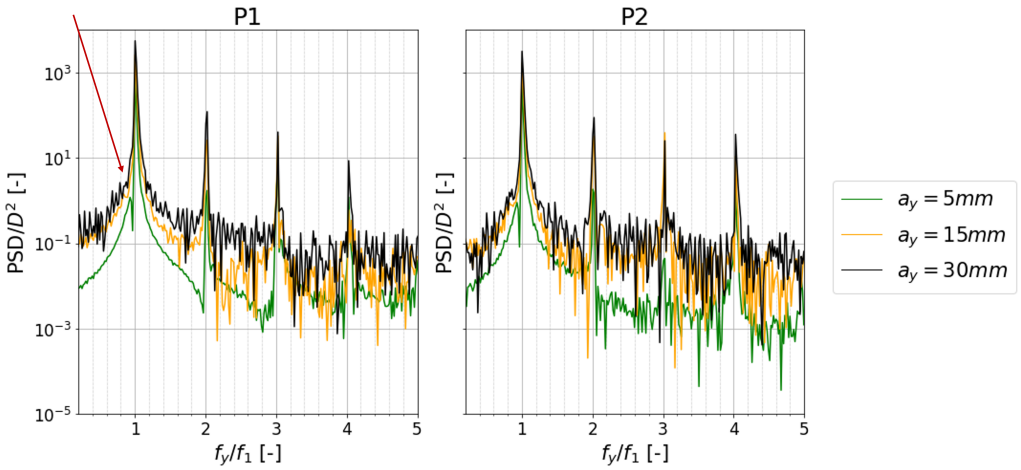

Figure 3.29: Power Spectral Density for the horizontal harmonic base excitation for $a_y = 5, 15, 30$ mm, $f_y/f_1 = 1.000$ at $f_y = 0.98$ Hz; a possible nonlinear component is outlined at $f = 0.91$ Hz for the $a_y = 5$ mm test series.

3.2.4 Forcing frequency 1.38 Hz

The investigation point D for $f_y/f_1 = 1.408$ at $f_y = 1.38$ Hz is here discussed. The first observation is about the wave amplitude of P1 related to the one of P2: the second probe, which is near the inner cylinder of ALFRED's model, captures higher values than the one on the edge of the annular tank. It's the first time that this magnitude of amplitude is reached in the test series at different forcing amplitude. The video captures in Figure 3.30 for $a_y = 30$ mm show a violent motion that leads to bubble making events both at the surface and under it. A very complex motion is undergoing in the model pool, which is also not resembling so easily to the first sloshing mode.

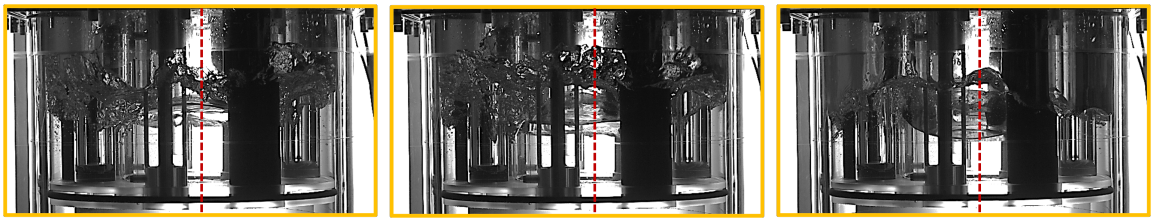

Figure 3.30: Cine file capture near, at and beyond the maximum amplitude when $f = 1.38$ Hz: the maximum amplitude is not more reached in proximity of the P1 sensor and the violence of the motion is increasing by bubbles making events.

The phase plane plots in Figure 3.31 show violent motion for the larger forcing amplitude because at equal resolution [$\tau = 0.05$ s] the curves are not smooth. This observation is in continuity with the investigated $f_y = 0.98$ Hz forcing frequency in the previous paragraph. P2 contribution becomes greater than the one of P1, so

phase plane shows up the strong wave structure interaction with the inner cylinder. The PSD plots are still affects of low resolution and basically show the forcing frequency contribution and its multiples. Despite the difficulties, smaller peaks can be spotted before and after the $2 \cdot f_y$ peak in the P2's PSD, that becomes more representative since the magnitude of wave amplitude is higher than the P1 one.

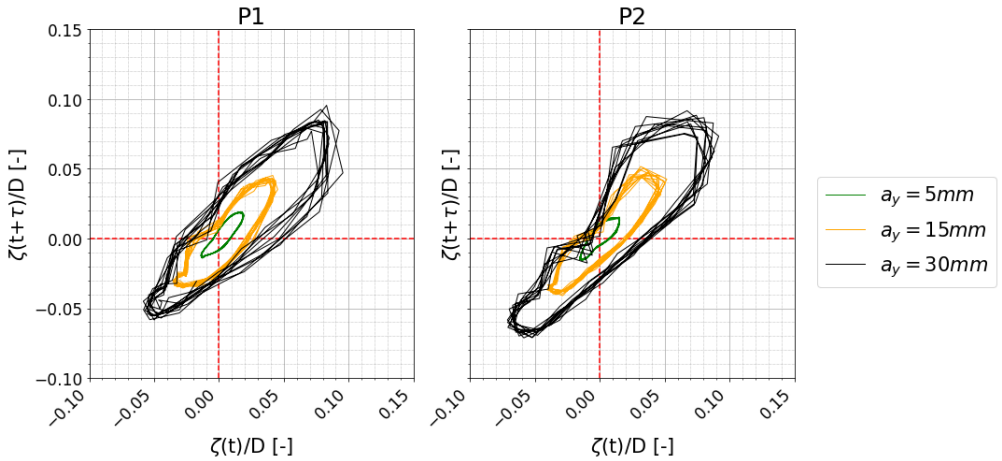

Figure 3.31: Phase plane plots for the horizontal harmonic base excitation for $a_y = 5, 15, 30$ mm, $f_y/f_1 = 1.408$ at $f_y = 1.38$ Hz: phase plane plots show not smooth orbits due to violent free-liquid surface motion.

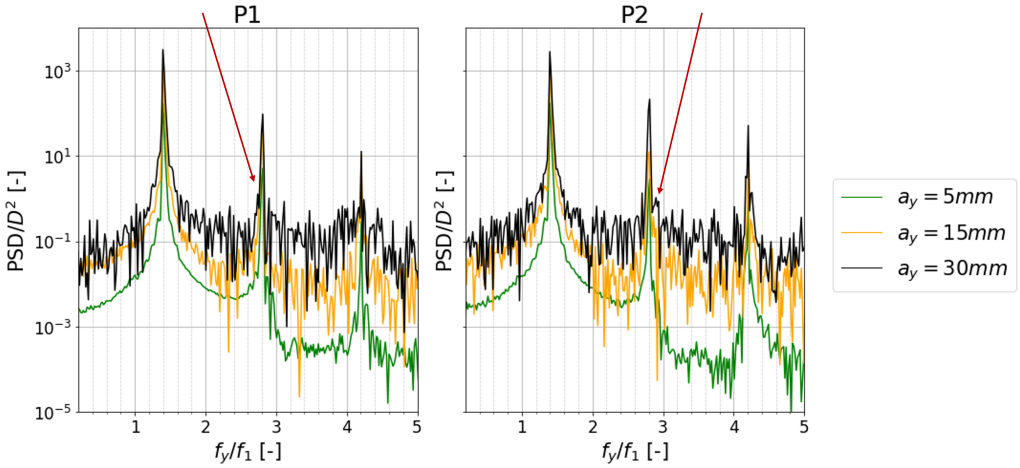

Figure 3.32: Power Spectral Density for the horizontal harmonic base excitation for $a_y = 5, 15, 30$ mm, $f_y/f_1 = 1.408$ at $f_y = 1.38$ Hz: smaller peaks can be spotted before and after the $2 \cdot f_y$ peak in the P2's PSD.

3.3 Effect of water depth

The influence of water depth on ALFRED's model is investigated across five different depths. Particularly, the study focuses on shallow water due to the compact dimensions of the model. The water depth is measured starting from the diaphragm as a convention, because the main sloshing processes take places in the upper part of the model's pool.
The reference test series involves horizontal harmonic base excitation in one degree of freedom (DoF), with a force amplitude set to $a_y = 15$ mm and the model's free-liquid surface resting at a level of $h_{model} = 8.84$ cm. To explore the effect, variations of $\pm 11\%$ are applied to h_{model}, along with two other initial conditions smaller than the nominal value. These tests are identified by the following nomenclature: $h_1 = 5.00$ cm, $h_2 = 6.50$ cm, $h_3 = 7.84$ cm, $h_{model} = h_4 = 8.84$ cm, and $h_5 = 9.90$ cm.
Table 3.2 summarizes the forcing frequencies corresponding to the maximum wave amplitudes at each tested water depth. Notably, the frequency required for achieving maximum amplitude increases with greater water depths, indicating a stiffening behavior of the free-liquid surface. Additionally, with increasing h, there is a considerable rise in maximum wave amplitude. For instance, an $+11\%$ increase in water depth from $h_{model} = 8.84$ cm results in a $+23\%$ increase in wave amplitude. Figure 3.33 visually illustrates this increasing amplitude, consolidating insights from Table 3.2.

	h_1	h_2	h_3	h_{model}	h_5
f_1[Hz]	0.85	0.98	0.98	1.04	1.08
$\%\zeta_{max,h-model}$	-43.1%	-20.3%	-6.6%	$\times$	$+23.0\%$

Table 3.2: Forcing frequencies and maximum wave amplitudes when $a_y = 15$ mm for the five water depths: $h_1 = 5.00$ cm, $h_2 = 6.50$ cm, $h_3 = 7.84$ cm, $h_4 = 8.84$ cm, $h_5 = 9.90$ cm.

Figure 3.34 shows the maximum amplitude reached for each test series. Video captures confirm the previous observation on the wave amplitude. It is visually confirmed that higher water depths, in addition to the small model dimensions, may lead to sloshing processes that could hit the top plate.
Time histories in Figure 3.35 are taken in a two/three periods of time windows. The different forcing frequencies for each water depth test series are there outlined, as the signal from the probes are not synchronized and the PSD in Figure 3.36 exhibits peaks in frequency ratio equal to 1, but the f_1 value is suited of each of the water depth. Phase plane plots in Figure 3.37 exhibit nonlinear behaviour for all the water depth, but as they increase, the free-liquid surface motion becomes more violent and critical. The violence of the motion is confirmed also in the previous Figure 3.34.

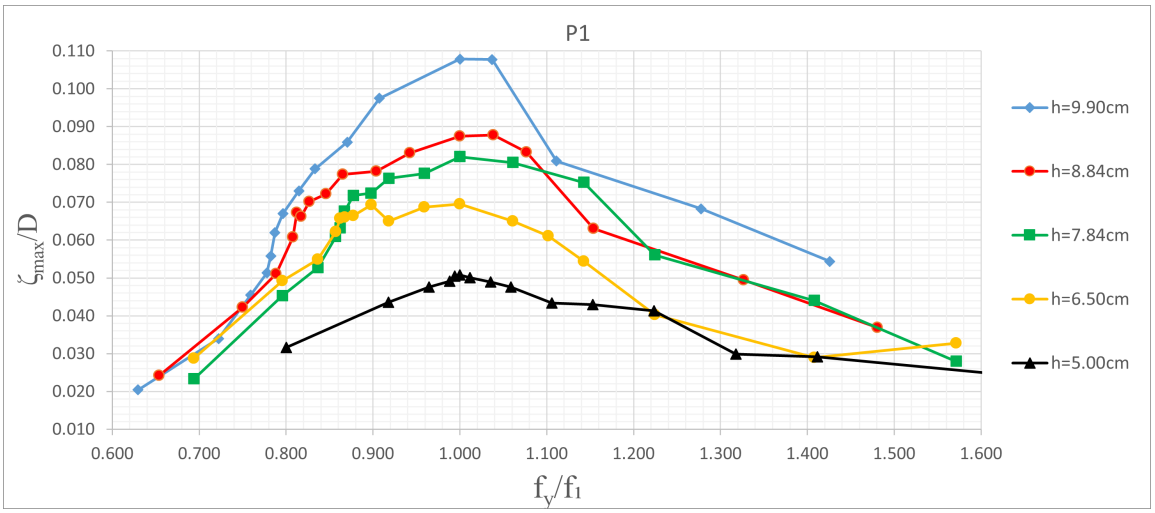

Figure 3.33: Maximum amplitude plot of P1 for horizontal harmonic base excitation in Y direction and forcing amplitude $a_y = 15$ mm in function of frequency ratio f_y/f_1; $f_1(h_1) = 0.85$ Hz, $f_1(h_2) = 0.98$ Hz, $f_1(h_3) = 0.98$ Hz, $f_1(h_4) = 1.04$ Hz, $f_1(h_5) = 1.08$ Hz; greater wave amplitude are reached for higher water depths.

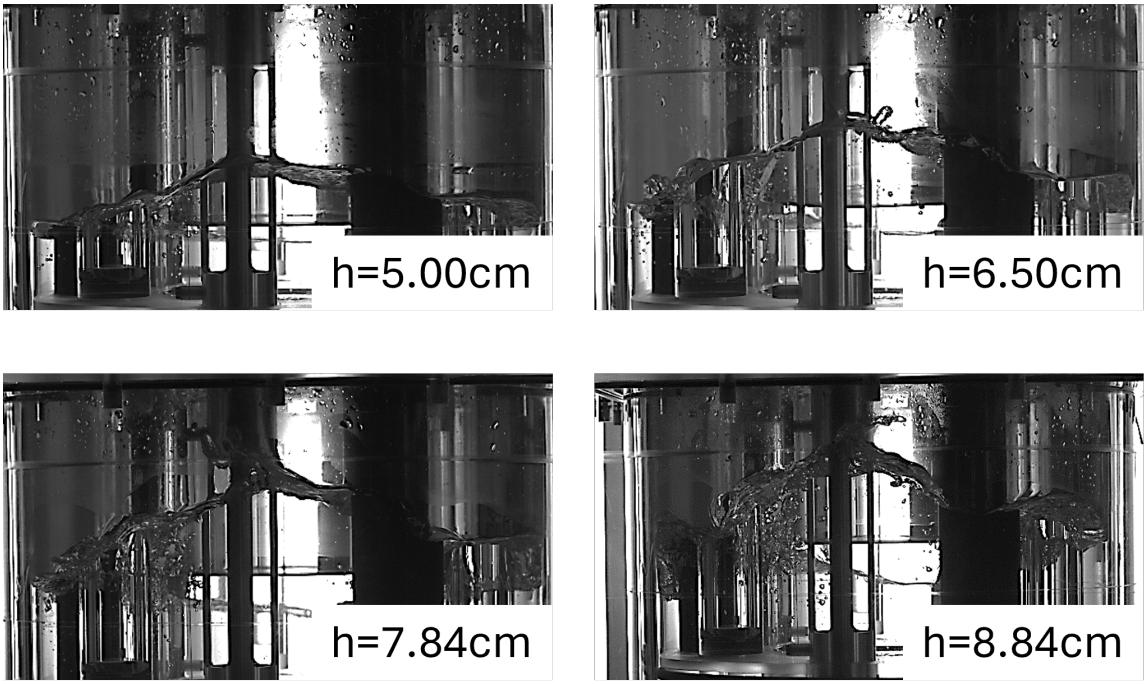

Figure 3.34: Video captures for the $a_y = 15$ mm test series at when the maximum amplitude is approached for h_1, h_2, h_3 and h_4: sloshing process reaches higher amplitude as the water depth increases; maximum amplitude are exhibited at increasing forcing frequencies.

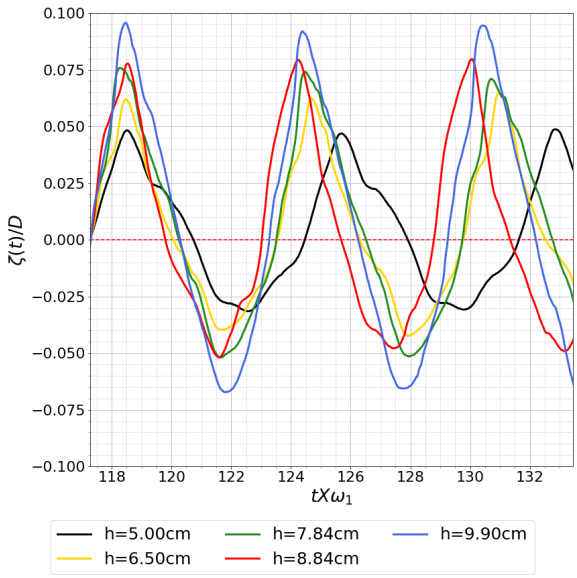

Figure 3.35: Dimensionless time histories (two periods window) at different water depth for the horizontal harmonic base excitation $a_y = 15$ mm when maximum amplitudes are reached at forcing frequency: $f_1(h_1) = 0.85$ Hz, $f_1(h_2) = 0.98$ Hz, $f_1(h_3) = 0.98$ Hz, $f_1(h_4) = 1.04$ Hz, $f_1(h_5) = 1.08$ Hz.

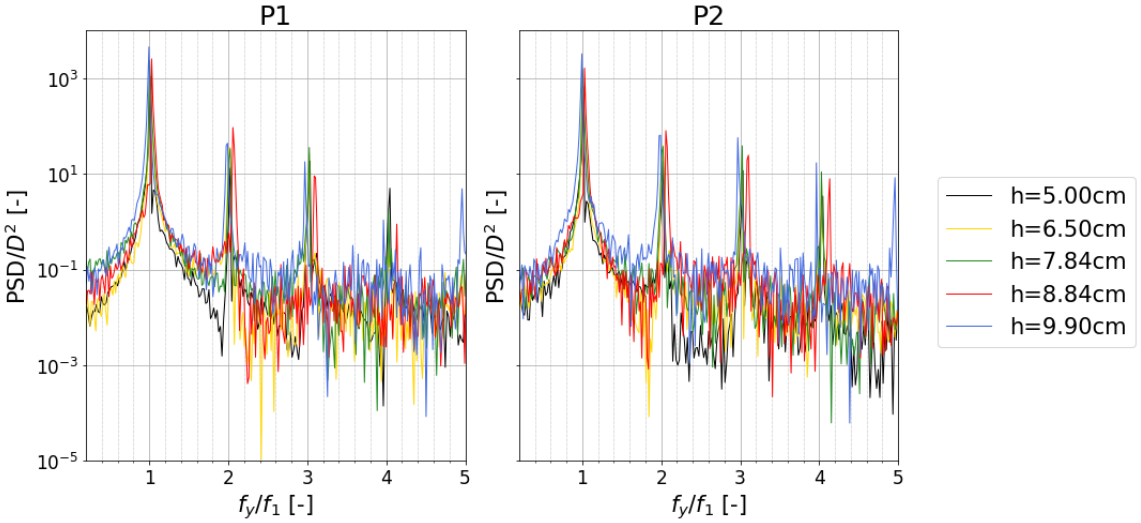

Figure 3.36: Dimensionless PSD plots at different water depth for the horizontal harmonic base excitation $a_y = 15$ mm when the forcing frequency is: $f_1(h_1) = 0.85$ Hz, $f_1(h_2) = 0.98$ Hz, $f_1(h_3) = 0.98$ Hz, $f_1(h_4) = 1.04$ Hz, $f_1(h_5) = 1.08$ Hz; forcing frequency peaks are in 1 because the f_1 is suited for each of the performed water depth.

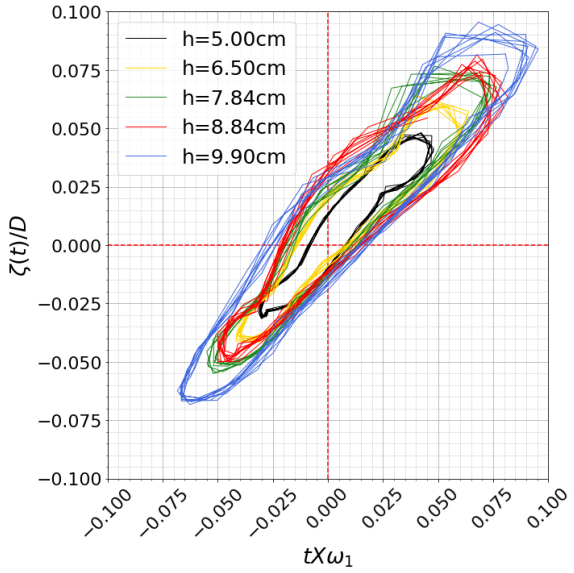

Figure 3.37: Dimensionless phase plane plots at different water depth for the horizontal harmonic base excitation $a_y = 15$ mm when the forcing frequency is: $f_1(h_1) = 0.85$ Hz, $f_1(h_2) = 0.98$ Hz, $f_1(h_3) = 0.98$ Hz, $f_1(h_4) = 1.04$ Hz, $f_1(h_5) = 1.08$ Hz.

3.4 Simulation of hazard in the primary pool

The simulation of a major hazard in the actual demonstrator is performed removing the 3 steam generators from the model, which are the most damping elements. Water depth of similitude $h_{model} = 8.84$ cm has been setup. The Figure 3.38 represents the maximum amplitude plots ζ_{max} for the test series at $a_y = 15$ mm and $a_y = 30$ mm in the two cases of internal structure with and without the 3 steam generators. In the plot the wave amplitude is reported as a function of the dimensionless acceleration κ_y. The shift of the larger amplitude test series is due to the definition of the parameter.
The first observation is about the wave amplitudes. In both the two forcing amplitude cases, at equal κ_y an higher maximum amplitude is reached from the liquid surface in the ALFRED's model. The damping role of the three steam generators is confirmed. Maximum amplitude is reached for similar forcing frequencies: for the $a_y = 15$ mm test series is for $f_y = 1.08$ Hz when the internal structure is complete and for $f_y = 1.12$ Hz when the hazard is simulated; for the $a_y = 30$ mm test series is for $f_y = 1.08$ Hz in both the internal configurations.
The second observation is about the frequency range when the maximum wave amplitude is reached. When the internal structure is complete of the three SG, a plateau at the maximum amplitude is reached for a range of forcing frequencies f_y =[0.98,1.12] Hz. On the contrary when the configuration without the three SG is set-up, the wave-structure interaction is still present but less significant and smaller plateau are recorded.

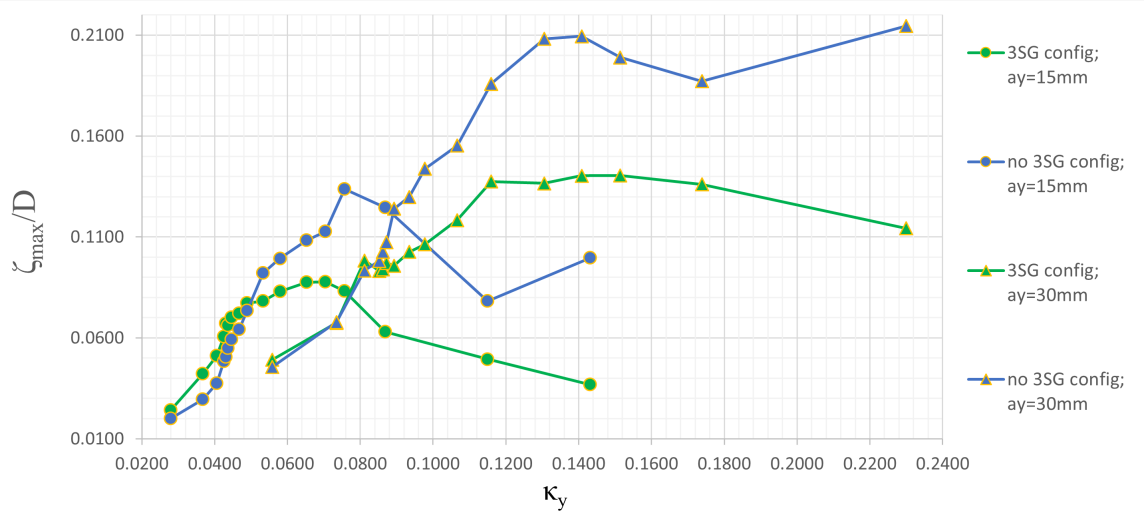

Figure 3.38: Maximum amplitude plot as a function of the dimensionless acceleration κ_y for the horizontal harmonic test series for the nominal configuration (3SG) and the hazardous one (no3SG): higher wave amplitudes are reached in the hazardous structural configuration at equal κ_y.

3.4.1 Forcing amplitude 15 mm at forcing frequency 1.12 Hz

The impact of the internal structural arrangement, both with and without the inclusion of three steam generators, is examined at a frequency of $f_y = 1.12$ Hz for the harmonic base excitation test series with an amplitude of $a_y = 15$ mm. The chosen frequency corresponds to the maximum wave amplitude during the hazardous configuration.
The video footage in Figure 3.39 captures moments before, during, and after reaching peak wave amplitude in both configurations of the model. The attained maximum amplitude significantly differs between the configurations, with the less-damped configuration reaching 1.61 times that of the normal configuration. Additionally, observations note the intensity of sloshing motion, with occurrences of bubble formation and vigorous free-liquid surface movements evident in the hazardous configuration.

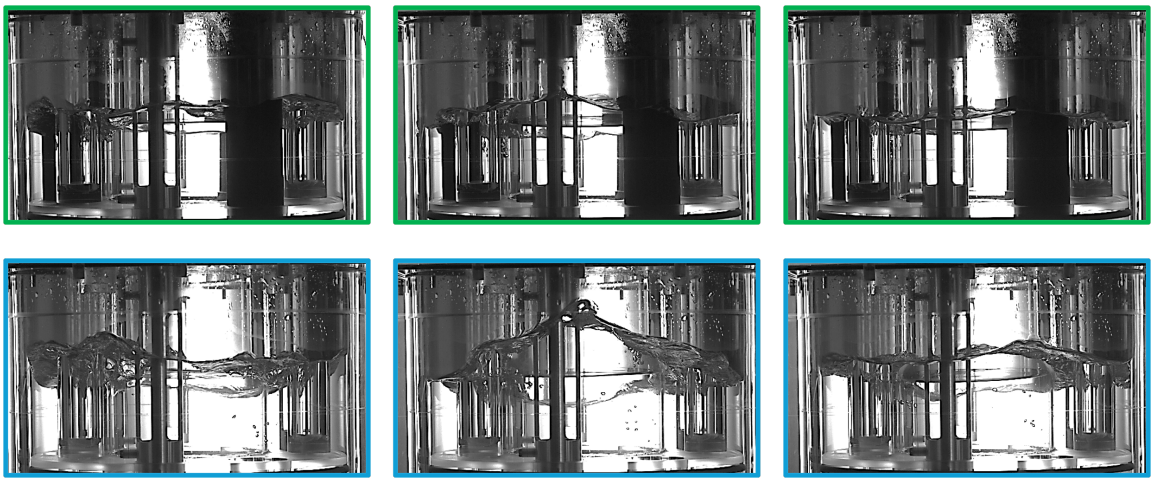

Figure 3.39: Video captures for the $a_y = 15$ mm test series at $f_y = 1.12$ Hz with the 3SG (first row) and without them (second row) when the maximum amplitude is approached, reached and passed: in the hazardous configuration higher wave amplitude are reached and the bubbles suggest a more violent sloshing process.

The time history shown in Figure 3.42 demonstrates higher peaks during the hazardous configuration setup. The interaction between waves and the structure appears more pronounced in the nominal configuration, as irregularities affect the trough, resulting in less smooth peaks compared to the other configuration. This phenomenon is also evident in the phase plane plots, where the orbits exhibit more prominences when the steam generators are installed. Although the PSD plots suffer from low resolution, a secondary peak at $f_y = 2.12$ Hz is discernible alongside the primary peak at $f_y = 0.98$ Hz and its multiples.

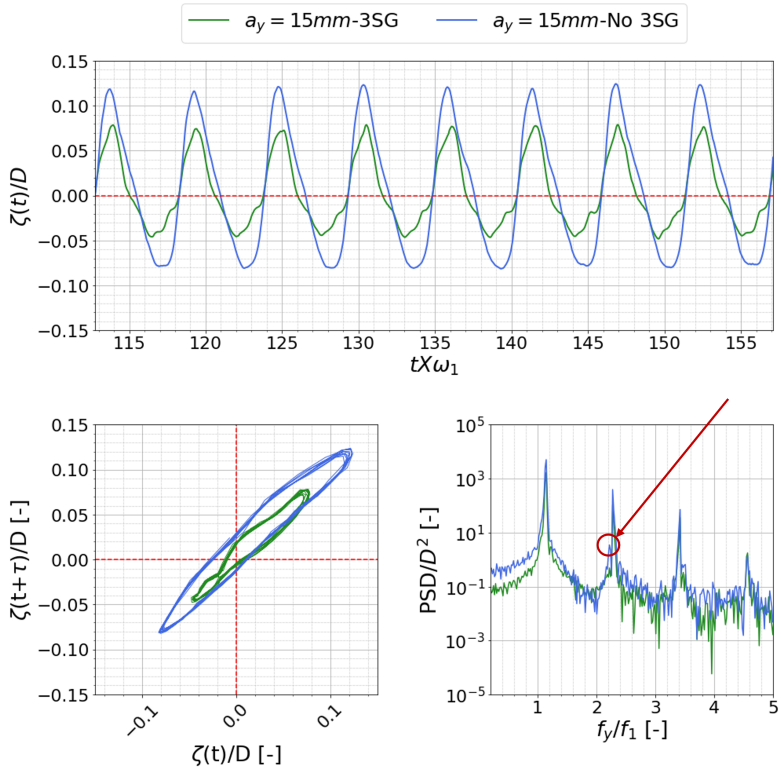

Figure 3.40: Dimensionless time history, phase plane plots and PSD plot for the $a_y = 15$ mm test series st $f_y = 1.12$ Hz for the two structural configuration: wave amplitude for the 3SG configuration is 1.61 times than for the other configuration; phase plane plots outline a stronger wave structure interaction in the nominal configuration; secondary peak at $f_y = 2.12$ Hz

3.4.2 Forcing amplitude 30 mm at forcing frequency 1.08 Hz

Test series at the greater forcing amplitude at $a_y = 30$ mm enhance the behavior outlined for the previous series at $a_y = 15$ mm. The maximum wave amplitude is reached at $f_y = 0.98$ Hz, where the free surface in the hazardous configuration reaches 1.50 times the one for the nominal internal structure of ALFRED. Violent motion is experienced for both of the set-up because bubbles making events can be equally seen. In §3.2 is outlined how applying 30mm of external forcing amplitude at $f_y = 0.98$ Hz is critical also for the ALFRED's complete internal structure.
The dimensionless time history confirms the differences in terms of maximum wave amplitude within the two examined structural configurations. Phase plane plots outline a stronger wave-structure interaction for the ALFRED's complete set-up. Unlike the $a_y = 15$ mm test series, the PSD exhibits a secondary peak at $f_y = 0.91$ Hz, despite the low resolution.

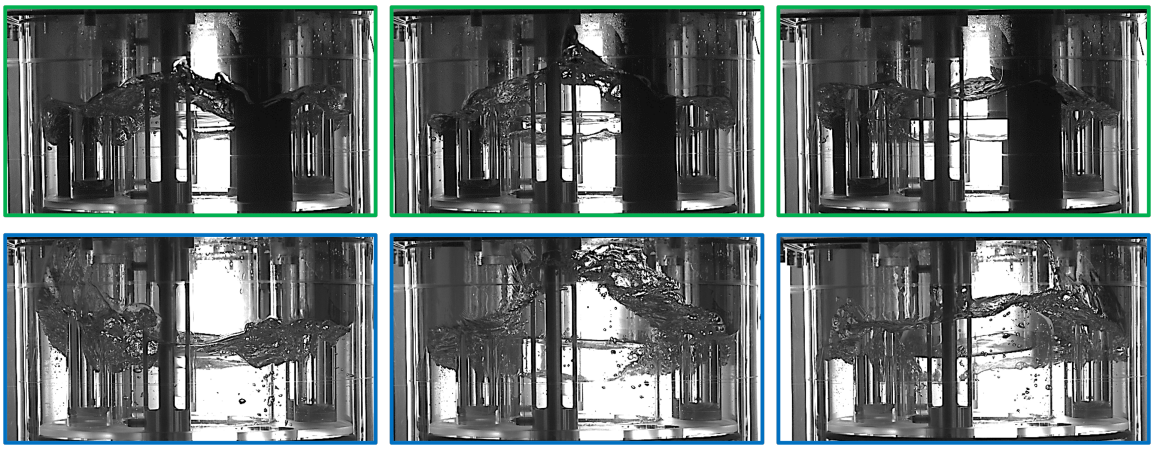

Figure 3.41: Video captures for the $a_y = 30$ mm test series at $f_y = 0.98$ Hz with the 3SG (first row) and without them (second row) when the maximum amplitude is approached, reached and passed: wave amplitude is higher for the hazardous configuration; the bubbles suggest a more violent sloshing process..

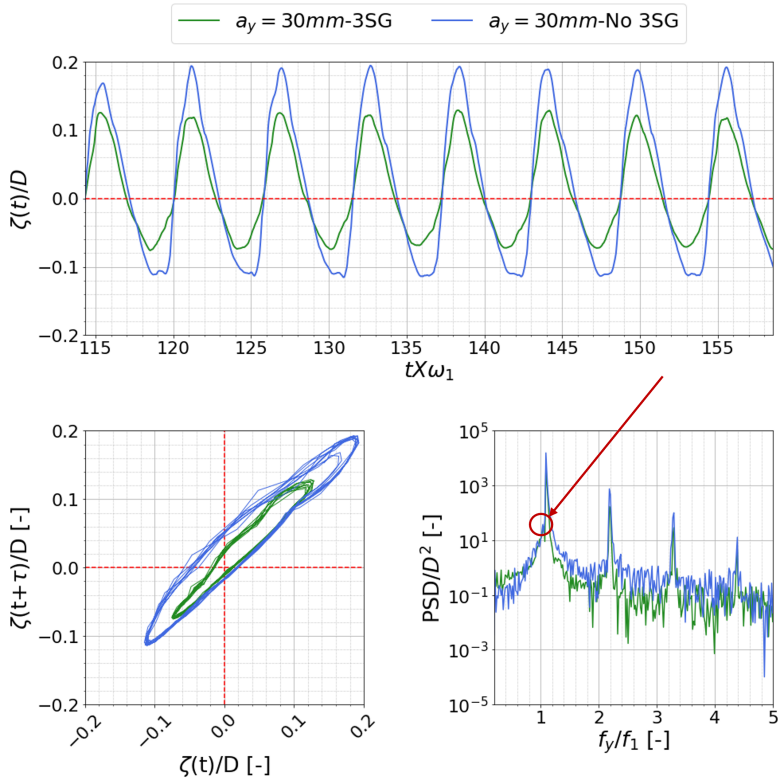

Figure 3.42: Dimensionless time history, phase plane plots and PSD plot for the $a_y = 30$ mm test series st $f_y = 0.98$ Hz for the two structural configuration: wave amplitude for the 3SG configuration is 1.50 times than for the other configuration; phase plane plots outline a stronger wave structure interaction in the nominal configuration; secondary peak at $f_y = 0.91$ Hz

3.5 Scale effect assessment

Main objective in the scale effect assessment for the horizontal harmonic base excitation is to have hints of the effect of the previous consideration, which are made on a simplified experimental case study. The observation could be of interest when a more realistic seismic signal is then performed (§4.5). Scale effect assessment is studied by means of five parameters: forcing amplitude, forcing frequency, wave amplitude, water depth and internal configuration.
Forcing amplitude and frequency are necessary to compute the external forcing acceleration, which is then compared to the ground acceleration by literature. From the similarity in §2.2.1, it's know that:

$$\begin{cases} A_{model} = 0.054 \times A_{ALFRED} \\ f_{model} = 4.29 \times f_{ALFRED} \end{cases} \tag{3.2}$$

where subscript m stands for model and A for ALFRED. External acceleration for the horizontal harmonic base excitation are then as follows:

$$\ddot{a}_t = A_{ALFRED} \times (2\pi f_{ALFRED})^2 = \frac{A_{model}}{0.054} \times \left(2\pi \frac{f_{model}}{4.29}\right)^2 = \frac{\ddot{a}_y}{0.95} \tag{3.3}$$

where $\ddot{a}_t$ stands for the ground acceleration needed to theoretically simulate the harmonic base excitation in a real event scenario.
Wave amplitude is computed because the Froude scaling is valid by the similarity studies [34]:

$$Fr_m = Fr_A \rightarrow \frac{U_m^2}{gD_m} = \frac{U_A^2}{gD_A} \rightarrow U_A = \sqrt{\frac{D_A}{D_m}} U_m \rightarrow \left(\frac{d\zeta}{dt}\right)_A = \sqrt{\frac{D_A}{D_m}} \left(\frac{d\zeta}{dt}\right)_m \tag{3.4}$$

where D_a/D_m =18.4 by the geometry model scaling §2.2.1. The total uncertainty on the wave amplitude measured in the model is equal to 1.352 mm for the P1 probe and to 1.302 mm for the probe P2. In first approximation, the calculation of the uncertainty on ALFRED is simply computed as a wave amplitude value, so it's equal to $\simeq$5.80 mm for P1 and $\simeq$5.59 mm for P2 (§2.5.3).
Table 3.3 presents the scaling-up of the previous parameters on some of the most interesting test series among the harmonic base excitation results.
The effect of the forcing amplitude is highlighted in rows of colour light-yellow: the maximum wave amplitude equal to 0.231 m is reached for a forcing amplitude of $A_{ALFRED} = 0.03\text{m}/0.054 = 0.556\text{m}$, with a theoretical ground acceleration equal to $\ddot{a}_t = 1.081\,\text{m/s}^2$.
The effect of water depth, starting as a convention from the diaphragm in the ALFRED's model because is the region where the majority of the sloshing processes takes place, is outline in the rows in colour light-green: keeping constants the forcing amplitude, the selected frequencies corresponds to the first sloshing ones, which

are equal to the forcing frequencies for those relevant cases. Higher wave amplitude exhibits when the water depth is deeper, but an advantage is that the sloshing frequencies are higher than for the other ones. On the other hand, smaller amplitude are reached for more shallow water conditions, but the maximum amplitude is reached at lower frequencies. In terms of ground acceleration, the maximum value reported is for $h = 9.90$ cm, and it's minor than the higher from the previous comparison for $A_{ALFRED} = 0.556$ m.
The effect of the removal of the three steam generators is the most critical in terms of wave amplitude. Figure 3.38 already exhibits higher wave amplitude in the model for equal k_y dimensionless acceleration in y-direction. In the full scale discussion, supposing that a similar-sinusoidal excitation is experienced in real life events, the ground acceleration is greater than all the previous cases when the hazardous configuration is verified. In the worst-case scenario, wave amplitude reaches 0.357 m in a pool filled of molten lead for a deep equal to 1.627 m, which is the 22% of it.

		Model			ALFRED		
Test series	**3SG**	**h [m]**	$\ddot{a}_y$ [m/s^2]	ζ_m **[m]**	**h_A [m]**	$\ddot{a}_t$ [m/s^2]	ζ_A **[m]**
$a_y = 0.005$m $f_y = 0.98$Hz	Yes	0.088	0.190	0.015	1.627	0.180	0.065
$a_y = 0.015$m $f_y = 0.98$Hz	Yes	0.088	0.569	0.033	1.627	0.540	0.143
$a_y = 0.030$m $f_y = 0.98$Hz	Yes	0.088	1.137	0.054	1.627	1.081	0.231
$a_y = 0.015$m $f_y = 0.85$Hz	Yes	0.050	0.428	0.020	0.920	0.406	0.087
$a_y = 0.015$m $f_y = 0.98$Hz	Yes	0.065	0.569	0.028	1.196	0.540	0.119
$a_y = 0.015$m $f_y = 0.98$Hz	Yes	0.078	0.569	0.032	1.443	0.540	0.139
$a_y = 0.015$m $f_y = 1.04$Hz	Yes	0.088	0.640	0.035	1.627	0.608	0.149
$a_y = 0.015$m $f_y = 1.08$Hz	Yes	0.099	0.691	0.043	1.822	0.656	0.183
$a_y = 0.015$m $f_y = 1.04$Hz	Yes	0.088	0.640	0.035	1.627	0.608	0.149
$a_y = 0.015$m $f_y = 1.04$Hz	No	0.088	0.640	0.053	1.627	0.608	0.229
$a_y = 0.030$m $f_y = 1.12$Hz	Yes	0.088	1.486	0.055	1.627	1.411	0.238
$a_y = 0.030$m $f_y = 1.12$Hz	No	0.088	1.486	0.083	1.627	1.411	0.357

Table 3.3: Scale effect on some selected test series in the horizontal harmonic base excitation with different forcing amplitudes, frequencies, water depths and internal configurations; the uncertainty on the displacements for the wave amplitude in model from capacitance probe P1 is equal to $\simeq$0.0058 m (§2.5.3).

If the theoretical ground acceleration peaks in those horizontal harmonic base excitation are taken into account, the differences in numerical value from a peak in a real scenario are minimum in some cases. The order of magnitude for $\ddot{a}_t$ is of 1 m/s^2 in

Mioveni [34], Romania, the building site of ALFRED. For example, the conventional peak ground acceleration of Turin is $\ddot{a}_t \leq 1.4$ because is a zone 3 in the *Protezione Civile* updated archive [38]. In the end, the mean of the peak ground acceleration of Belgium [39] is reported and is quite low: $\ddot{a}_t = 0.40\,\mathrm{m/s^2}$.

Chapter 4

Earthquakes' simulation test series

In this chapter, the earthquakes' simulation test series have been post-processed. The input signal has been taken from the norm IEC 60068-3-3 and properly scaled in amplitude and frequency to simulate the seismic characterization of the region of interest in Mioveni (Romania) (§2.7.2). To study the sloshing processes during this norm-seismic signal on ALFRED's model, the pseudo spectra of acceleration develops from a maximum value plateau that starts for $f = 0.89$ Hz, while the amplitude is multiplied by ten times the original one.
In the first part of the chapter, a description of the sloshing processes is reported during the norm-base seismic signal applied only in the x-direction when the three steam generators' configuration is set-up and the water depth is $h_{model} = 8.84$ cm. The comparison with the fundamental harmonic base excitation, for a forcing amplitude of $a_y = 5$ mm and a forcing frequency of $f_y = 0.98$ Hz, helps for a better understanding of the randomness of sloshing processes when a seismic event is experienced.
In the second part of the chapter, the shifted-scaled norm-base seismic signal is performed to three different setup. Firstly the effect of water depth is tested for a percentage variation of $\pm 11\%$ and then a hazardous internal configuration is tested when $h_{model} = 8.84$ cm.
In the last part, the shifted-scaled norm-base signal is applied in the three direction, so the output from the capacitance probes is compared with the one-direction signal.

4.1 Norm-base seismic input in one direction

The norm-base seismic simulation in the x-direction of the reference frame attached to the experimental setup it's a simplification of the signal in the three direction. Fundamental harmonic base excitation with a forcing amplitude $a_y = 5$ mm and forcing frequency $f_y = 0.98$ Hz is selected to compare with the results of the seismic simulation, so the dimensionless time is scaled by the pulsation $\omega_1 = 2 \cdot \pi \cdot 0.98$ Hz= 6.158rad/s, and wave amplitude is divided by D. The Figure 4.2 presents the dimensionless time history from the capacitance probes P1 and P2. The motion is nonlinear, as it's suggested in Figure 4.1 by the video captures of the free-liquid surface motion taken in the dimensionless time range from 67.738 to 73.896 ($t \approx [11, 12]$ s). The very last part of the signal is not so useful to study because the input signal, which is amplified by ten times in amplitude, gives a little shock to the shake table to return to the homing position of zero in the three axis of the Cartesian

reference frame. The component of displacement due to the instantaneous arrest is not of interest because is not related to any imposed acceleration by the input signal.

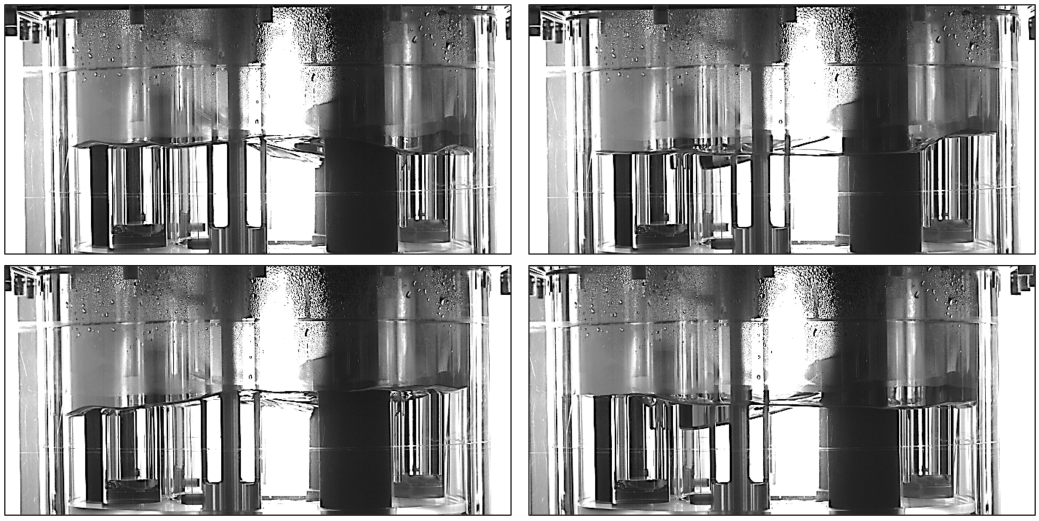

Figure 4.1: Video captures of the free-liquid surface motion taken in the dimensionless time range from 67.738 to 73.896 ($t \approx [11, 12]$ s): surface motion is not planar; internal cylinder sloshing system can be spotted in the second and the fourth capture.

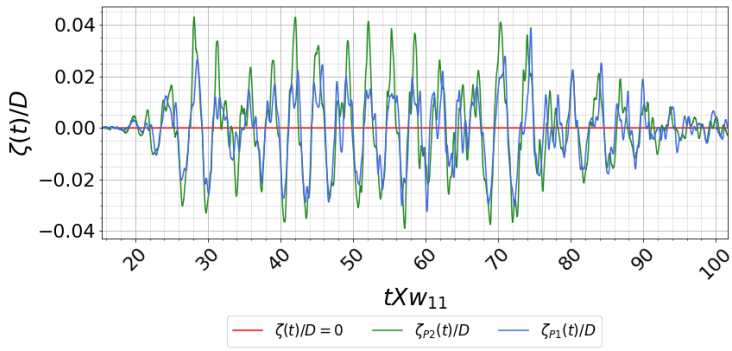

Figure 4.2: Dimensionless time histories for shifted-scaled norm-base test series (which is 10 times increased in amplitude from the original): P1 is in blue and P2 is in green

The PSD plots, in Figure 4.3 are studied in confrontation with the one for the selected harmonic test series. The seismic case represents the first four peaks according to the Pseudo Spectra of Acceleration in the range of 0.89 Hz, as outlined in §2.7.2. Then, in the PSD is way difficult to identify exactly which are the nonlinear component. Higher peaks amplitude is near the harmonic tests one, but on a span of frequencies and not only one peak.

The phase plane plots are very powerful in the comparison within seismic and harmonic study case. as it's shown in Figure 4.4. When the harmonic input at low amplitude is applied, the orbits are on a limited and common curve, while the orbits for the seismic case doesn't follow a path or a specific curve. The greater difference is recorded for the capacitance probe P2, which is near the inner cylinder: sloshing processes are more intense on the internal structure than the harmonic study case.

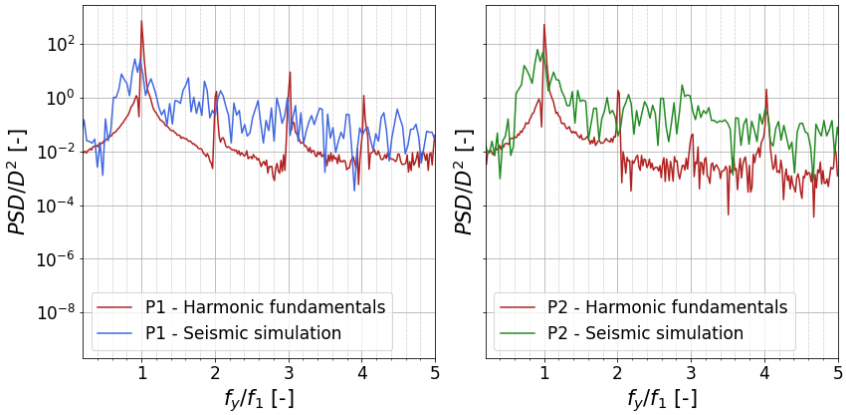

Figure 4.3: Dimensionless PSD plots for the seismic simulation in one direction and the fundamental harmonic in y-direction at $a_y = 5$ mm and $f_y = 0.98$ Hz: the seismic one reflects the plateau in the 0.89 Hz range of the Pseudo Spectra of the Acceleration, while the harmonic case is easier to comment.

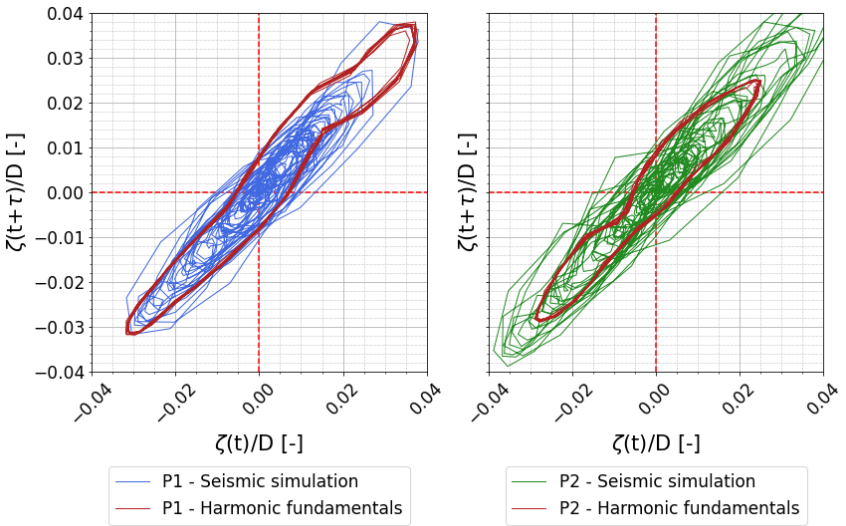

Figure 4.4: Dimensionless phase plane plots for the seismic simulation in one direction and the fundamental harmonic in y-direction at $a_y = 5$ mm and $f_y = 0.98$ Hz: the seismic case is highly random if compared to the harmonic one.

4.2 Effect of water depth

The effect of water depth is studied for the nominal value $h_{model} = 8.84$ cm, $h = 7.84$ cm and $h = 9.90$ cm for simulating an $\pm 11\%$ of the h_{model}, and $h = 6.50$ cm. The tested setup always represents a shallow water condition.
The dimensionless time history in Figure 4.5 exhibits higher wave amplitudes when the water depth is increasing. Similar time evolution of the free-liquid surface is spotted when the water depth is equal to h_{model} and its $\pm 11\%$. The same observation it's about the PSD plot in frequency ratio f_y/f_1 =(0.6,2.2) ($f_y = [0.59, 2.16]$ Hz) range: except from the forcing frequency plateau around 0.89Hz of the input signal, the other nonlinear frequency components very small in amplitude are in common for the three higher test series.
The previous observation is not effective for the lower water depth test series at $h = 6.50$ cm because the similarities cannot be distinctly found: in the zoom of the time history in Figure 4.5 happens that peak/trough for $h = 6.50$ cm doesn't correspond to the one of the other series.

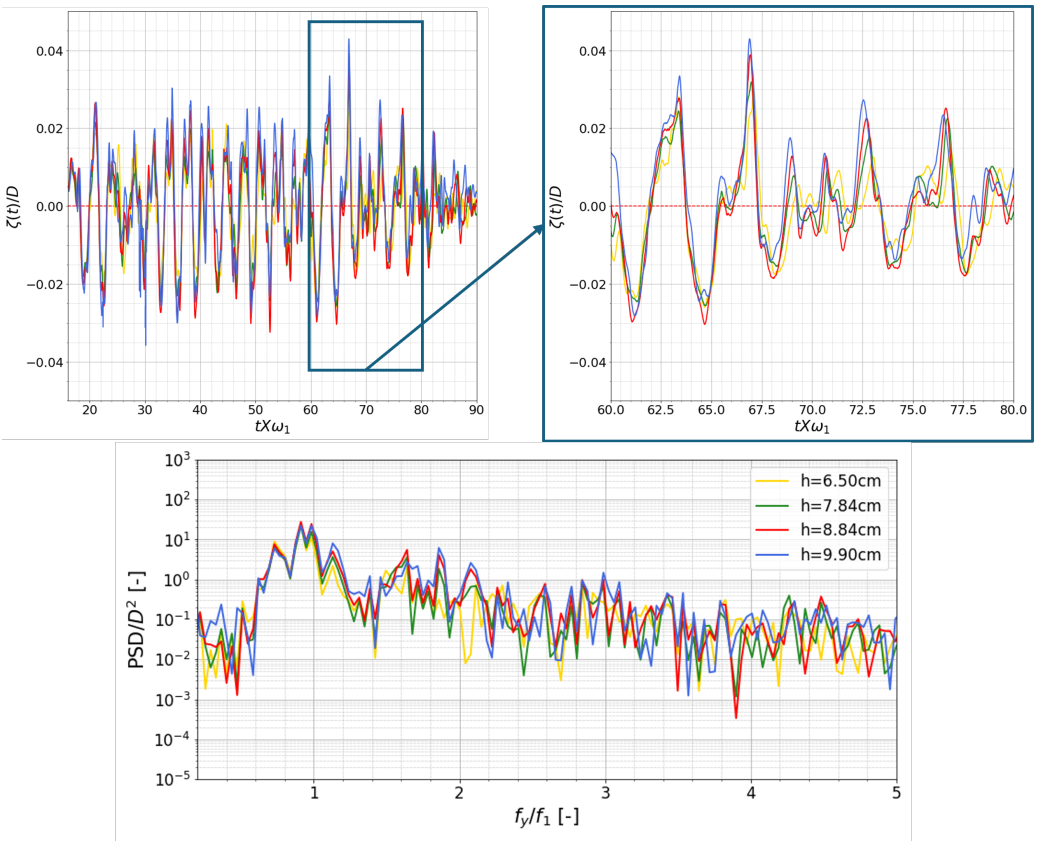

Figure 4.5: Dimensionless time history and PSD plots at different water depth: the wave amplitude is higher in time window within time range $t = [9.7, 12.9]$s; PSD plot is computed on the complete signal.

4.3 Simulation of hazard in the primary pool

The simulation of a hazard in the primary pool is simulated by the removal of the three steam generators out of the model, as in the fundamentals harmonic test series (§3.4).
Time history in Figure 4.6 for the capacitance probe P2 exhibits higher peaks and deeper troughs in the hazardous configuration. The observation is according to the fundamentals harmonic test series. Since the position of the probe is near to the inner cylinder, representing likewise the central nuclear core, more critical sloshing processes are experienced in the hazardous configuration. The PSD plots exhibits the same peaks at the input forcing frequency, and higher secondary peaks related to the nonlinear component are spotted for the modified internal structure. The nonlinear components don't match completely within the two configurations' PSD, suggesting different values as the structural damping in the model is changed.

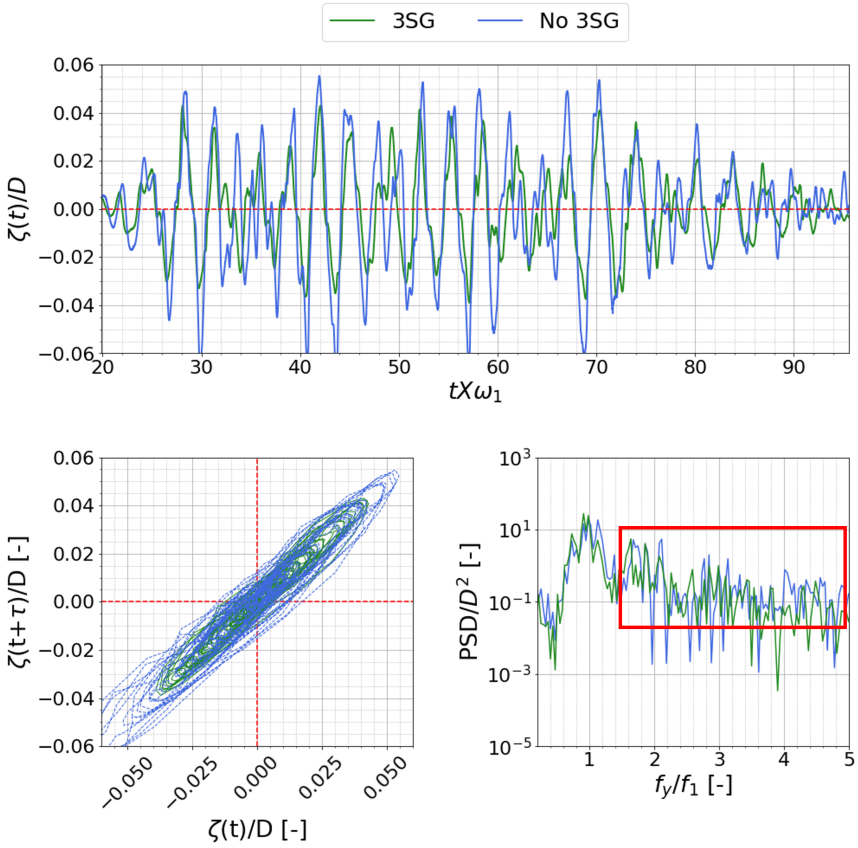

Figure 4.6: Dimensionless time history, phase plane plots PSD plots by the capacitance probe P2 for the seismic test series in one direction at $h_{model} = 8.84$ cm and the configuration with and without the three SG: the wave amplitude is higher in the hazardous configuration and the PSD outline several different nonlinear components.

4.4 Norm-base seismic input in three direction

The norm-base seismic input signal in one direction, which is shifted in frequency and scaled in amplitude, is finally applied in the three directions, basically using the very same signal for the x direction but also in y and z direction of the Cartesian reference frame of the shake table. Results are shown in Figure 4.8 for the capacitance probe P1 and in Figure 4.7 for a sight on the sloshing processes in the model's pool. The wave amplitude confrontation is ten times higher than the *x-only* series when the peaks occur. The simply three dimensions input signal is more critical if compared to any of the previous seismic test series with different water depths or with a hazardous internal configuration but applied in one direction. The norm-base seismic test series only in the x-direction gives back an external acceleration in x equal to $0.629\,\mathrm{m/s^2}$, so applying in the 3DoF case the same norm-base shifted and scaled signal means applying at the same time a peak of equal intensity in all the directions.
Finally, moving the input signals in three directions makes the free-liquid surface motion more critical and harder to predict in the complicated ALFRED's model annular geometry. The wave-structure interaction affects the sloshing processes since the 1 DoF test series, and the effect is way more crucial. The main observation after this comparison within the one DoF and the three DoF cases is the dangerous increasing of the wave amplitude when moving to more realistic seismic simulations. It's critical than studying the simpler cases for moving to the more complicated simulations.

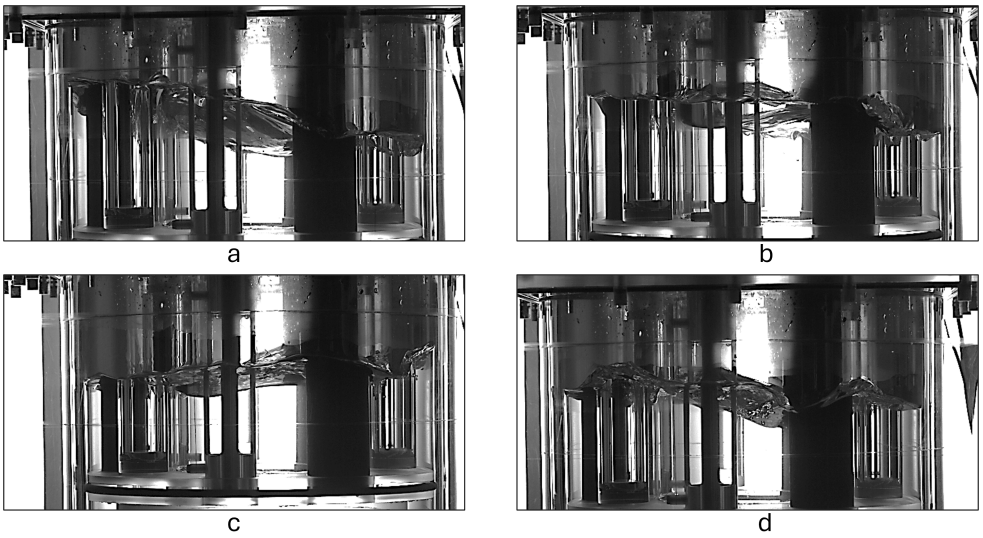

Figure 4.7: Video captures of the free-liquid surface motion taken in the dimensionless time range from 67.738 to 73.896 ($t \approx [11, 12]$s): *a, b, c, d* are consecutive in time; surface motion is not planar and the wave amplitude is greater than the test series in one direction (Figure 4.1).

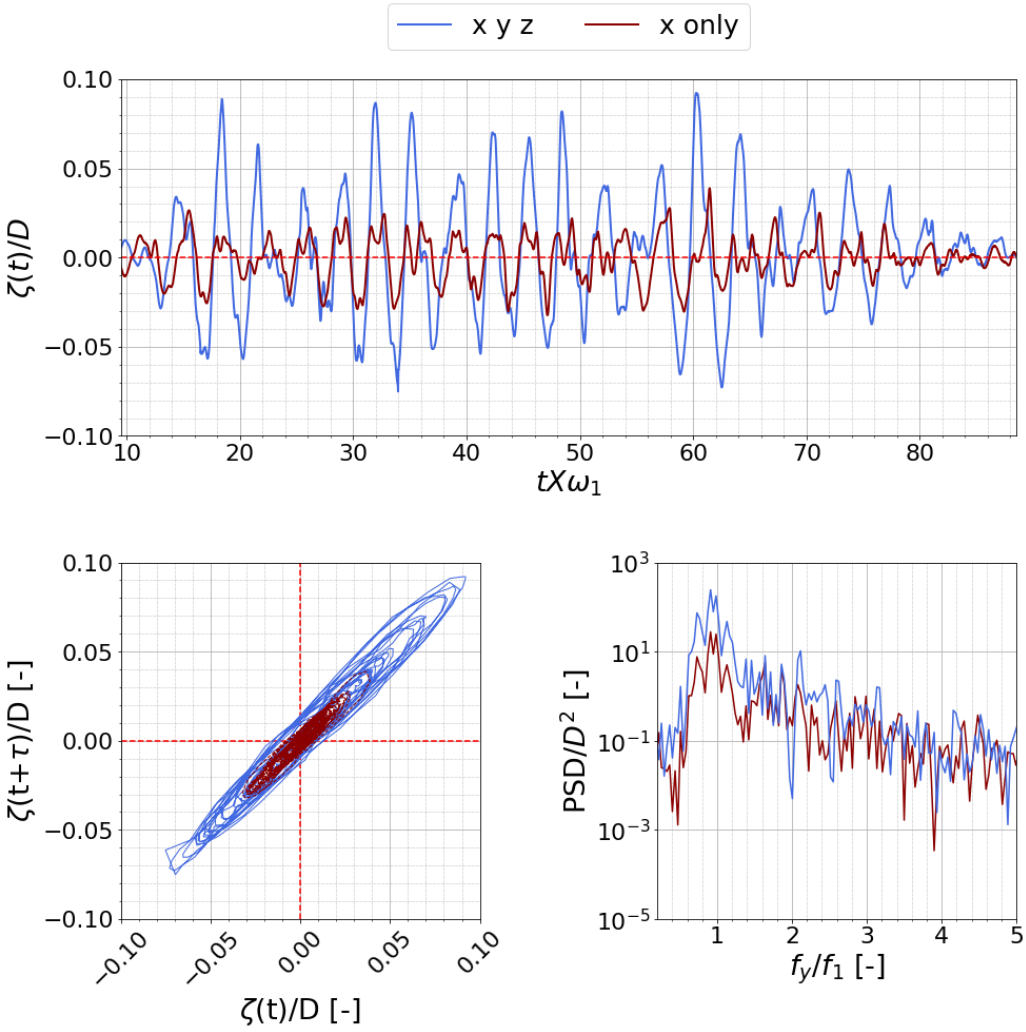

Figure 4.8: Dimensionless time history, phase plane plots PSD plots by the capacitance probe P1 for the seismic test series in one direction and three directions at $h_{model} = 8.84$ cm: when the peaks occur, in the three DoF series the wave amplitude is ten times higher than the one from the *x-only* series.

4.5 Scale effect assessment

The scale effect assessment for the norm-base test series is made taking into account the five parameters already investigated in §3.5: forcing amplitude, forcing frequency, wave amplitude, water depth and internal configuration. The wave amplitude for ALFRED upscaling is computed as in Eq. 3.4 based on the Froude scaling. When the norm base excitation is applied in one direction along x, the peak of the external forcing acceleration is computed for the forcing frequency of $f_x = 0.89$Hz and the maximum forcing amplitude imposed of 20mm:

$$\ddot{a}_t = A_{ALFRED} \times (2\pi f_{ALFRED})^2 = \frac{A_{model}}{0.054} \times \left(2\pi \frac{f_{x,model}}{4.29}\right)^2 = 0.629\,\mathrm{m/s^2} \qquad (4.1)$$

when the conventional water depth is equal to $h = 8.84$ cm.
In Table 4.1 is reported an overview of the most interesting results.

		Model			ALFRED		
Test series	**3SG**	**h [m]**	$\ddot{a}_y$ [m/s^2]	ζ_m **[m]**	**h_A [m]**	$\ddot{a}_t$ [m/s^2]	ζ_A **[m]**
Norm base signal scaled and shifted 1DoF	Yes	0.088	0.652	0.016	1.627	0.629	0.068
$a_y = 0.015$m $f_y = 0.98$Hz 1DoF	Yes	0.088	0.190	0.015	1.627	0.180	0.065
Norm base signal scaled and shifted 1DoF	No	0.088	0.652	0.024	1.627	0.629	0.102
Norm base signal scaled and shifted 3DoF	Yes	0.088	1.158	0.040	1.627	1.10	0.170

Table 4.1: Scale effect on some selected test series in the earthquakes'reproduction norm base excitation with different forcing amplitudes, frequencies, water depths and internal configurations; the uncertainty on the displacements for the wave amplitude in model from capacitance probe P1 is equal to ≃0.0058 m (§2.5.3).

The 1DoF series for the configuration with the three steam generators exhibits highly nonlinear motion, and the maximum wave amplitude reached in the model is equal to ≃15.8 mm±1.351 mm (total uncertainty on the probes measurements §2.5.3). The maximum wave amplitude can be compared to the one in output from the horizontal harmonic base excitation at forcing amplitude 5mm and first sloshing frequency of 0.98 Hz, which is equal to ζ =0.068 m.
The confrontation within the test series results for the configuration with and without the three steam generators is particularly descriptive, as it is when the horizontal harmonic base excitations are applied. The peak of wave amplitude reached is equal to 0.102 m when the hazardous configuration is set up, which is 1.5 times the one when all the tubes in the pool are considered.

The greatest discrepancy in terms of magnitude order is obtained when the norm-base seismic signal is applied in all the direction. The ground acceleration has components in all the three direction at the same time, so when a peak is applied along x then is simultaneously along y and z. The external acceleration vector in its maximum peak has a nominal module equal to:

$$\ddot{a}_t = \sqrt{3 \times A_{ALFRED} \times (2\pi f_{ALFRED})^2} = \frac{A_{model}}{0.054} \times \left(2\pi \frac{f_{x,model}}{4.29}\right)^2 = 1.10\,\mathrm{m/s^2} \tag{4.2}$$

The case is an estimation of the seismic loads built on the region of interest ground acceleration of $\ddot{a}_t = 1\,\mathrm{m/s^2}$ in Mioveni [34]. The wave amplitude in ALFRED reaches peaks 2.5 times higher than in the 1DoF case, for a maximum value of 0.170 m.
The fundamentals harmonic test series make the point on how the maximum wave amplitude can qualitatively increase in the model. Moreover, in the respective scale effect assessment in §3.5, some theoretical horizontal ground accelerations $\ddot{a}_t$ were of the same magnitude order if compared to the $\ddot{a}_t$ peaks of Mioveni [34] and Turin [38] of $1\mathrm{m/s^2}$, which is a medium-low value, and to the mean one of Belgium [39] of $0.40\mathrm{m/s^2}$.
The same value from the report and the literature are represented in the seismic simulations' tests, with the 1DoF signals that make a connection with the previous 1DoF harmonic test series and the following 3DoF seismic tests.
Finally, the importance of the integrity of the internal component in the nuclear reactor is here highlighted. The sloshing processes demand a strong structural damping component in the primary pool. The problem of possible hazard is something that must be avoided and if it occurs have to be stabilized. It's here reported that one of the very first nuclear accident in 1960, that happened in the US on the SL-1 reactor [24], has demonstrated how many damages the cooling water caused hitting the top of the primary pool during that dramatic event.

Chapter 5

Conclusion

A preliminary investigation of the free-liquid surface sloshing motion on the ALFRED's model is presented. Fundamental base harmonic excitations have been post-processed for three forcing amplitudes at $a_y/D = 0.013, 0.039, 0.076$, where D is the external diameter of the tank, and near/at and away $f_y = 0.89$Hz, the estimated numerical first sloshing frequency. The complexity of the annular tank geometry and the internal structures makes the sloshing process hard to predict and to analyse. The wave-structure interaction adds complexity in evaluating the sloshing modes.
A first sloshing mode is basically experienced in each of the harmonic test series, with non-negligible nonlinear components since the smallest external base excitation. Some frequencies can be identified in the PSD for the smallest external amplitude cases. The maximum wave amplitude for the nominal water depth of $h_{model} = 8.84$cm is reached in a frequency range that goes from 0.94Hz to 1.12 Hz. When $a_y/D = 0.076$ ($a_y = 30$mm), a plateau on the maximum amplitude is experienced. The wave steepness increases at higher forcing amplitudes, as well as the motion becomes more violent and critical if studied in similarity with ALFRED.
Shallow water condition has been tested because the geometric dimensions of the special tank don't allow filling enough of the pool to have a deeper water depth. The greater wave amplitude is reached at lower forcing frequency for the smaller water depths, while higher ones lead to more intense sloshing processes. If it's good to have smaller wave amplitudes, on the other hand, it is dangerous to experience resonance at lower frequencies.
A hazardous internal structure has also been tested for the harmonic base excitation, removing the 3D printed tubes representing the steam generators. The motion in the simulated damage configuration is less damped, so is more critical for the model and, in similarity, for the actual demonstrator. Violent motion is easier to be experienced for damaged internal arrangement and higher accelerations.
The seismic test series have been conducted in one direction and in the three directions, for the same water depths and internal configurations set-up for the harmonic base excitation ones. The harmonic ones revealed to be a powerful tool to analyse the experimental investigation of sloshing processes when the norm-base earthquake is simulated. In fact, basically the same previous considerations can be applied when the norm-base input signal is applied in one direction.
Ultimately, the norm-base earthquake in three directions emphasizes the importance of being aware of the fundamental free surface behaviour. Similarly, equipped test series exhibit higher wave amplitude when the signal is simply applied in all the di-

rection and not only in one. The full scale effect assessments show that the seismic simulations and some of the harmonic test series are in agreement with the hypothesis made on the ground accelerations of the regions mentioned.
Finally, it is encountered that sloshing in the primary pool of ALFRED is a problem of concern for the hard-to-predict behaviour, which makes really tricky to provide a numerical model (objective for the sloshing framework of the PASCAL project), and the great amplitudes reached during the dynamic processes. Despite some of the tested conditions are ten times the estimated ones in Mioveni (Romania, the building site for ALFRED), the critical motion experienced also for the simpler and less intense external excitations exhibits the necessity of further investigation of the sloshing processes and, potentially, more accurate models of the demonstrator.
The experimental investigation of sloshing could be improved and could keep into account force measurements by means of the strain gauge sensors, alongside the information on the free surface displacement. A more complete and dedicated experimentation could be done for the vertical excitation, different in more ways from the horizontal ones. Seismic simulation test series could be studied after the post-processing of harmonic external excitation in two and three degree of freedom. Finally, more realistic earthquake signals could be scaled for the shaking facilities for a more useful simulation of extreme events that very potentially lead to catastrophes.

Appendices

Appendix A

Dimensionless analysis

The study case's container can be seen as an excited annular tank partially filled with liquid at a certain height, h. The following hypothesis made are:

1. the fluid is incompressible, so $\nabla\rho = 0$;
2. no heat transfer is considered in the fluid during the sloshing;
3. the volume is laterally moved and is subjected to gravity.

The nomenclature adopted corrected to match with the one of the theory Paragraph 1.3.3. It's known that the equation of mass conservation in Lagrangian form is the following:

$$\frac{D\rho}{Dt} = -\rho(\nabla \cdot \mathbf{q}) \tag{A.1}$$

where $\mathbf{q} = (q_x, q_y, q_z)^T$ is the fluid velocity in a Cartesian reference frame. Given the hypothesis of incompressible and stationary fluid, it's true that $\frac{D\rho}{Dt} = 0$, so the mass conservation equation is written as follows:

$$\nabla \cdot \mathbf{q} = 0, \ \left(\frac{\partial q_x}{\partial x} + \frac{\partial q_y}{\partial y} + \frac{\partial q_z}{\partial z}\right) = 0 \tag{A.2}$$

The momentum conservation equation is written as follows:

$$\frac{\partial \mathbf{q}}{\partial t} + \mathbf{q} \times \nabla\mathbf{u} = -\frac{1}{\rho}\nabla p + \nu\nabla^2\mathbf{q} + \frac{1}{\rho}\mathbf{F} \tag{A.3}$$

where, according to the hypothesis about volumetric forces, $\mathbf{F} = \rho(a_x, 0, -g)^T$, with $g = 9.81 m/s^2$ gravity acceleration along z-direction.
The surface tension needs to be formulated because the sloshing problem is under investigation. It is a quantity affecting the movement of the fluid on its boundary, so it should be considered as a boundary condition.
The conservation equations are scaled as it follows:

$$\nabla^* \cdot \mathbf{q}^* = 0 \tag{A.4}$$

$$\frac{U}{\tau}\frac{\partial \mathbf{q}^*}{\partial t^*} + \frac{U^2}{L}\mathbf{q}^* \times \nabla^*\mathbf{q}^* = -\frac{U^2}{L}\nabla^* p^* + \mu\frac{U}{\rho L^2}\nabla^{*^2}\mathbf{q}^* + g\mathbf{a}^* \tag{A.5}$$

where the physical quantity and maths operator ∇ has been made dimensionless by means of: U, the characteristic system velocity, τ, the characteristic timescale, and L is the characteristic length scale.
The *Strouhal number* $St = \frac{L}{U\tau}$, the *Reynolds number* $Re = \frac{UL}{\nu} = \frac{UL\rho}{\mu} = [m^2/s]$, and the $Fr = \frac{U^2}{gL}$ are introduced in the dimensionless momentum equation. In the

current study case, L is the radius R of the cylinder, while the characteristic time τ of sloshing phenomenon is the inverse of pulsation $\tau = \omega^{-1}$.
Momentum equation can be written in the canonical form for the convection:

$$St\frac{\partial \mathbf{q}^*}{\partial t^*} + \mathbf{q}^* \times \nabla^* \mathbf{q}^* = -\nabla^* p^* + \frac{1}{Re}\nabla^{*^2}\mathbf{q}^* + \frac{1}{Fr}\mathbf{a}^* \tag{A.6}$$

Momentum conservation in Eq. A.6, can be re-write once again in the canonical form for non-dimensional acceleration $\mathbf{a}^*$ as follows:

$$\Lambda\frac{\partial \mathbf{u}^*}{\partial t^*} + \frac{1}{Fr}\mathbf{u}^* \times \nabla^* \mathbf{u}^* = -\frac{1}{Fr}\nabla^* p^* + \frac{Fr}{Re}\nabla^{*^2}\mathbf{u}^* + \mathbf{a}^* + \frac{1}{Bo}\kappa^*\nabla^*\alpha \tag{A.7}$$

where $\Lambda = \frac{U}{\tau g}$. Eq. A.7 takes into account the *surface tension* by *Bond number*. It indicates the relative effect within gravitational forces and tension of the surface of interface, and it's defined as:

$$Bo = \frac{\rho g L^2}{\sigma} \tag{A.8}$$

where σ is the *surface tension* and, as always, L indicates the hydraulic diameter of reference.
According to the technical report of reference [34], Bond number it's negligible when compared to the other physical phenomena taking place.
If a sinusoidal excitation along *x-axis* side is considered, as displacement $X = Asin(\omega t)$, and the velocity U is equal to excitation velocity $U = \frac{\partial X}{\partial t} \sim A\omega$, so the characteristic numbers are the following:

$$St = \frac{L}{U\tau} = \frac{R}{A}$$

$$Re = \frac{AR\omega}{\nu}$$

$$Fr = \frac{A^2}{R}\frac{\omega^2}{g}$$

Appendix B

Monte Carlo method

The data are read from the files taken at each height, whom structure is explained in the previous paragraph 2.5.1. In the code below is presented the input section of the used code *Calibration_MC_Capacitance.py*. In it, the filenames are properly saved because they were previously saved in a summary file that connects the singular names to the corresponding height. Besides, the number of test is then saved keeping in account the number of file name read from the summary file. It's fundamental to remember that is the one read on the ruler external to the mockup, so the reference system is not the one in Figure 2.9. The architecture of the summary file *Calibration_file_2023_11_06.csv* is in such a way that near to the filename there's the corresponding height read on the external ruler, so at 30mm corresponds the highest water depth that the mockup can allow.

```
# Input
#name_file = "CalibrationData"
path_file=r'OUTPUT CALIBRATION FILE COMPLETE PATH NAME'
path_file_orig=r'PATH OF THE CALIBRATION FILE IN INPUT'
#text_file = 'Calibration_Data.csv'
text_file='Calibration_file_2023_11_06.csv'
name_file = np.genfromtxt(path_file_orig+text_file, delimiter=',')
# Read the CSV file into a pandas DataFrame
df = pd.read_csv(path_file_orig+text_file, header=0)
size_tab = np.shape(name_file)
n_test = size_tab[0]
```

Listing B.1: *Calibration_MC_Capacitance.py*: Input section

In the code below, the initialization of the variables is presented. These variables are meant to contain the input PDF extracted from the data.

```
#%% Variable initialisation
list_v=[]
ll=[]
list_c=[]
M_V=[] # Voltage
Results_C=[]
val_P = np.zeros((3, 8, n_test))  # Initialize the val_TC array with zeros
i_c = 0
```

```
tab_loi_norm = np.zeros((3, 3, n_test))
plt.ioff()
```

Listing B.2: *Calibration_MC_Capacitance.py*: Variable initialization

In the code below, an estimation of the input PDFs is provided. These functions are the input to the Monte Carlo method, that is applied later in this code file. The outer loop is used to move within the test cases (`for it in range (n_test-1)`), extract the data from each of them (`abb = pd.read_csv(path_file+ligne_test[0]+'.txt',delimiter="", decimal=",", header=22)`) and finally save them as numerical array, keeping in mind the architecture of those files (Figure 2.10). Once the data are extracted, the inner loop provides the estimation of the mean value, the standard deviation, the minimum value and the maximum value of each of the probes for the selected file test (notice that the inner loop, `for i_tc in range (3)`, is setted to count the three columns of the test file extracted in the outer loop). Then, by means of the package `norm`, on those data for the `i_tc` probe a normal distribution is computed and saved on the already initialized array (`tab_loi_norm`, its architecture is in Figure B.1).

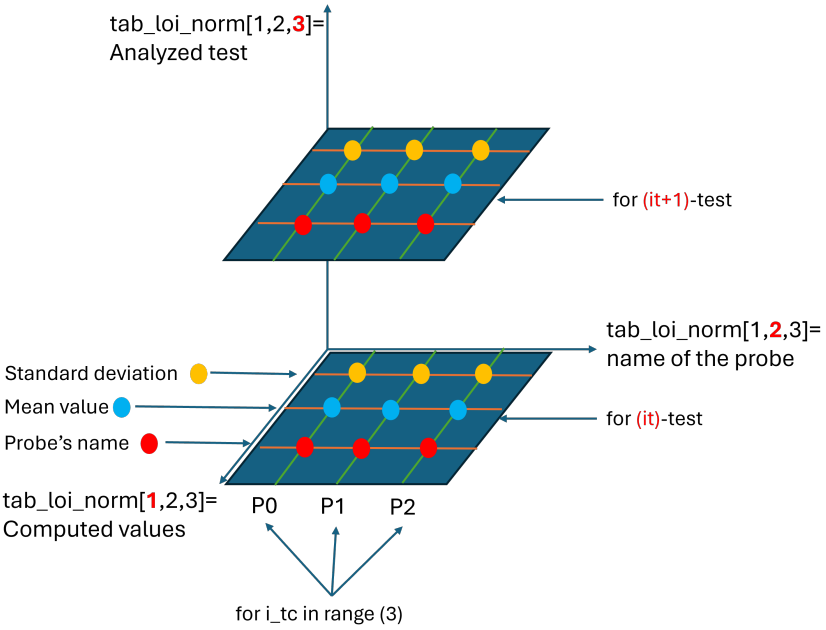

Figure B.1: Architecture of the summary array `tab_loi_norm`

```
#%% Probes calculation
# Extraction of the value of the TC and calculation of several quantities
with tqdm(total=n_test-1, desc="Recuperation de points...") as pbar:
    for it in range(n_test-1):
```

```
        pbar.update(1)
        ligne_test = df.iloc[it, :]

        list_c.append(it)
        #ab = np.genfromtxt(ligne_test[9])  # Read data using NumPy
        abb = pd.read_csv(path_file+ligne_test[0]+'.txt', delimiter="\t", decimal=",", header=22)

        ab=abb.to_numpy()
        #ab0 = np.genfromtxt(path_file+ligne_test[0]+'.txt', delimiter=',') # Read data using NumPy
        #ab=ab0[1:] # Remove the first array of float
        for i_tc in range(3): #number of the capacitance probe
            val_P[i_tc, 0, i_c] = np.mean(ab[:, i_tc+1])
            val_P[i_tc, 1, i_c] = np.std(ab[:, i_tc+1])
            val_P[i_tc, 2, i_c] = np.min(ab[:, i_tc+1])
            val_P[i_tc, 3, i_c] = np.max(ab[:, i_tc+1])
            val_P[i_tc, 4, i_c] = 1  # input voltage
            val_P[i_tc, 5, i_c] = 1.96 * np.std(ab[:, i_tc])  # 97.5% confidence degree for an infinity of tests
            val_P[i_tc, 6, i_c] = 100 # freq acq
            val_P[i_tc, 7, i_c] = 200  # N points

            aa_norm = ab[:, i_tc+1]
            # pdf calculation - normal law - uncertainty - TC
            pdd = norm.fit(aa_norm)  # Fit a normal distribution
            tab_loi_norm[0, i_tc, it] = i_tc
            tab_loi_norm[1, i_tc, it] = pdd[0]  # Mean of the fitted distribution
            tab_loi_norm[2, i_tc, it] = pdd[1]  # Standard deviation of the fitted distribution

        i_c += 1
        Results_C.append(3)
```

Listing B.3: *Calibration_MC_Capacitance.py*: Probes calculation

The code below sets the height of reference for each of the calibration file. In particular, it's setted that the mean value is the one read from the external ruler on the mockup (Figure 2.12a) and the standard deviation on it coincides with the ruler error equal to $0.5mm$. The array named `tab_loi_normpt` is dedicated to save these mean values and standard deviations.

```
#%% Height calculation
tab_loi_normpt = np.zeros((2, n_test))
df_shape=df.shape

with tqdm(total=n_test-1, desc="Height...") as pbar:
```

```
    for it in range(n_test-1):
        pbar.update(1)

        ligne_test = df.iloc[it, :]

        mean_normpt = ligne_test[1]
        std_normpt = 0.5 #reading mistake ruler

        tab_loi_normpt[:, it] = [mean_normpt, std_normpt]

        plt.close('all')
```

Listing B.4: *Calibration_MC_Capacitance.py*: Height calculation

The code below perform 50000 repetition of the Monte Carlo method on the PDFs extracted previously. First, fitting variable are initialized: `fit_list_mont` for storing the random values of fitting slope, intercepts and correlation indexes; `m_fit` the final slope of the calibration law for each of the probes; `q_fit` the final intercepts of the calibration law for each of the probes; `dx_fit` the uncertainty for each probe measurement.
The code is divided in three loops. The outer loop enters each of the probe data (`i_tc` index in range(3)). The first inner loop sets the number of the Monte Carlo repetitions to 50000 cycles. Besides, it creates the array for saving the random values. The third loop generates a random number (`rtc` for the probes and `rtp` for the height on the external ruler) based on the normal distribution, which mean value and standard deviation are stored in `tab_loi_norm`. These values are then saved queuing the arrays `r_listtc` and `r_listpt`. Outside this last loop and at the end of the second, these arrays are needed to upload the `fit_list_mont`, whom save the slope (0), the intercept(1) and the correlation (2) (`fit_list_mont`[**1**,2,3]) for each repetition (`fit_list_mont`[1,**2**,3]) of each probe (`fit_list_mont`[1,2,**3**]). In fact, a computation of the interpolation for the linear fit is provided: `fitxy_pt = np.polyfit(r_listtc, r_listpt, 1)`. The correlation index is equal to `rsq_ikk = np.corrcoef(r_listtc, r_listpt)[0, 1]`^{2} and express how much a linear fit is suitable for the statistical analysis.

```
#%% Monte Carlo calculation
from scipy.stats import norm

# Calculate the sizes of the matrices
s_norm_tc = tab_loi_norm.shape
s_norm_pt = tab_loi_normpt.shape

# Initialize variables
fit_list_mont = np.zeros((3, 50000, 3))
m_fin = np.zeros((3, 2))
```

```
q_fin = np.zeros((3, 2))
dx_fin = np.zeros((3, 1))

# Loop over different i_tc values
for i_tc in tqdm(range(3), desc="i_tc loop"): #each probe
    # Display progress bar for Monte Carlo runs
    with tqdm(total=50000, desc=f"i_tc {i_tc + 1} - Monte Carlo runs") as pbar_ikk:
        # Loop over ikk values
        for ikk in range(50000):
            pbar_ikk.update(1)

            # Initialize arrays to store random values
            r_listtc = []
            r_listpt = []

            # Loop over i_essai values
            for i_essai in range(s_norm_tc[2]):
                # Generate random values based on normal distribution
                rtc = np.random.normal(tab_loi_norm[1, i_tc, i_essai], tab_loi_norm[2, i_tc, i_essai])
                r_listtc.append(rtc)
                rpt = np.random.normal(tab_loi_normpt[0, i_essai], tab_loi_normpt[1, i_essai])
                r_listpt.append(rpt)

            # Fit linear polynomial to the generated data
            fitxy_pt = np.polyfit(r_listtc, r_listpt, 1) # fit of the h_liq = f(Voltage)
            rsq_ikk = np.corrcoef(r_listtc, r_listpt)[0, 1] ** 2

            # Store the results in the fit_list_mont array
            fit_list_mont[0, ikk, i_tc] = fitxy_pt[0]
            fit_list_mont[1, ikk, i_tc] = fitxy_pt[1]
            fit_list_mont[2, ikk, i_tc] = rsq_ikk
```

Listing B.5: *Calibration_MC_Capacitance.py*: Monte Carlo Calculation

In the last part of the code, a norm distribution is built on the 50000 values for the slope and the intercept of each probe, stored in `fit_list_mont`. At the end, the code gives in output for each probe a mean value for the slope m_i of the curve, its intercept q_i and their standard deviation δm_i and δq_i. The law for each $i - probe$ is the following,

$$h_i = m_i X V_i + q_i \tag{B.1}$$

with h_i the free surface height (mm), V_i the output voltage (V) and m_i and q_i the fitting couple.

Appendix C

Acquisition program

The results are obtained by means of a proper `LabView` program designed for the PASCAL project purpose by Julien de Decker. The source-code file runs on a different PC from the one that provide the input signal to the shaking table (Figure **??**). The data are acquired by means of an ARDUINO for the Octopus Acceleration system and from the NI DAQ 9234 for the PCB accelerometer and the capacitance probes. The PC mentioned collect data by usage of the USB ports.
Once the data are acquired, they are saved in a *.tdms* file. The Figure C.1 shows a screenshot of the first sheet of the generated output file. In orange is outlined the information concerning the primary set of accelerometers, operating at a frequency equal to $200Hz$ and the data of all these accelerations are saved in the sheet *Acceleration*. In green is outlined the data acquired with the DAQ system, so the P0 P1 and P2 1D liquid free surface motion, and the acceleration from the PCB. Those data can be seen in the sheet named *Extra sensors* The frequency of acquisition of those data is obtained by computing the inverse of the increment name $wf\_increment$, so equal to $2048Hz$ in the Figure C.1 case. This frequency could then request the re-sampling of the data for the post-processing. It's outlined that the sampling frequency is correctly equal to $200Hz$, as the one from the ARDUINO.

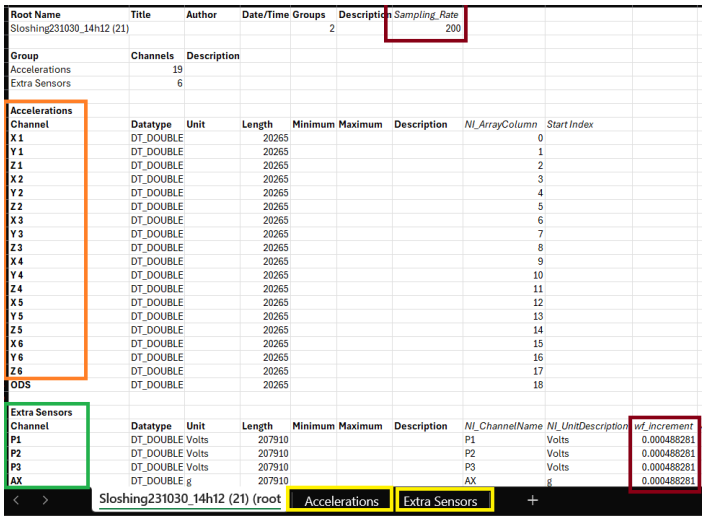

Root Name	Title	Author	Date/Time	Groups	Description	Sampling_Rate
Sloshing231030_14h12 (21)				2		200

Group	Channels	Description
Accelerations	19	
Extra Sensors	6	

Accelerations

Channel	Datatype	Unit	Length	Minimum	Maximum	Description	NI_ArrayColumn	Start Index
X 1	DT_DOUBLE		20265				0	
Y 1	DT_DOUBLE		20265				1	
Z 1	DT_DOUBLE		20265				2	
X 2	DT_DOUBLE		20265				3	
Y 2	DT_DOUBLE		20265				4	
Z 2	DT_DOUBLE		20265				5	
X 3	DT_DOUBLE		20265				6	
Y 3	DT_DOUBLE		20265				7	
Z 3	DT_DOUBLE		20265				8	
X 4	DT_DOUBLE		20265				9	
Y 4	DT_DOUBLE		20265				10	
Z 4	DT_DOUBLE		20265				11	
X 5	DT_DOUBLE		20265				12	
Y 5	DT_DOUBLE		20265				13	
Z 5	DT_DOUBLE		20265				14	
X 6	DT_DOUBLE		20265				15	
Y 6	DT_DOUBLE		20265				16	
Z 6	DT_DOUBLE		20265				17	
ODS	DT_DOUBLE		20265				18	

Extra Sensors

Channel	Datatype	Unit	Length	Minimum	Maximum	Description	NI_ChannelName	NI_UnitDescription	wf_increment
P1	DT_DOUBLE	Volts	207910				P1	Volts	0.000488281
P2	DT_DOUBLE	Volts	207910				P2	Volts	0.000488281
P3	DT_DOUBLE	Volts	207910				P3	Volts	0.000488281
AX	DT_DOUBLE	g	207910				AX	g	0.000488281

Figure C.1: Test file *.tdms* architecture: in orange is outlined the information concerning the primary set of accelerometers, in green is outlined the data acquired with the DAQ system; the frequency of acquisition of those data is obtained by computing the inverse of the increment name $wf\_increment$

Appendix D

Harmonic base excitation in 1 DoF

D.1 Sine signal at constant amplitude and constant frequency in X-direction

```
import numpy as np
import pandas as pd
import matplotlib.pyplot as plt
from scipy.signal import chirp

#-------------------------------------------------

# Note: If you want to use zero for frequencies f_x, f_y, and f_z, use a very
# small value instead of zero, as the 'chirp' function can have trouble
# with zero value in frequencies.

#-------------------------------------------------
# Constant values
FT = 200  # Sampling Frequency [Hz]
t_signal = 60  # Duration of the constant signal [s]
t_ramp_start = 10  # Duration of the starting ramp [s]
t_ramp_end = 10  # Duration of the ending ramp [s]

t_tot = t_ramp_start + t_signal + t_ramp_end
t = np.arange(0, t_tot + 1/FT, 1/FT)  # Time vector [s]
g = 9.81  # Gravity acceleration [m/s^2]

#-------------------------------------------------
# Vectors of parameters for the FOR LOOP with importation from .xlsx file
file = (r'C:\Users\vitog\OneDrive\Desktop\Tesi\Lab\Input_horizontal_excitation\Harmonic_values.xlsx')  # Replace with the actual file path
sheet = 'X_direction'

# Replace 'your_file.xlsx' with the actual file path
file_path = file

# Replace 'Sheet1' with the name of the sheet containing your data
sheet_name = sheet
```

```
33
34 # Import f_x_vec, f_x_file_name_vec
35 df = pd.read_excel(file_path, sheet_name=sheet_name)
36 f_x_vec = df['f_[Hz]']
37
38 # Import Amp_x_acc_vec and Amp_x_poss_name_vec
39 Amp_x_acc_vec = df['a_acc_x_[m/s^2]']
40
41 #-------------------------------------------------
42 # Initialize an empty matrix to store the position vector in one
       matrix
43 matrix_of_Poss = np.empty((len(t), 0))
44
45 #-------------------------------------------------
46 # Starting FOR LOOP
47 # generating N-sine signals along x-direction
48 total_number_of_signals = len(f_x_vec)
49
50 for i in range(total_number_of_signals):
51 #for i in (0,2):
52     # Assign Parameters
53     f_x = f_x_vec[i]
54     Amp_x_acc = Amp_x_acc_vec[i]
55
56     # Assembling Acceleration Amplitude
57     Amp_array_x = np.full_like(t, Amp_x_acc)
58 # Building of the starting and ending ramping in amplitude of the
       sine signal
59     value_to_extract_up_to_start = t_ramp_start
60     t_start = t[t <= value_to_extract_up_to_start]
61     m_start = Amp_x_acc / t_ramp_start
62     Amp_array_x[:len(t_start)] = m_start * t_start
63
64     value_to_extract_up_to_end = t_ramp_end
65     t_end = t[t >= (t_tot - value_to_extract_up_to_end)]
66     m_end = Amp_x_acc / t_ramp_end
67     Amp_array_x[-len(t_end):] = -m_end * (t_end - (t_tot -
      t_ramp_end))
68     Amp_array_x[-len(t_end):] = -Amp_array_x[-len(t_end):][::-1]
69
70     # Sine sweep in X direction
71     beta = 0  # because it's a constant signal
72     f_t = f_x + beta * t
73     sine_signal_x = chirp(t, f0=f_x, f1=f_x, t1=t_tot, method='
      linear')
74     sine_signal_x = sine_signal_x * Amp_array_x
75     Amp_x_pos = -sine_signal_x / (4 * np.pi ** 2 * f_t ** 2)
76
77     # Converting from [m] to [mm]
78     Poss = Amp_x_pos * 1000
```

```
79      #-----------------------------------------------
80      # ORGANIZING MATRIX OF POSITION IN TIME ACCORDING TO
        SHAKESPEARE CONTROL
81      # UNIT INPUT FILE:
82      # Round the elements of the Poss array to 3 decimal places
83      Poss = np.round(Poss, 3)
84      # Set the first row to zeros - LIMITATION ON SHAKESPEARE
        CONTROL UNIT
85      Poss[0] = 0
86      #-----------------------------------------------
87      # Assembling poistion matrix
88      matrix_of_Poss = np.column_stack((matrix_of_Poss, Poss))
89      #-----------------------------------------------
90      # Plotting of the signals
91      plt.figure()
92      plt.subplot(2, 1, 1)
93      # Plot the position along X
94      plt.plot(t, Poss/1000)
95      plt.plot(t, np.zeros(len(Poss)), 'r--')  # Plot the zero line
96      plt.title('Position along X')
97      plt.xlabel('time [s]')
98      plt.ylabel('Position [m]')
99      plt.grid(True)
100     plt.minorticks_on()
101     plt.grid(which='minor', linestyle=':', linewidth=0.5, color='
        black')
102     plt.subplot(2, 1, 2)
103     # Plot the acceleration along X
104     plt.plot(t, sine_signal_x)
105     plt.plot(t, np.zeros(len(Poss)), 'r--')  # Plot the zero line
106     plt.title('Acceleration along X')  # Corrected title
        placement
107     plt.xlabel('time [s]')
108     plt.ylabel('Acceleration [m/s^2]')
109     plt.grid(True)
110     plt.minorticks_on()
111     plt.grid(which='minor', linestyle=':', linewidth=0.5, color='
        black')
112     plt.tight_layout()  # Add this line for proper layout
113     # Show the plot
114     plt.show()
```

D.2 Sine signal at constant amplitude and constant frequency in Z-direction

```
1 import numpy as np
2 import pandas as pd
3 import matplotlib.pyplot as plt
```

```
from scipy.signal import chirp

#-----------------------------------------------
# Parameters
FT = 200  # Sampling Frequency [Hz]
f_x_exc = 1.0413  # [Hz]
f_z = 2.2293  # [Hz]
Az = 30  # [mm]
Ax_exc = 15  # [mm]
t_tot = 80  # [s]
t_excitation = 20  # [s]
t_start_x = 4 / f_x_exc  # Duration of starting ramp [s]
t_end_x = 4 / f_x_exc  # Duration of ending ramp [s]
t_cost_x=t_excitation-(t_start_x + t_end_x)  # Duration of the constant signal
t_start_z = 4 / f_z  # Duration of starting ramp [s]
t_end_z = 4 / f_z  # Duration of ending ramp [s]
t_cost_z=t_tot-(t_start_z + t_end_z)  # Duration of the constant signal [s]
#-----------------------------------------------
# Time vector
t = np.arange(0, t_tot + 1 / FT, 1 / FT)  # Time vector [s]
t_array_exct = np.arange(0, t_excitation + 1 / FT, 1 / FT)  # [s]
#-----------------------------------------------
#AMPLITUDE FOR HORIZONTAL INITIAL EXCITATION
# Amplitude of the signal (X-direction excitation)
Ax_exc = Ax_exc * 1e-3  # [m] conversion from mm to m
Amp_array_x = Ax_exc * np.ones(len(t_array_exct))

# Calculate amplitudes with ramps
value_to_extract_up_to_start = t_start_x
t_start = t_array_exct[t_array_exct ≤ value_to_extract_up_to_start]
m_start = Ax_exc / t_start_x
Amp_array_x[:len(t_start)] = m_start * t_start

value_to_extract_up_to_end = t_end_x
t_end=t_array_exct[t_array_exct≥(t_excitation-value_to_extract_up_to_end)]
m_end = Ax_exc / t_end_x
Amp_array_x[-len(t_end):]=m_end*(t_end-(t_excitation - t_end_x)*np.ones(len(t_end)))
Amp_array_x[-len(t_end):] = Amp_array_x[-len(t_end):][::-1]
#-----------------------------------------------
#AMPLITUDE FOR VERTICAL EXCITATION
# Amplitude of the signal (Z-direction)
Az = Az * 1e-3  # [m] conversion from mm to m
Amp_array_z = Az * np.ones(len(t))

# Calculate amplitudes with ramps
```

```
value_to_extract_up_to_start = t_start_z
t_start = t[t ≤ value_to_extract_up_to_start]
m_start = Az / t_start_z
Amp_array_z[:len(t_start)] = m_start * t_start

value_to_extract_up_to_end = t_end_z
t_end = t[t ≥ (t_tot - value_to_extract_up_to_end)]
m_end = Az / t_end_z
Amp_array_z[-len(t_end):] = m_end * (t_end - (t_tot - t_end_z) * np.ones(len(t_end)))
Amp_array_z[-len(t_end):] = Amp_array_z[-len(t_end):][::-1]
#-------------------------------------------------
# Sine sweep in Z direction
sine_signal_z = chirp(t, f0=f_z, f1=f_z, t1=t_tot, method='linear')
sine_signal_z = sine_signal_z * Amp_array_z
sine_signal_z = sine_signal_z * 1000  # Conversion to [mm]

# Plotting
plt.figure()
plt.plot(t, sine_signal_z)
plt.plot(t, np.zeros(len(sine_signal_z)), 'r--')
plt.title('Position along Z')
plt.xlabel('time [s]')
plt.ylabel('Position [mm]')
plt.ylim(-40, 40)
plt.grid(True)
plt.minorticks_on()
plt.grid(which='minor', linestyle=':', linewidth=0.5, color='black')
#-------------------------------------------------
#ASSEMBLING WITH HORIZONTAL INITIAL EXCITATION
# Section for vertical excitation with horizontal start
sine_signal_exc = chirp(t_array_exct, f0=f_x_exc, f1=f_x_exc, t1=t_excitation, method='linear')
sine_signal_exc = sine_signal_exc * Amp_array_x

# Assembling the signal
sine_signal_exc = sine_signal_exc[:-1]
sine_signal_z = sine_signal_z[:-1]

sine_signal_z = np.concatenate((np.zeros(len(sine_signal_exc) // 2), sine_signal_z))
sine_signal_exc = np.concatenate((sine_signal_exc, np.zeros(len(sine_signal_z) - len(sine_signal_exc))))
sine_signal_exc = sine_signal_exc * 1000

# Effective time, considering the initial horizontal excitation
t_tot_effective = t_excitation / 2 + t_tot
```

```
effective_time = np.arange(0, t_tot_effective + 1 / FT, 1 / FT)[:-1]

# Plotting the final signals
plt.figure()
plt.subplot(2, 1, 1)
plt.plot(effective_time, sine_signal_exc)
plt.title('Position along X')
plt.xlabel('time [s]')
plt.ylabel('Position [mm]')
plt.xlim(0, 20)
plt.ylim(-40, 40)
plt.grid(True)
plt.minorticks_on()
plt.grid(which='minor', linestyle=':', linewidth=0.5, color='black')
plt.subplot(2, 1, 2)
plt.plot(effective_time, sine_signal_z)
plt.title('Position along Z')
plt.xlabel('time [s]')
plt.ylabel('Position [mm]')
plt.xlim(0, 20)
plt.ylim(-40, 40)
plt.grid(True)
plt.minorticks_on()
plt.grid(which='minor', linestyle=':', linewidth=0.5, color='black')
plt.tight_layout()  # Add this line for proper layout

plt.figure()
plt.plot(effective_time, sine_signal_exc, effective_time, sine_signal_z)
plt.xlabel('time [s]')
plt.ylabel('Position [mm]')
plt.legend(['Sine signal in X', 'Sine Signal in Z'])
plt.ylim(-40, 40)
plt.grid(True)
plt.minorticks_on()
plt.grid(which='minor', linestyle=':', linewidth=0.5, color='black')

# Final signal
Signal = np.column_stack([sine_signal_exc, np.zeros(len(sine_signal_exc)), sine_signal_z])
```

D.3 Sine signal at constant amplitude and constant frequency in the three spacial directions

```
import numpy as np
import pandas as pd
import matplotlib.pyplot as plt
from scipy.signal import chirp

#-------------------------------------------------
# PARAMETERS
FT = 200  # Sampling Frequency [Hz]
# Frequency of signals
f_x = 0.2  # [Hz]
f_y = 0.7  # [Hz]
f_z = 2    # [Hz]
# Ramping time and signal durations
t_tot = 120
t_start_x = 4 / f_x
t_end_x = 4 / f_x
t_cost_x = t_tot - (t_start_x + t_end_x)
t_start_y = 4 / f_y
t_end_y = 4 / f_y
t_cost_y = t_tot - (t_start_y + t_end_y)
t_start_z = 4 / f_z
t_end_z = 4 / f_z
t_cost_z = t_tot - (t_start_z + t_end_z)
# Amplitude of position in [mm]
Ax = 30  # [mm]
Ay = 0   # [mm]
Az = 20  # [mm]
#-------------------------------------------------
# Time vector
t = np.arange(0, t_tot + 1 / FT, 1 / FT)
#-------------------------------------------------
# X-direction
Ax = Ax * 1e-3  # Conversion from mm to m
Amp_array_x = Ax * np.ones(len(t))

value_to_extract_up_to_start = t_start_x
t_start = t[t ≤ value_to_extract_up_to_start]
m_start = Ax / t_start_x
Amp_array_x[:len(t_start)] = m_start * t_start

value_to_extract_up_to_end = t_end_x
t_end = t[t ≥ (t_tot - value_to_extract_up_to_end)]
m_end = Ax / t_end_x
Amp_array_x[-len(t_end):]=m_end*(t_end-(t_tot - t_end_x)*np.ones(
    len(t_end)))
Amp_array_x[-len(t_end):] = Amp_array_x[-len(t_end):][::-1]

plt.figure()
plt.plot(t, Amp_array_x * 1000)
plt.xlabel('Time [s]')
```

```
plt.ylabel('Amplitude X Position [mm]')
plt.title('Trend of Amplitude X [mm] in function of time [s]')
#-------------------------------------------------
# Y-direction
Ay = Ay * 1e-3  # Conversion from mm to m
Amp_array_y = Ay * np.ones(len(t))

value_to_extract_up_to_start = t_start_y
t_start = t[t ≤ value_to_extract_up_to_start]
m_start = Ay / t_start_y
Amp_array_y[:len(t_start)] = m_start * t_start

value_to_extract_up_to_end = t_end_y
t_end = t[t ≥ (t_tot - value_to_extract_up_to_end)]
m_end = Ay / t_end_y
Amp_array_y[-len(t_end):]=m_end*(t_end-(t_tot-t_end_y)*np.ones(
    len(t_end)))
Amp_array_y[-len(t_end):] = Amp_array_y[-len(t_end):][::-1]

plt.figure()
plt.plot(t, Amp_array_y * 1000)
plt.xlabel('Time [s]')
plt.ylabel('Amplitude Y Position [mm]')
plt.title('Trend of Amplitude Y [mm] in function of time [s]')
#-------------------------------------------------
# Z-direction
Az = Az * 1e-3  # Conversion from mm to m
Amp_array_z = Az * np.ones(len(t))

value_to_extract_up_to_start = t_start_z
t_start = t[t ≤ value_to_extract_up_to_start]
m_start = Az / t_start_z
Amp_array_z[:len(t_start)] = m_start * t_start

value_to_extract_up_to_end = t_end_z
t_end = t[t ≥ (t_tot - value_to_extract_up_to_end)]
m_end = Az / t_end_z
Amp_array_z[-len(t_end):]=m_end*(t_end-(t_tot-t_end_z)*np.ones(
    len(t_end)))
Amp_array_z[-len(t_end):] = Amp_array_z[-len(t_end):][::-1]

plt.figure()
plt.plot(t, Amp_array_z * 1000)
plt.xlabel('Time [s]')
plt.ylabel('Amplitude Z Position [mm]')
plt.title('Trend of Amplitude Z [mm] in function of time [s]')
#-------------------------------------------------
# Sine sweep in X direction
sine_signal_x = chirp(t, f0=f_x, f1=f_x, t1=t_tot, method='linear
    ')
```

```
97 sine_signal_x = sine_signal_x * Amp_array_x
98
99 plt.figure()
100 plt.plot(t, sine_signal_x * 1000, t, np.zeros(len(t)))
101 plt.title('Position along X')
102 plt.xlabel('Time [s]')
103 plt.ylabel('Position [mm]')
104 #-----------------------------------------------
105 # Sine sweep in Y direction
106 sine_signal_y = chirp(t, f0=f_y, f1=f_y, t1=t_tot, method='linear
    ')
107 sine_signal_y = sine_signal_y * Amp_array_y
108
109 plt.figure()
110 plt.plot(t, sine_signal_y * 1000, t, np.zeros(len(t)))
111 plt.title('Position along Y')
112 plt.xlabel('Time [s]')
113 plt.ylabel('Position [mm]')
114 #-----------------------------------------------
115 # Sine sweep in Z direction
116 sine_signal_z = chirp(t, f0=f_z, f1=f_z, t1=t_tot, method='linear
    ')
117 sine_signal_z = sine_signal_z * Amp_array_z
118
119 plt.figure()
120 plt.plot(t, sine_signal_z * 1000, t, np.zeros(len(t)))
121 plt.title('Position along Z')
122 plt.xlabel('Time [s]')
123 plt.ylabel('Position [mm]')
124 #-----------------------------------------------
125 # Assemble signal
126 Signal = np.vstack((sine_signal_x * 1000, sine_signal_y * 1000,
    sine_signal_z * 1000)).T
```

Bibliography

[1] Raouf A Ibrahim. *Liquid sloshing dynamics: theory and applications*. Cambridge University Press, 2005.

[2] R. A. Ibrahim, V. N. Pilipchuk, and T. Ikeda. "Recent Advances in Liquid Sloshing Dynamics". In: *Applied Mechanics Reviews* 54.2 (Mar. 2001), pp. 133–199. ISSN: 0003-6900. DOI: 10.1115/1.3097293. eprint: https://asmedigitalcollection.asme.org/appliedmechanicsreviews/article-pdf/54/2/133/5438074/133_1.pdf. URL: https://doi.org/10.1115/1.3097293.

[3] Thomas M Brocher et al. *The 1964 great Alaska earthquake and tsunamis: A modern perspective and enduring legacies*. Tech. rep. US Geological Survey, 2014.

[4] He Liu and Daniel H Schubert. "Water Storage Tank Response to Earthquake Loads in Alaska—Predictive Modeling by the Finite Element Method". In: *Cold Regions Engineering: Cold Regions Impacts on Transportation and Infrastructure*. 2002, pp. 495–506.

[5] H Norman Abramson. "Dynamics of contained liquids: a personal odyssey". In: *Appl. Mech. Rev.* 56.1 (2003), R1–R7.

[6] H.N. Abramson, United States. National Aeronautics, and Space Administration. *Some Studies of Liquid Rotation and Vortexing in Rocket Propellant Tanks*. NASA technical note. National Aeronautics and Space Administration, 1962. URL: https://books.google.be/books?id=nAtC7ywbgpcC.

[7] H Norman Abramson and Guido E Ransleben Jr. "Simulation of fuel sloshing characteristics in missile tanks by use of small models". In: *Ars Journal* 30.7 (1960), pp. 603–612.

[8] H Norman Abramson, Wen-Hwa Chu, and GUIDO E RANSLEBEN Jr. "Representation of fuel sloshing in cylindrical tanks by an equivalent mechanical model". In: *ARS Journal* 31.12 (1961), pp. 1697–1705.

[9] Alessia Simonini. *PhD Thesis: Sloshing dynamics investigation by means of non-intrusive measurement techniques*. eng. Universite Libre de Bruxelles, 2018.

[10] M Eswaran and Ujjwal K Saha. "Sloshing of liquids in partially filled tanks-a review of experimental investigations". In: *Ocean Systems Engineering* 1.2 (2011), pp. 131–155.

[11] O.M. Faltinsen and A.N. Timokha. *Sloshing*. Cambridge University Press, 2009. ISBN: 9780521881111. URL: https://books.google.be/books?id=81qkPwAACAAJ.

[12] Olav F Rognebakke and Odd M Faltinsen. "Coupling of sloshing and ship motions". In: *Journal of Ship Research* 47.03 (2003), pp. 208–221.

[13] K. Mori. *Proceedings of the International Workshop on Water Waves and Floating Bodies (16th) Held in Hiroshima, Japan on April 22-25, 2001*. AD-a396 725. Hiroshima univ (japan) Department of engineering systems, 2001. URL: https://books.google.be/books?id=7QN20AEACAAJ.

[14] Odd M Faltinsen. "A nonlinear theory of sloshing in rectangular tanks". In: *Journal of Ship Research* 18.04 (1974), pp. 224–241.

[15] Stefano Gallazzi Egidio Di Gialleonardo Antonio Premoli and Stefano Bruni. "Sloshing effects and running safety in railway freight vehicles". In: *Vehicle System Dynamics* 51.10 (2013), pp. 1640–1654. DOI: 10.1080/00423114.2013.814797.

[16] M Toumi, M Bouazara, and MJ Richard. "Impact of liquid sloshing on the behaviour of vehicles carrying liquid cargo". In: *European Journal of Mechanics-A/Solids* 28.5 (2009), pp. 1026–1034.

[17] Helmut F Bauer. *Theory of the fluid oscillations in a circular cylindrical ring tank partially filled with liquid*. National Aeronautics and Space Administration, 1960.

[18] Helmut F. Bauer. "Tables of Zeros of Cross Product Bessel Functions Jp'(ξ)Yp'(kξ) - Jp'(kξ)Yp'(ξ) = 0". In: *Mathematics of Computation* 18.85 (1964), pp. 128–135. ISSN: 00255718, 10886842. URL: http://www.jstor.org/stable/2003415 (visited on 02/21/2024).

[19] Hongyuan Yue, Jianyun Chen, and Qiang Xu. "Sloshing characteristics of annular tuned liquid damper (ATLD) for applications in composite bushings". In: *Structural Control and Health Monitoring* 25.8 (2018), e2184.

[20] Jean Muller, Philippe Planquart, and Delphine Laboureur. "Experimental investigation of the transition between linear to chaotic regimes of sloshing". In: *Multiphase Science and Technology* 35.4 (2023).

[21] Emil Hopfinger and Volker Baumbach. "Liquid sloshing in cylindrical fuel tanks". In: *EUCASS Proceedings Series* 1 (Sept. 2009), pp. 279–292. DOI: 10.1051/eucass/200901279.

[22] George W Housner. "Dynamic pressures on accelerated fluid containers". In: *Bulletin of the seismological society of America* 47.1 (1957), pp. 15–35.

[23] George William Housner and Donald E Hudson. "Earthquake research problems of nuclear power plants". In: *Nuclear Engineering and Design* 3.2 (1966), pp. 308–319.

[24] JF Kunze. "Additional Analysis of the SL-1 Excursion, Final Report of Progress, July through October 1962". In: *IDO-19313, US Department of Energy, Idaho Operations Office, Idaho Falls, Idaho* (1962).

[25] TH Thomas et al. *Nuclear reactors and earthquakes*. Tech. rep. Lockheed Aircraft Corp., Palo Alto, CA (United States); Holmes and Narver ..., 1961.

[26] M. Jeltsov, W. Villanueva, and P. Kudinov. "Seismic sloshing effects in lead-cooled fast reactors". In: *Nuclear Engineering and Design* 332 (2018), pp. 99–110. ISSN: 0029-5493. DOI: https://doi.org/10.1016/j.nucengdes.2018.03.020. URL: https://www.sciencedirect.com/science/article/pii/S0029549318302917.

[27] Marti Jeltsov, Walter Villanueva, and Pavel Kudinov. "Parametric study of sloshing effects in the primary system of an isolated lead-cooled fast reactor". In: *Nuclear Technology* 190.1 (2015), pp. 1–10.

[28] Konstantinos Myrillas et al. "CFD and experimental investigation of sloshing parameters for the safety assessment of HLM reactors". In: *Nuclear Engineering and Design* 312 (2017). 16th International Topical Meeting on Nuclear Reactor Thermal Hydraulics, pp. 317–326. ISSN: 0029-5493. DOI: https://doi.org/10.1016/j.nucengdes.2016.06.042. URL: https://www.sciencedirect.com/science/article/pii/S0029549316302035.

[29] International Atomic Energy Agency. *Generation IV*. URL: https://aris.iaea.org/PDF/ALFRED.pdf.

[30] Ansaldo Energia. *Generation IV*. URL: https://www.ansaldoenergia.com/offering/nuclear/generation-iii.

[31] Kaunas university of technology. *Proof of augmented safety conditions in advanced liquid metal cooled systems (PASCAL)*. URL: https://en.ktu.edu/projects/proof-of-augmented-safety-conditions-in-advanced-liquid-metal-cooled-systems-pascal/.

[32] ASME Performance Test Code. *Test Uncertainty PTC 19.1 - 2018*. American Society of Mechanical Engineers, 2018.

[33] Kostantinos Myrillas, Jean-Marie Buchlin, and Philippe Planquart. "Internal report: Democritos - sloshing phase 4". In: (2014-2015).

[34] Jean Muller. "Internal report: ALFRED Mockup - Similarity study". In: (2023).

[35] PCB Piezotronics. *PCB Piezotronics*. URL: https://www.pcb.com/products?m=356b18.

[36] NATIONAL INSTRUMENTS CORP. *NI-9234 Specifications*. Data Sheet Updated 2023-06-30. NATIONAL INSTRUMENTS CORP., 2023. URL: https://www.ni.com/docs/en-US/bundle/ni-9234-specs/page/specs.html.

[37] Xuebo Zheng, Bo Yang, and Bofeng Bai. "Capacitance probe for water holdup measurement in crude oil-water flows". In: *Measurement: Sensors* 10-12 (2020), p. 100028. ISSN: 2665-9174. DOI: https://doi.org/10.1016/j.measen.2020.100028.

[38] Protezione civile - Seismic activities and emergency planning. *Artelia - Grenoble*. URL: https://rischi.protezionecivile.it/en/seismic/activities/emergency-planning-and-damage-scenarios/seismic-classification/.

[39] Dlubal. *Dlubal:Structural Analysis and Design Software*. URL: https://www.dlubal.com/en/load-zones-for-snow-wind-earthquake/.